

Interfacial Effects in Solid-Liquid Glyme-Based Electrolytes for Lithium Batteries

Von der Fakultät Chemie der Universität Stuttgart
zur Erlangung der Würde eines

Doktors der Naturwissenschaften
(Dr. rer. nat.) genehmigte Abhandlung

Vorgelegt von

Seyedeh Maryam Nojabae

aus Tonekabon

Hauptberichter: Prof. Dr. Joachim Maier

Mitberichterin: Prof. Dr. Sabine Ludwigs

Prüfungsvorsitzender: Prof. Dr. Peer Fischer

Tag der mündlichen Prüfung: 13.12.2018

Max-Planck-Institut für Festkörperforschung

2018

What you seek is seeking you.

Rumi

Erklärung über die Eigenständigkeit der Dissertation

Ich versichere, dass ich die vorliegende Arbeit mit dem Titel *Interfacial Effects in Solid-Liquid Glyme-based Electrolytes for Lithium Batteries* selbständig verfasst und keine anderen als die angegebenen Quellen und Hilfsmittel benutzt habe; aus fremden Quellen entnommene Passagen und Gedanken sind als solche kenntlich gemacht.

Declaration of Authorship

I hereby certify that the dissertation entitled *Interfacial Effects in Solid-Liquid Glyme-based Electrolytes for* is entirely my own work except where otherwise indicated. Passages and ideas from other sources have been clearly indicated.

Name/Name: _____

Unterschrift/Signed: _____

Datum/Date: _____

Contents

Contents	VII
List of Abbreviations and Symbols	ix
Zusammenfassung	xv
Abstract	xvii
Chapter 1 Introduction and Motivation	1
Chapter 2 Theoretical Background	5
2.1 Electrical Double Layer	5
2.1.1 Gouy-Chapman-Stern Model	5
2.1.2 Debye-Hückel (<i>DH</i>) Approximation	7
2.2 Mechanism of Ion Conduction in Solid-Liquid Lithium Electrolyte	9
2.3 Solid Electrolyte Interphase (SEI) on Lithium Electrode	14
2.3.1 SEI Formation in Lithium Metal Batteries (LMB)	14
2.3.2 Charge Transfer in SEI	16
2.3.3 SEI and Dendrite Formation	17
2.3.4 SEI Modification	18
Chapter 3 Glyme-based Electrolyte in Contact with Mica	21
3.1 Experimental	21
3.1.1 Materials	21
3.1.2 Surface Force Apparatus (SFA)	24
3.1.3 Zeta Potential (ζ)	27
3.1.4 Infrared Spectroscopy (IR)	28
3.1.5 Impedance Spectroscopy (IS)	28
3.1.6 Rheology	28
3.2 Results and Discussion	29
3.2.1 IR	29
3.2.2 Viscosity, Zeta Potential and Conductivity	33
3.2.3 SFA	35
3.3 Conclusions	42
Chapter 4 Solid-Liquid Glyme-Based Composite Electrolyte	43
4.1 Experimental	43
4.1.1 Materials	43
4.1.2 Characterisation Techniques	43
4.1.3 Impedance Spectroscopy	44

4.1.4	Galvanostatic Polarization	47
4.1.5	Stripping-Plating Experiments.....	50
4.2	Results and Discussion.....	51
4.2.1	Characterization of the AAO	51
4.2.2	Electrochemical Properties of AAO: (1 M LiTf/triglyme).....	52
4.2.3	Influence of Salt Concentration on Electrochemical Properties of AAO: (LiTf/triglyme).....	56
4.2.4	Influence of Temperature on Electrochemical Properties of AAO: (1 M LiTf/triglyme)	61
4.2.5	Lithium Stripping-Plating Experiments.....	65
4.3	Conclusions	68
Chapter 5	SEI on Lithium Electrode in Contact with Glyme Electrolyte.....	69
5.1	Experimental	69
5.1.1	Materials	69
5.1.2	X-ray Photoelectron Spectroscopy (XPS)	70
5.1.3	Electrochemical Measurement.....	72
5.1.4	Surface Modification:	72
5.2	Results and Discussion.....	73
5.2.1	Chemical Composition and Morphology of the SEI on lithium	73
5.2.2	Temperature and Salt Concentration Influence on the SEI	80
5.2.3	Electrochemical Cycling Influence on the SEI.....	84
5.2.4	SEI Modification for Lithium Metal Battery	87
5.3	Conclusions	93
Chapter 6	General Conclusions.....	94
Appendix	97
List of Figures	107
References	113
Acknowledgments	123
Curriculum Vitae	125

List of Abbreviations and Symbols

Abbreviations

AAO	anodic alumina
AC	alternating current
DC	direct current
<i>DH</i>	Debye-Hückel
DSC	differential scanning calorimetry
EDL	electric double layer
EIS	electrochemical impedance spectroscopy
FD	force distance
FECO	fringe of equal chromatic order
FIB	focused ion beam
<i>GP</i>	Gouy-Chapman
IHP	inner Helmholtz plane
LiTDI	lithium 4,5-dicyano-2-(trifluoromethyl)imidazole
LiTf	lithium trifluoromethanesulfonate
LMB	lithium metal battery
NMR	nuclear magnetic resonance
OHP	outer Helmholtz plane
<i>PB</i>	Passion-Boltzmann
SEI	solid electrolyte interphase

SFA surface force apparatus
 SLI solid liquid interface
 TEGDME tri (ethylene glycol) dimethyl ether
 XPS X-ray photoelectron spectroscopy

Symbols

a_s area on the oxide particle occupied with adsorbed ion
 c_{salt} concentration of the salt
 $c_j(x)$ local concentration of the ions of type j at distance x
 c_i concentration of ionic species i
 $c_{j,\infty}$ bulk concentration of ions
 c_{free} concentration of free ions
 c_{pair} concentration of ion pairs
 c_{dimer} concentration of dimers
 c_s concentration of adsorbed anion on oxide particle surface
 c_{Bulk} bulk capacitance
 C capacitances
 d thickness of stern layer
 D distance between Mica sheets
 D^* salt diffusion coefficient
 e charge of the electron
 E interaction energy
 F Faraday constant
 f Henry's function

F	force between two surfaces
h	Planck constant
I_M	ionic strength
$I^*(\omega)$	alternating current
I_∞	the steady state current
K_{diss}	ion pair dissociation constant
k_B	Boltzmann constant
l_B	Bjerrum length
L	thickness of the polymer layer
N_A	Avogadro number
P	pressure gradient
Q	CPE-T of fitted equivalent circuit
r	radius of particles
R	resistance
$R_{tot,0}$	initial total resistance
$R_{SEI,0}$	initial interfacial resistance
$R_{SEI,\infty}$	final interfacial resistance
R_+	corresponding resistance to cation
R_-	corresponding resistance to anion
S	mean distance between two complexation center
s	transport parameter of ion pairs
t_{m^+}	transference number of the cations

u_+ cationic mobility
 U_∞ steady state voltage
 $U^*(\omega)$ alternating voltage
 V applied voltage
 Z^* complex impedance
 z_- anion charges
 z_+ cation charges
 z_j valence of ion j
 $\Psi(x)$ electric potential at distance x
 $\rho(x)$ space charge density at distance x
 α CPE-P of fitted equivalent circuit
 β_∞ proportion of bulk contributing to σ_m
 β_L proportion of bulk contributing to σ_m
 γ activity coefficients
 ϵ_0 permittivity of the vacuum
 ϵ dielectric constant of the medium
 ζ Zeta potential
 η viscosity
 θ phase shift
 κ Debye-Hückel parameter
 λ Debye length
 μ_d dynamic electrophoretic mobility

ν frequency
 $\rho(x)$ space charge density at distance x
 ρ_p particle density
 ρ_m liquid density
 σ ionic conductivity
 σ_+^{ex} conductivity in the space charge zone
 σ_∞ conductivity of the bulk
 σ_m effective conductivity of the composite electrolyte
 σ_+ ionic conductivity of cation
 σ_- ionic conductivity of anions
 σ_- ionic conductivity of anions
 σ^δ ambipolar conductivity
 τ time constant
 φ solution volume fraction
 φ_L space charge volume fraction
 ϕ work function depending on the setup
 $\Psi(x)$ potential at distance x
 ϑ measure of the strength of the adsorption effect
 ω angular frequency

Zusammenfassung

Fest-Flüssig-Grenzflächen sind für das Verständnis des Ladungstransportmechanismus in elektrochemischen Zellen von großer Bedeutung. Die hier vorgestellte Studie umfasst Fest-Flüssig-Grenzflächen in Lithiumzellen, die Fest-Flüssig-Elektrolyte auf der Basis von Ethylenglykolethern (Glyme) enthalten. Die Bildung und die Chemie solcher Grenzflächen und die damit verbundenen Auswirkungen auf das elektrochemische Verhalten des Systems werden eingehend untersucht.

In "Soggy Sand"-Elektrolyten bildet sich an der Oberfläche der Oxidteilchen eine Raumladungszone durch bevorzugte Adsorption von Anionen der in aprotischen Lösungsmitteln gelösten Salze. Folglich wird nahe der Oxidoberfläche die Beweglichkeit der Anionen verringert und die Konzentration der Kationen erhöht, wodurch lokal die Kationenleitfähigkeit und die Überföhrungszahl verbessert wird. Es werden komplementäre Techniken wie Messung der Oberflächenkraft (surface force apparatus SFA), Infrarotspektroskopie, Zetapotential-Messungen und elektrochemische Impedanzspektroskopie eingesetzt, um das Schichtungs- und Abschirmverhalten in dem analogen System zu verstehen, das Lithium-Triflat in Triglyme und gespaltene Muskovit-Glimmeroberflächen umfasst. Man findet eine ausgeprägte elektrochemische Doppelschichtstruktur an der Grenzfläche, die zwei verschiedene Bereiche unterhalb von ~ 15 nm umfasst. Die durch die SFA-Messungen geschätzte Abschirmlänge in Elektrolyten auf Glyme-Basis ist viel höher als nach der Debye-Hückel-Theorie erwartet. Dies lässt sich mit starken elektrostatischen Wechselwirkungen zwischen den Ionen erklären. Dieses Modell kann nicht nur auf "Soggy Sand"-Elektrolyte, sondern auch auf die Grenzfläche zwischen Elektrode und Elektrolyt erweitert werden, da die Abschirmlänge von den Volumeneigenschaften bestimmt wird.

In einem praxisnäheren Ansatz werden Fest-Flüssig-Kompositelektrolyte verwendet, die aus nanoporösem anodischem Aluminiumoxid bestehen, in das in Triglyme gelöstes

Lithium-Triflat infiltriert ist. Impedanzspektroskopie und galvanostatische Polarisationsmessungen zeigen, dass der Kompositelektrolyt eine erhöhte Lithiumüberführungszahl und eine flüssigkeitsähnliche Leitfähigkeit bietet, was auf eine beachtliche, aber nicht vollständig ausgeschöpfte Adsorptionskapazität hinweist. Darüber hinaus wird die Erhöhung der Lithiumüberführungszahlen bei erhöhten Temperaturen und niedrigen Salzkonzentrationen im Hinblick auf Mobilität und Salzdissoziationsgrad diskutiert. Hinsichtlich der möglichen Praxisanwendungen wird die Fähigkeit dieser Elektrolyte zur Unterdrückung der dendritischen Lithiumabscheidung und zur Vermeidung von Überspannungen über Hunderte von Zyklen hinweg gezeigt. Dies geschah mittels vielfach wiederholter Abscheidung und Auflösung von metallischem Lithium.

Die Passivierungsschicht (solid-electrolyte-interphase, SEI) die sich am dem flüssigen Elektrolyten ausgesetzten Lithiummetall bildet, ist für die Grenzfläche zwischen Elektrode und Elektrolyt von entscheidender Bedeutung. Die Zusammensetzung und Morphologie der SEI wird mit einer Kombination von Röntgen-Photoelektronenspektroskopie (XPS) und Rasterelektronenmikroskopie mit fokussiertem Ionenstrahl (FIB) bestimmt. Dabei wird eine dicke SEI gefunden (mehrere hundert nm), die aus anorganischem (LiOH , Li_2CO_3 , LiF , Li_2O , Li_2S und Li_2S_x) und organischen Spezies (wie RCH_2OLi) besteht. Die Abhängigkeit der Zusammensetzung und Morphologie der SEI von der Salzkonzentration, dem Anion und der Temperatur wurde untersucht. Die SEI scheint bei höherer Salzkonzentration und erhöhter Temperatur dicker und leitfähiger zu werden. Die Zusammensetzung der SEI ändert sich bei niedriger Salzkonzentration drastisch (nur geringe Menge anorganischer Phasen), während Temperaturschwankungen keine Zusammensetzungsänderung bewirken. Schließlich wird gezeigt, dass stickstoffhaltige Salze eine SEI bilden können die Li_3N enthält. Diese bieten eine verbesserte Zyklierfähigkeit im Vergleich zu schwefelreichen Lithiumsalzen, welche die Bildung von instabilem Li_xS_y induzieren.

Abstract

Solid-liquid interfaces are of great importance for understanding charge transport mechanisms in electrochemical cells. The presented study here is dedicated to solid-liquid interfaces involved in lithium cells containing solid-liquid glyme-based electrolytes. The formation and chemistry of such interfaces and the associated impact on the electrochemical behaviour of the system have been studied in detail.

In “soggy sand” electrolytes, space charge zones form due to preferential adsorption of salt anions on the surface of the oxide particles in the salt containing aprotic solvent. Consequently, in the vicinity of the oxide particle surface, anion mobility is depressed, and the concentration of cations is increased, causing local enhancement in the cation conductivity and transference number. Herein, complementary techniques such as surface force apparatus, infrared spectroscopy, Zeta potential measurements and electrochemical impedance spectroscopy are employed to understand the layering and screening behaviour in the analogous system comprising lithium triflate/triglyme and cleaved muscovite mica surface. A pronounced interfacial electrochemical double layer structure is found, embracing two distinct regions below $D \sim 15$ nm. The screening lengths in glyme-based electrolytes estimated from the SFA measurements are of much higher value than expected according to the Debye-Hückel theory. This can be explained in terms of strong ion-ion electrostatic interactions. This model can be expanded not only to soggy sand electrolytes but also to the electrode/electrolyte interface, as the screening length is indeed determined by bulk properties.

In a more practical approach, solid-liquid composite electrolytes consisting of nanoporous anodic aluminium oxide infiltrated by lithium triflate salt containing triglyme are used. Impedance spectroscopy and galvanostatic polarization measurements have shown that the composite electrolyte offers an enhanced lithium transference number and liquid-like conductivity, indicating distinctive but not entirely exhaustive adsorption level. Additionally, the enhancement in lithium transference numbers at elevated temperatures and low salt concentrations is discussed in terms of mobility and degree of salt dissociation. Regarding the applications, the ability of these electrolytes in suppressing the dendritic lithium deposition and avoiding over-potential for hundreds

of cycles is shown using lithium stripping-plating experiment.

The passivation layer (solid electrolyte interphase, SEI) formed on the lithium metal exposed to the liquid electrolyte is of crucial matter to the electrode/electrolyte interfacial layering. The composition and morphology of the SEI are determined using a combination of X-ray photoelectron spectroscopy and Focused-Ion-Beam (FIB) scanning electron microscopy. A thick SEI (hundreds of nm), composed of inorganic LiOH, Li₂CO₃, LiF, Li₂O, Li₂S, and Li₂S_x and organic species such as RCH₂OLi is observed. The compositional and morphological dependence of the SEI on salt concentration, salt anion and temperature are probed. The SEI appears to be thicker and more conductive at higher salt concentrations and elevated temperatures. The composition of the SEI changes drastically at lower salt concentrations with a small amount of inorganic phases visible, while the temperature variations induce no compositional changes. Finally, it is shown that the salts containing nitrogen are able to form Li₃N-containing SEI, offering improved cell cyclability in comparison to sulphur-rich lithium salts which are inducing the formation of unstable Li_xS_y.

Chapter 1 Introduction and Motivation

Meeting the increased energy demand is an intricate challenge encountered by the modern society. Among the rechargeable batteries, Lithium ion batteries have been studied vastly and commercialized due to their cyclability and life time [1-4]. Alternatively, lithium metal batteries (LMB) have regained great attention recently due to their higher energy and power densities to address this ongoing energy appeal [5-7]. The lithium metal anode offering high theoretical capacity ($3,860 \text{ mAh g}^{-1}$), the lowest electrode potential (-3.04 V vs. standard hydrogen electrode) and low gravimetric density (0.534 g cm^{-3}) is considered the optimum anode for the high performance batteries. In particular, lithium-sulfur (Li-S) batteries and lithium-air batteries (Li-O) employing lithium metal as negative electrode have been of great interests [8, 9].

In addition to the electrode, electrolyte is yet another component crucial for ionic transport and stability of the cell. Conventional lithium ion battery electrolytes consist of an aprotic organic solvent and a lithium salt. Liquid lithium battery electrolytes have drawbacks such as flammability and incompatibility with lithium metal anode. In addition, conventional liquid electrolytes exhibit relatively low lithium transference number, giving rise to salt concentration gradients and consequently capacity and cell life time decay [10]. Nowadays, electrolytes with enhanced lithium transference number are of great practical importance explicitly in LMB for high power applications needed in E-Mobility.

To overcome these complications solid-liquid composite electrolytes have been developed, combining the favourable electrochemical properties of the liquid state associated with the beneficial mechanical properties of the solid state [11-13]. In “soggy sand” electrolyte as the first example of solid-liquid electrolytes, addition of oxide nanoparticles to lithium salt containing liquid electrolyte leads to the formation of space charge zone (or an electrochemical double layer) consisting of adsorbed anions on the particle surface compensated by cations in the diffuse part [11, 14]. Such interfacial effect leads to ion pair dissociation and improvement of the cation

conductivity and transference number.

Another component in the lithium batteries, playing a determining role in stability of the cell, is the passivation layer formed on the lithium exposed to the electrolyte. In conventional lithium batteries consisting of salt containing aprotic organic solvent, the formation of interphase between electrode and electrolyte, the so called “solid electrolyte interphase” (SEI) is unavoidable [15]. This passivation layer formed on the reactive lithium metal is yet another complication in LMB, causing additional impedance or dendrite formation detrimental for cell safety and cycle life [16].

In all electrochemical devices including lithium batteries, interfaces are of great importance to charge transfer mechanism. Particularly, in lithium batteries employing liquid or solid-liquid composite electrolytes, understanding the space charge zone (electric double layer) formed at the electrode/electrolyte is crucial to improve the electrochemical performance. The emerged solid electrolyte interphase indeed promotes new aspects to the formed space charge zone at this interface. Furthermore, in solid-liquid composite electrolytes such as “soggy sands”, such interfaces are present in the electrolyte itself. If nano-porous monolithic oxides are employed, where the liquid is nano-confined, the structure and thickness of the formed space charge becomes even more influential.

In the present work, the solid-liquid interfaces within the composite glyme-based electrolytes as well as in contact with lithium metal are investigated spectroscopically and their roles in transport processes are studied electrochemically.

Firstly, the ion redistribution and the formation of space charge zone with specific screening behaviour of triflate salt-containing triglyme at mica interfaces is investigated. This interface can serve as a model for the electric double layer within solid-liquid electrolyte and electrode/electrolyte contact. The thickness and structure of the interfacial layer is studied employing surface force apparatus (SFA), infrared (IR) spectroscopy and Zeta potential measurements.

Additionally, solid-liquid composites consisting of nanoporous anodic alumina

infiltrated with glyme electrolyte are investigated. The electrochemical properties including lithium transference number, conductivity and cyclability of this electrolyte are explored. In this context, the influence of salt concentration and temperature on the interfacial effect and the electrochemical behaviour are probed exclusively.

In the last chapter, composition, morphology and resistance of the SEI formed at the lithium metal electrode in contact with glyme-based composite electrolyte and their evolution upon cycling, changing temperature and salt concentration is studied using impedance spectroscopy, X-ray photoelectron spectroscopy and focused-ion-beam scanning electron microscopy. As far as the application is concerned, the deposition of dendritic and mossy lithium in such electrolytes and the possibility of controlling the formation of the solid electrolyte interphase (SEI) through artificial SEI is discussed.

Chapter 2 Theoretical Background

2.1 Electrical Double Layer

2.1.1 Gouy-Chapman-Stern Model

Exposing a surface to an electrolyte leads to a rearrangement of ions in the vicinity of the surface and formation of an electric double layer (EDL) in which the distribution of ions is different from the bulk. The concept of EDL was initially described by von Helmholtz in a colloidal system, where the surface charge neutralization by a layer of counter ions identical to the conventional capacitance model was suggested [17]. Later, the Gouy-Chapman model was developed, proposing that the surface charge is balanced by a continuous steeply decaying distribution of counter-ions forming the diffuse double layer [18, 19].

A further extension that combines Helmholtz and Gouy-Chapman model was developed by Stern, now widely used to describe EDL [20]. The Gouy-Chapman-Stern, shown in Figure 2-1, consists of a rigid (Stern) layer, followed by a purely diffuse (Gouy-Chapman) layer. The Stern layer is the compact region next to the surface consisting of non-mobile adsorbed ions. The first layer of these specifically adsorbed ions allocated directly at the interface is known as inner Helmholtz plane (IHP). (Note that the specifically adsorbed ions do not need to be of the opposite charge). The outer Helmholtz plane (OHP) is the layer next to the IHP containing the non-specifically adsorbed counter ions and forms the borderline between the Stern and diffuse layer. In IHP and OHP, the potential drop is linear. The potential distribution in the diffuse part is taken as continuous and is the result of the competition between Columbic attraction (surface charge and the counter-ions) and the osmotic pressure forces, or in other words between interaction energy and configurational entropy [21].

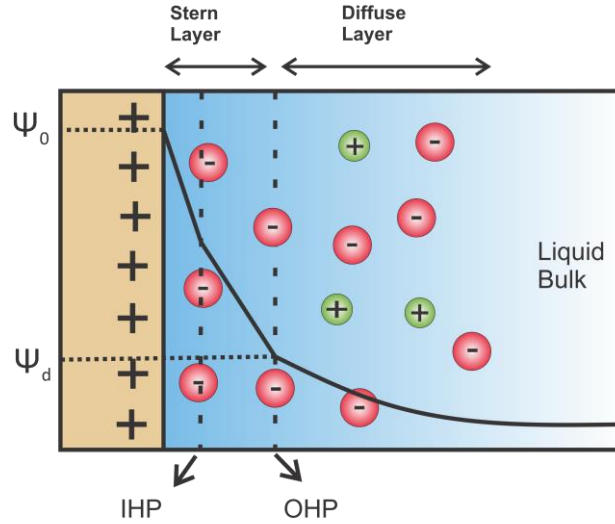


Figure 2-1 Gouy-Chapman-Stern model for EDL at solid-liquid interface. This model consists of 2 layers: Stern and diffuse layer.

The charge distribution in the diffuse layer can be mathematically modelled using the Poisson-Boltzmann (*PB*) equation. For 1D geometry, the Poisson equation relates the the electric potential ($\Psi(x)$) to charge density ($\rho(x)$):

$$\nabla^2 \Psi(x) = \frac{\nabla^2 \Psi(x)}{d x^2} = -\frac{\rho(x)}{\varepsilon_0 \varepsilon} \quad \text{Equation 2-1}$$

where ε is the dielectric constant of the medium considered equal to the bulk, ε_0 is the permittivity of the vacuum, x is the distance from the OHP and ρ is the charge density in the system. Charge density is related to the local concentration of ions:

$$\rho(x) = e \sum_j z_j c_j(x) \quad \text{Equation 2-2}$$

where $c_j(x)$ is the local concentration of the ions of type j and it is related to its bulk value $c_{j,\infty}$ using Boltzmann distribution:

$$c_j(x) = c_{j,\infty} \exp\left(\frac{-z_j e \Psi}{k_B T}\right) \quad \text{Equation 2-3}$$

Here, e is the electron charge, T is the absolute temperature and k_B is Boltzmann constant. Combination of Equation 2-1 and 2-2 leads to the Poisson-Boltzmann (*PB*) equation, which is a non-linear partial differential equation:

$$\frac{\nabla^2 \Psi(x)}{d x^2} = -\frac{e}{\varepsilon_0 \varepsilon} \sum_j z_j c_{j,\infty} \exp\left(\frac{-z_j e \Psi}{k_B T}\right) \quad \text{Equation 2-4}$$

2.1.2 Debye-Hückel (DH) Approximation

Debye-Hückel approximation simplifies the *PB* equation with the assumption that the potential is small enough, resulting in [22]:

$$\exp\left(\frac{-z_j e \Psi}{k_B T}\right) \approx 1 - \frac{z_j e \Psi}{k_B T} \quad \text{Equation 2-5}$$

With this approximation and considering the electro-neutrality in a completely dissociated ($c_- = c_+ = c$) and symmetrical electrolyte ($z_- = z_+ = z$), Equation 2-4 becomes:

$$\frac{\nabla^2 \Psi(x)}{d x^2} = \kappa^2 \Psi \quad \text{Equation 2-6}$$

which is the linearized form of *PB* equation. The solution to this differential equation is a simple exponential decay taking into account the following boundary conditions, with d being thickness of the Stern layer:

$$\Psi = \Psi_d \exp(-\kappa(x - d)) \quad \Psi(d) = \Psi_d, \Psi(\infty) = 0 \quad \text{Equation 2-7}$$

Here, κ is the *DH* parameter, which is reciprocal of the Debye length (λ):

$$\kappa^{-1} = \lambda = \sqrt{\frac{\varepsilon_0 \varepsilon k_B T}{2N_A e^2 c}} \quad \text{Equation 2-8}$$

Major assumptions in the *GC* model are:

- Ions are point charges
- The non-Columbic interactions in the vicinity of ions are ignored.
- The solvent is a continuum with constant permittivity(ε), for which the bulk value is taken
- Electric potentials in Equation 2.1 and 2.3 are approximately identical.

The *GC* model typically leads to reasonable approximation for small salt concentration, but fails particularly in predicting the screening length at high salt concentrations.

Another important length parameter is the Bjerrum length (l_B), the length between two ions at which the electrostatic potential energy equals the thermal energy of ions. Pairs of distances lower than or equal to l_B , are considered as associated:

$$l_B = \frac{e^2}{4\pi\epsilon_r\epsilon_0 k_B T}$$

Equation 2-9

2.2 Mechanism of Ion Conduction in Solid-Liquid Lithium Electrolyte

The concept of heterogeneous doping has been initially proposed to explore the conductivity enhancement mechanism in solid-solid composites [23]. Increase in ionic conductivity by one order of magnitude or more is achieved by addition of oxide particles such as Al_2O_3 , SiO_2 to solid anionic conductors (CaF_2 , SrF_2 , PbF_2) or the cationic conductors (LiI , LiCl , AgCl , AgBr) [24-27]. The introduction of the particles leads to the formation of a space charge region on the particle surface (similar to EDL) as a result of ion adsorption leading to the rearrangement of the ionic and electronic defects. The difference in the local free energy of the defects in the bulk and at the interface (oxide/matrix) promotes adsorption of one kind of the ions at the surface of the oxide and thus enhancement of concentration of the counter charge carrier. Preferential allocation of the small oxide particles in the grain boundaries of the ionic conductor provides efficient percolation pathways that are essential for the overall conductivity increase [23].

Subsequently, this concept has been employed to design solid-liquid electrolytes, offering the high ionic conductivity of a liquid accompanied with favourable mechanical properties of solids [11, 14, 28]. “Soggy sand electrolytes” are the class of synergistic solid-liquid electrolytes, developed by addition of fillers to salt containing aprotic solvents. Introduction of surface active ceramic particles to the electrolyte leads to formation of space charge region, depicted in Figure 2-2, due to the preferential adsorption of one sort of ions on the surface which causes salt ion pair dissociation, increase in concentration of this type of ions and depletion of the concentration of the counter-ions. Different oxides including SiO_2 , TiO_2 and Al_2O_3 have been investigated as heterogeneous dopant in liquid electrolytes, with the degree of the “soggy sand” effect changing by using various solvents and fillers [11]. For instance, SiO_2 with high density of $-\text{OH}$ groups on the surface shows higher overall ionic conductivity enhancement in comparison to the other dopants, due to the stronger ability of anion adsorption as a

consequence of its higher surface acidity [14, 29].

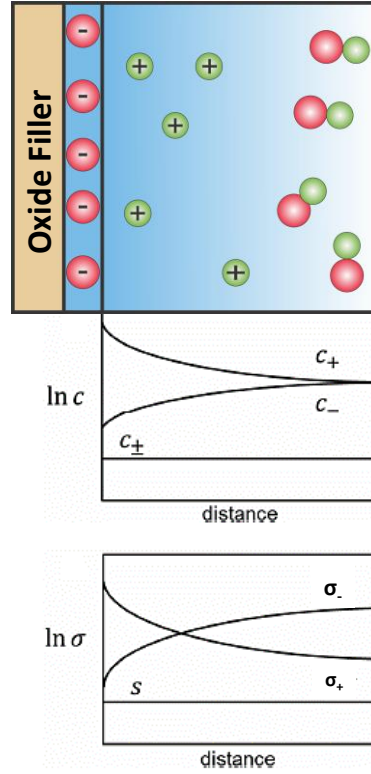


Figure 2-2 Formation of the space charge and profile of concentration and conductivity as function of distance from the surface of oxide particle [11].

Owing to this interfacial effect the conductivity of one sort of ion in the vicinity of the particles is increased while that of the counter-ion decreased. The conductivity in the space charge zone can be calculated via [23, 30]:

$$\langle \sigma_+^{ex} \rangle = Fu_+ \left(2c_\infty \frac{\vartheta}{1-\vartheta} \right) = 2\sigma_\infty \frac{\vartheta}{1-\vartheta} \quad \text{Equation 2-10}$$

where F is the faraday constant, c_∞ is the bulk concentration, u_+ represents the cationic mobility at the interface which can be calculated using the molar conductivity, and ϑ is the measure of the strength of the adsorption effect. For large effect ($\vartheta \rightarrow 1$), Equation 2-10 results in:

$$\langle \sigma_+^{ex} \rangle = Fu_+ \sqrt{c_s c_\infty} \quad \text{Equation 2-11}$$

where c_s is concentration of counter ions at OHP. However, the local phenomena does

not suffice to observe an overall increased conductivity. Indeed, the particles should be able to form a continuous network that provides the pathways for the free ions to percolate along. The effective conductivity of the composite electrolyte (σ_m) can be calculated considering the parallel-switching of the bulk and space charge zones [11, 23]:

$$\sigma_m = \beta_\infty(1 - \varphi)\sigma_\infty + \beta_L\varphi_L\langle\sigma_+^{ex}\rangle \quad \text{Equation 2-12}$$

where φ and φ_L correspond to the filler and the space charge volume fraction respectively, β_∞ and β_L correspond to the proportion of bulk and space charge zone contributing to σ_m and hence take account of the particle distribution. The β_L values can be considered to be constant for a given morphology. For an ideal parallel-switching, β_∞ and β_L are approximately equal to unity. Figure 2-3 schematically represents the variation of the effective conductivity of the composite (normalized by σ_∞) as a function of volume fraction of particles. Starting from the conductivity of pure electrolyte ($\sigma_m = \sigma_\infty$), the addition of the filler results in an increase in σ_m due to the ion pair dissociation and formation of the space charge pathways.

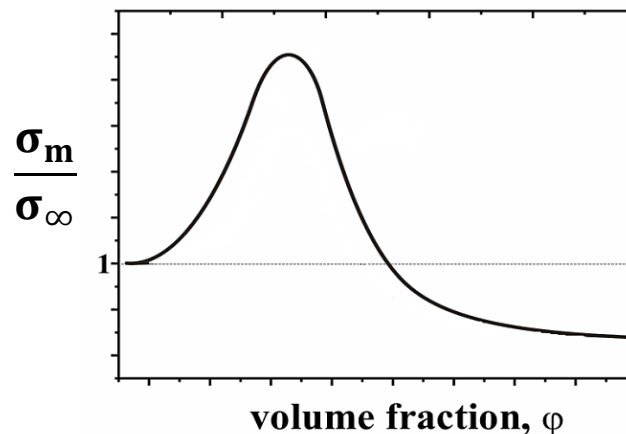


Figure 2-3 Normalized ionic conductivity of the “soggy sand” electrolyte as a function of the volume fraction of added particle [14].

However, upon further addition of the dopant, σ_m decays as a consequence of blocking of the space charge pathways which can even suppress σ_m to lower values than for the pure liquid ($\beta_\infty \ll 1$). A concomitant very favourable effect is the increased

transference number of cations as the consequence of anion immobilization. Both effects are interrelated. Furthermore, the σ_{m+} can be derived using Equation 2-12 and employed to calculate the transference number of the cations (t_{m+}) in “soggy sand” electrolyte [11, 31, 32]:

$$t_{m+} = \frac{\sigma_{m+}}{\sigma_{\infty}} = \frac{\beta_{\infty}(1-\varphi)(t_{\infty+}-1) + \frac{\Delta\sigma_{m+}}{\sigma_{\infty}} + 1}{\frac{\Delta\sigma_{m+}}{\sigma_{\infty}} + 1} \quad \text{Equation 2-13}$$

where $t_{\infty+}$ is the transference number of liquid electrolyte and $\Delta\sigma_m = \sigma_m - \sigma_{\infty}$. Note that here it is assumed that the adsorbed amount is still small compared to the overall value, so that the values of σ_{∞} and σ_{-} in the bulk are the same before and after adsorption.

As depicted in Figure 2-4, similar to σ_{m+} , the t_{m+} will increase upon addition of dopant towards a maximum as the space charge region forms and the mobility of anion is suppressed. Upon increasing φ , blocking of space charge pathways occurs which decreases t_{m+} . However, with the further increase of φ leading to disappearance of bulk contribution, β_{∞} drops significantly, which has a positive effect on t_{m+} .

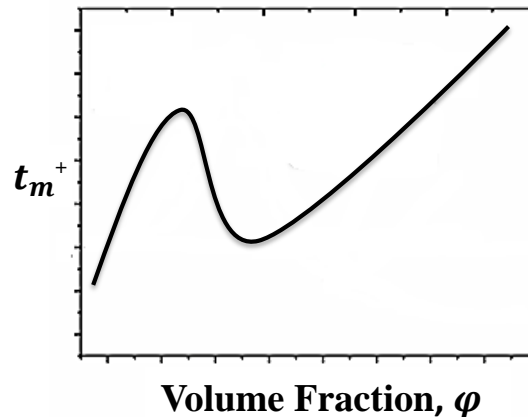


Figure 2-4 Lithium transference number dependence on the volume fraction of the added particles.

At extreme volume fraction of the filler a high cation transference number is achievable notwithstanding a lower conductivity as bulk pathways vanish and space charge layers overlap [32].

The liquid and gel form of this electrolyte encounter sedimentation and agglomeration, causing lack of reproducibility [33]. In the case when mesoporous silica is used as a filler, ionic transport is possible inside the pores and transference numbers around 80% were shown to be possible at volume fractions around 0.1 [12]. Indeed in the case that the salt containing electrolyte flow in nano-channels of oxide material, shown in Figure 2-5, where the diameter of pores are corresponding to the thickness of space charge zone (or a length of EDL), the local effect could be translated to the entire system with highly percolating space charge zones.

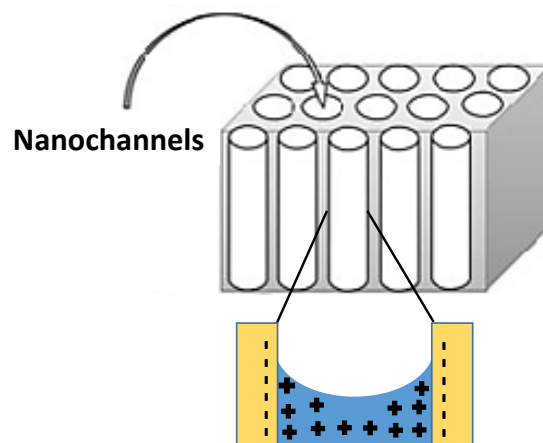


Figure 2-5 Electrolyte confined in the surface active nano-channels removing the bulk effect.

2.3 Solid Electrolyte Interphase (SEI) on Lithium Electrode

2.3.1 SEI Formation in Lithium Metal Batteries (LMB)

The solid electrolyte interphase (SEI) is a passivation layer formed on the electrode surface exposed to the electrolyte. The SEI concept was initially suggested by Peled to describe the interphase emerging on the alkali and alkaline earth metals electrode in contact with non-aqueous electrolytes [34]. Subsequently, the presence of SEI has been observed on other electrodes and has thus been relevant for lithium ion or lithium sulphur batteries [16, 35-37]. The formation of SEI hinders further direct contact between electrode and electrolyte and suppresses further decomposition of the electrolyte components. Ideally, the SEI is composed of compounds which are ionically conductive in order to transfer the Li ion and avoid concentration gradient build up, and electronically insulating to prevent the further reduction of the electrolyte and final capacity fade. It is morphologically desirable for SEI to be thin and non-porous. However, the actual SEI on lithium metal electrodes typically does not show the above mentioned ideal characteristics and the electrolyte decomposition hardly ever completely stops leading to overconsumption of the available electrolyte and dendrite formation causing cell failure.

When the lithium electrode is exposed to a salt containing aprotic solvent, it typically reduces the salt anion and decomposes the solvent or even impurities such as H₂O due to its low negative standard reduction potential. The product of degradation would consequently precipitate on the lithium electrode as a mosaic of micro-phases, enabling the conduction feasible through the grain boundaries, Figure 2-6. Preferably the products of reaction are insoluble; nevertheless, the changes in the molar volume fraction during the redox reaction are unavoidable, leading to formation of the pores or cracks that increase the further decomposition [34]. In Lithium metal batteries using salt containing aprotic solvent compounds such as LiOH, Li₂CO₃, LiF, Li₂S

accompanied with organic species such as semicarbonate, ROCO_2Li , ROCOLi , ROLi are observed in SEI layer [38-43].

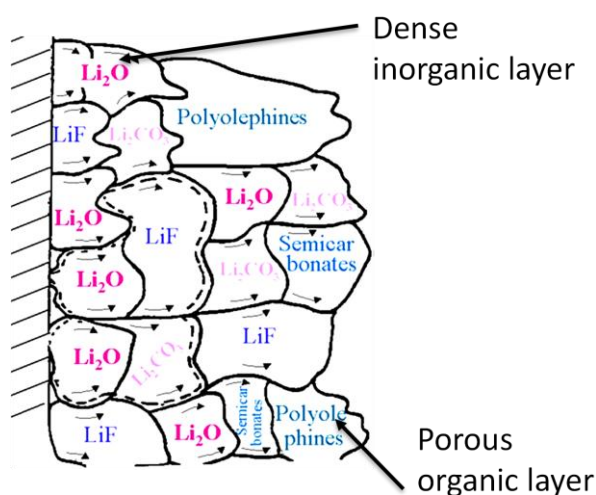


Figure 2-6 Schematic mosaic structure of SEI including organic and inorganic phases. The mosaic structure can have a bilayer form with an inner inorganic and outer organic layer [16].

In the mosaic model, the reduction of salt and solvent happens simultaneously resulting in a mixture of the insoluble organic-inorganic multi-phase passivation layer on the anode. It is reported that these micro-phases could under certain circumstances form a bilayer including inner inorganic phases and other organic based compounds, meaning the solvent molecule and salt ion do not diffuse through the SEI layer [38]. Therefore, the growth of SEI occurs at the SEI/electrolyte interface rather than the anode surface. In this model, the growth process occurs in 2 steps, resulting in the formation of a compact inorganic SEI and later on the growth of the secondary porous organic SEI as a consequence of further electrolyte reduction. Several modification to SEI model including polymer electrolyte interphase (PEI) and solid polymer layer (SPL) have been proposed [44, 45]. Furthermore, it is observed that pure lithium accompanied with a native passivation film on the surface exists even in a dry inert atmosphere, introducing new aspects to the formation and growth of the SEI [38]. From the literature on the solid state reactions, it is clear that chemistry and morphology depend critically on the involved compounds and the system parameters, exhibiting manifolds of mechanism [46].

2.3.2 Charge Transfer in SEI

In the simplest and ideal case, the SEI is not porous and the ionic transport occurs only through the inorganic part. Ideally, in this layer $t_{Li} = 1$ and $t_e = 0$. In such a system, the transfer of ions from the bulk of the electrolyte to the anode involves at least 3 steps as it is illustrated in Figure 2-7. Initially, solvated Li^+ strips off its solvation shell and transfers through the electrolyte/SEI interface and reaches the SEI. In the SEI, the charge transport takes place via mobile point defects namely vacancies or interstitial defects.

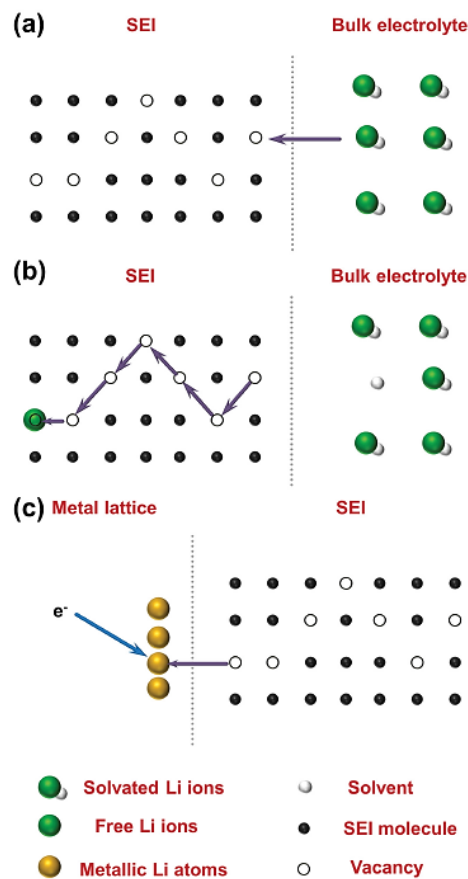


Figure 2-7 Highly simplified charge transfer mechanism at electrolyte/ SEI, SEI, SEI/ electrode interfaces. Each step could be the rate determining step [40].

Eventually, the Li^+ reaches the anode surface where the electron uptake leads to deposition of lithium metal on the anode. Kinetically, it is interesting to investigate

which step in the Li^+ charge transfer process is rate-limiting. When the SEI is thick and not damaged the migration through the SEI itself is most probably, kinetically least favourable step. In a real system, involved electric fields influence predominantly the interfacial effects, thus the transfer properties can be very complicated.

2.3.3 SEI and Dendrite Formation

SEI formation on graphite or silicon anodes of lithium ion batteries has been vastly investigated. Graphite anode SEI is fairly stable enabling its application in commercialized batteries. However, achieving stable SEI layers on the silicon anodes is more challenging due to the substantial volumetric changes during intercalation/deintercalation. In lithium metal batteries on the other hand the formation and growth of lithium dendrite is a severe complication caused by unstable SEI. The constant stripping-plating of lithium underneath the SEI during electrochemical cycling can lead to fracture of the passivation layer and formation of pathways for the reactive lithium metal to grow, Figure 2-8 [47-51].

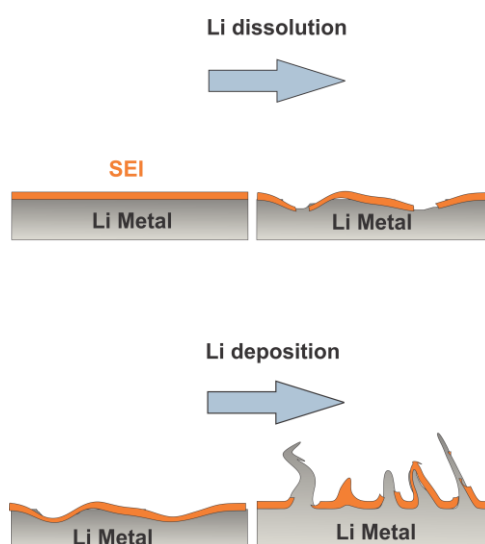


Figure 2-8 Removal and re-deposition of the Li ion underneath the SEI layer causes a crack and forms the passage for the reactive lithium metal to grow through.

The deposited lithium can grow in a dendritic or mossy form [52-54]. The needle-like dendrites will eventually short-circuit the cell, which is hazardous for the safety of the

battery, while the mossy dendrite increases the SEI impedance along with a more excessive Li consumption and potential final cell failure [55]. Furthermore, the crack and growth of the deposited lithium can also lead to the formation of isolated (dead) lithium, which is physically attached to lithium electrode while electrochemically disconnected and severely lowers the capacity [56]. The cracking of SEI and the structure of deposited lithium depend on various parameters including composition, thickness, elasticity, ionic and electronic conductivity of the SEI, as well as applied current density and separator mechanical strength [55, 57-59].

2.3.4 SEI Modification

According to the mentioned issues, a stable and purely ionically conductive interphase between anode and the electrolyte is crucial for the cyclability of the LMB. In this respect, two different general approaches have been employed to form a stable SEI layer: 1) tuning the electrolyte composition including solvent, salt or additives 2) growth of the artificial SEI.

The choice of the solvent appears to be critical, given that it is the main provider for organic phases within the SEI. Different kind of solvents have been investigated. Ether based solvents are suggested to perform reasonably well, as they are comparably stable toward lithium due to their relatively low oxidation potential [60]. In particular cyclic ethers such as 1,3-dioxolane (DOL) have shown superior cyclability due to the ability to form more flexible SEI as their reduction products include elastomers which are insoluble and adhere well to the lithium [61]. Similarly, the salt anion can be varied to manipulate the final composition of the SEI. It has been concluded the salts with higher ionic conductivity, simultaneously composed of the anion, allowing the formation of flexible structures, are the best options [62, 63].

Employing the additives with higher reduction voltage than electrolyte component such as fluoroethylene carbonate (FEC) and LiNO_3 is reported to have a beneficial effect on SEI stability [40, 64, 65]. These additives will react quickly with the lithium anode and form a favourable F and N-rich passivation layer that is more stable than the

degradation products of organic solvents and lithium salts.

Pre-passivation methods using liquid or gaseous phases to form an ex-situ passivation layer have been vastly explored. Pre-passivation of the lithium metal with siloxane-based solution, ionic liquid such as *N*-propyl-*N*-methylpyrrolidinium bis(fluorosulfonyl)imide is proposed to stabilize the SEI [66-68]. Passivating lithium with ceramics such as Al₂O₃ using atomic layer deposition (ALD) has been studied to prevent lithium corrosion [69, 70]. Exposure of lithium metal anodes to different gases such as N₂ to form Li₃N film and or exposure to fluoropolymers to obtain LiF films on have been investigated, with some indication of dendrite formation suppression [71-73]. Nevertheless, the artificial SEI are usually more fragile and incapable of self-recovering.

Chapter 3 Glyme-based Electrolyte in Contact with Mica

3.1 Experimental

3.1.1 Materials

Glyme

Glymes, shown in Figure 3-1, are liquid polyethers with low molecular weight ($M_w < 1000$). These dipolar aprotic solvents are chemically rather inert towards lithium in comparison to solvents such as alcohols and phenols due to the absence of hydroxyl groups.

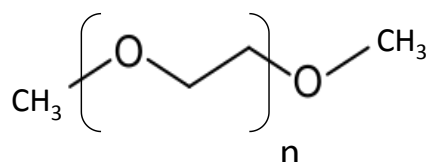


Figure 3-1. Molecular structure of glymes.

Different glymes and their typical physical and chemical properties are represented in Table 3-1 [74]. Glymes have shown many favourable properties including a wide liquid range, relatively low vapour pressure, low viscosities, and high chemical and electrochemical stability

Table 3-1 Physico-chemical properties of different glymes.

n	Common Name	Density(g/mL) at 25 C°	Boiling Point (C°)	Dielectric constant at 25 C°
1	Monoglyme(G1)	0.86	85	7.18
2	Diglyme(G2)	0.93	182	7.4
3	Triglyme(G3)	0.98	218	7.6
4	Tetraglyme(G4)	1	275	7.8

Among all physical and chemical properties of glymes, there are two features of great importance to this research. The low dielectric constant that provides a high level of ion association with shorter chains showing higher degree of association. This provides the means to investigate the formation of the double layer and ion dissociation phenomena at interfaces. Another feature is the ability of the glyme solvent to complexate alkali ions. This is due to the presence of ether-type oxygen atoms in the glyme molecular structure [75, 76].

Tri (ethylene glycol) dimethyl ether ($M_w = 178.2 \text{ g mol}^{-1}$, Sigma Aldrich, triglyme), was distilled prior to use (water content less than 150 ppm measured using Karl-Fischer titration) and kept in the glove box under argon atmosphere.

Lithium Trifluoromethanesulfonate (LiTf):

Lithium triflate (LiCF_3SO_3), with the molecular structure shown in Figure 3-2, is a common lithium salt showing potential application as an electrolyte component in lithium metal batteries [63]. Lithium triflate has a rather high solubility in glymes, and offers conductivities as high as 0.6 mS cm^{-1} in diglyme at 1 M concentration [77].

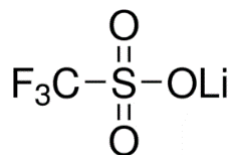


Figure 3-2 Molecular structure of the lithium triflate salt.

Ion association of this salt in various solvents has been investigated using infrared (IR) or Raman spectroscopy as the frequencies and intensities of the Tf anion vibrational modes are sensitive to the ion-ion interactions, leading to the observance of different ionic species contributions in the spectra [77, 78].

Muscovite Mica:

Muscovite mica is a hydrated aluminium potassium silicate mineral. Mica with the formula of $\text{KAl}_2(\text{AlSi}_3)\text{O}_{10}(\text{OH})_2$ has a layered structure, illustrated in Figure 3-3, consisting of one layer of AlO_6 octahedral, sandwiched by two layers of tetrahedral alumina silicate $((\text{Si}, \text{Al})\text{O}_4$ [79, 80]. The surface of air-cleaved mica is usually terminated by K^+ ions, favouring anion adsorption and enabling easy cation exchange.

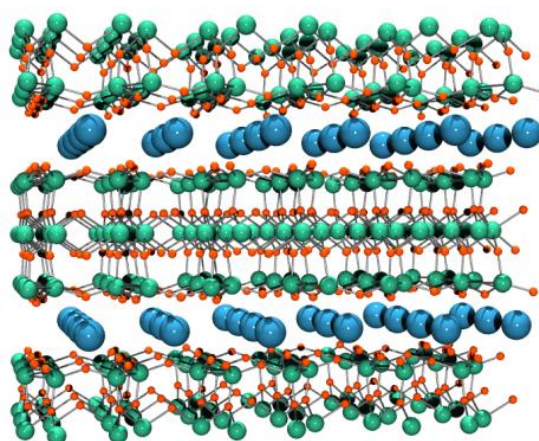


Figure 3-3 Crystal structure of muscovite mica. The oxygen atoms are depicted red, the potassium ions are depicted in blue, and the aluminium/silicon atoms are depicted green.

3.1.2 Surface Force Apparatus (SFA)

Surface force apparatus (SFA) is a technique allowing a direct measurement of the interaction forces between two surfaces when they approach or retract from each other as a function of distance with angstrom level resolution [81, 82]. The SFA has been employed in various fields to measure the physical forces between surfaces, including van der Waals, electrostatic forces, adhesion and capillary forces, solvation and hydration forces.

Figure 3-4 depicts the major part of the SFA setup. The two mica surfaces are allocated on curved glass discs mounted in a crossed-cylinder geometry. The mica sheets are backside-coated with a 40 nm thick silver layer as a reflective mirror. When the white light falls on the back-silvered molecularly smooth mica, it behaves as an interferometer. The transmitted light is directed towards a spectrometer, which gives rise to a series of fringes of equal chromatic order (FECO).

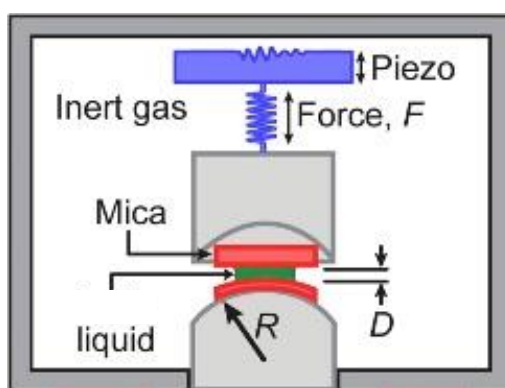


Figure 3-4 Simplified SFA setup showing the major parts of the instrument [83].

This setup of the mica behaves as a partially transparent and reflective system, meaning the irradiated light will pass through the bottom mica and reflect by the silver coating on the upper mica which acts as a mirror.

Figure 3-5 shows the FECO in a distance versus wavelength plot for the two mica sheets facing each other in the two states of distanced (top) and in contact (bottom).

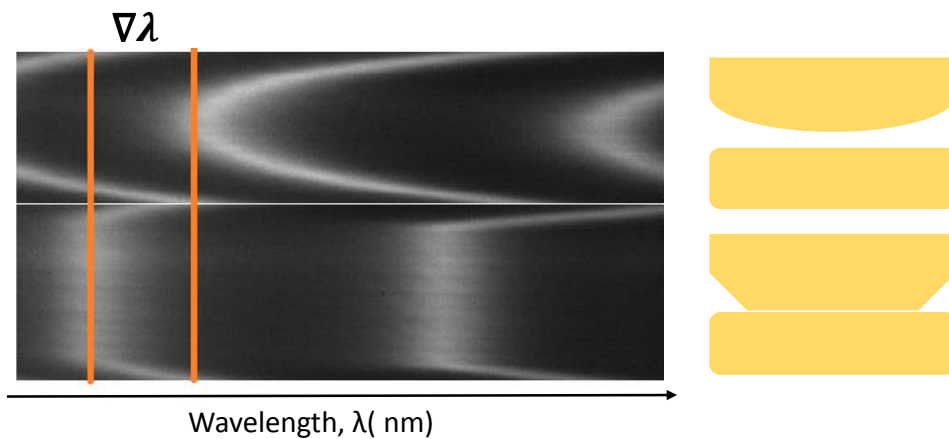


Figure 3-5 Fringes of equal chromatic order (FECO) reveal the information about the distance between the two mica surfaces in SFA. Top: Surfaces separated from each other. Bottom: Surfaces in contact with each other. The wavelength shift between the contact and the separated surfaces is shown between the two red lines [84].

With positioning the disks in complete contact (zero position), one would be able to track the change in the separation distance between two disks with angstrom resolution using shifts in FECO wavelength. The transmitted wavelengths (FECO) can be related to the distance between mica sheets (D) by:

$$n\lambda = 2D \quad \text{Equation 3-1}$$

Muscovite mica offering a molecularly smooth surface should be coated with the silver layer using physical vapour deposition (PVD) and cleaved down to 2 or 3 μm for SFA experiments. The prepared mica sheets are subsequently glued to the curved glass cylinders with the same radius value. The cylinders are positioned to each other in the crossed orientation, which can be considered equivalent to the flat surface in interaction with the cylinder.

As it can be observed from Figure 3-4, the bottom disc is mounted on a double cantilever spring, which is accountable for the force measurement. The upper disc is mounted on a piezo-electric tube, which is responsible for the separation or approach

of the two surfaces. The liquid is injected between these two surfaces. Upon the approach of the two discs, the appearance of any forces would be observed as deflection in the spring. The forces F are then calculated using the displacement D and the constant of the double cantilever spring k [85]:

$$\Delta F(x) = k(\Delta D_{\text{applied}} - \Delta D_{\text{measured}}) \quad \text{Equation 3-2}$$

The measured force can be translated to the interaction energy (E) using the Derjagun theory [86]:

$$F = 2R\pi E \quad \text{Equation 3-3}$$

where R is the radius of the utilized cylinder.

The rate of the movement and the curvature of the disc can be optimized in the SFA measurement to obtain favourable sensitivity.

The SFA setup has been used to study solid-liquid systems including polymers and ionic liquids. In this study, force-distance characteristics of the pure triglyme and LiTf consisting triglyme solution at ca. $1000 \mu\text{m}^2$ contact area were investigated using a Surface Force Apparatus 2000 (SurForce LLC, Santa Barbara, U.S.A.). The SFA runs are implemented under controlled environment at 22°C and Argon gas purging during and 30 min prior to the experiment. The electrolytes were then injected between the opposing surfaces of the 3-layer interferometer setup by syringes when two mica surfaces were contacted. The SFA experiments were performed using two different approach rates of the discs. Faster speeds of 2.5 nm s^{-1} allowed the observation of the initial interfacial structuring, while low semi-static compression speeds of 0.2 nm s^{-1} allowed studies of systems under equilibrium, avoiding hydrodynamic effects.

The SFA measurements have been done in collaboration with Prof. Markus Valtiner and Dr. Hsiu-Wei Cheng (department of interface chemistry and surface engineering) at the Max Planck Institute for Iron Research in Düsseldorf.

3.1.3 Zeta Potential (ζ)

Zeta potential (ζ) is the electric potential at the slipping plane in the double layer relative to the bulk of the medium. Slipping or shear plane is defined as the plane that within the ions are stationary due to the strong adsorption. Normally, the zeta potential resembles the potential at the OHP or at the beginning of the diffuse layer [87]. The zeta potential is typically measured based on electro-kinetic phenomena such as streaming potential, electrophoresis and electroacoustic effect.

In this study, the electroacoustic method has been employed to determine ζ . Here, an ultrasonic wave created by a piezoelectric transformer is used to induce a motion in the charged particles relative to the solvent. This displacement polarizes the double layer inducing an electric field that can be measured either as a colloid vibration potential (CVP) or as colloid vibration current (CVI).

The CVI can be translated to electrophoretic mobility, μ_d [88, 89]:

$$CVI = A \frac{\rho_p - \rho_m}{\rho_m} \varphi \mu_d \nabla P \quad \text{Equation 3-4}$$

where ρ_p is the particle density, ρ_m is liquid density, ∇P is the pressure gradient of the sound waves and A is the cell constant. Electrophoretic mobility is connected to zeta potential through:

$$\mu_d = \frac{2\varepsilon_m \zeta}{3\eta} f(\kappa a) \quad \text{Equation 3-5}$$

where ε_m is the dielectric constant of the liquid, η is the viscosity of the liquid, $f(\kappa a)$ is the Henry's function which is dependent on double layer thickness.

An electroacoustic DT-1200 spectrometer (Dispersion Technology, Inc., Quantachrome) was used to measure the CVI at 3 MHz.

3.1.4 Infrared Spectroscopy (IR)

Room temperature IR spectra were recorded using Bruker IFS 66 v/S spectrometer under purged N₂. The Harrick liquid transmission cell with ZnSe windows was filled with the electrolyte in the Argon purged glove box. The spectral resolution was 1 cm⁻¹ using 150 scans per measurement. The peaks corresponding to the triflate stretching band were fitted with MagicPlot Pro 2.5.1 software using a mixed Gaussian-Lorentzian function and a linear baseline. This software estimates the area under each band and calculates the fraction of each corresponding species by dividing its associated area by sum of areas. The concentration of each species can be calculated multiplying the fraction of that species with the total concentration. To be able to extract quantitative information from IR spectra, the Beer law should be applied, meaning the absorbance should be linearly proportional to the concentration. An important presumption is that the absorption sensitivities for the relevant peaks are the same. This presumption obviously implies that the summed area is proportional to the total concentration, fulfilled for this system shown in appendix A Figure 1 [78].

3.1.5 Impedance Spectroscopy (IS)

A temperature controlled (RC6CP Lauda thermostat) ac-impedance spectroscopy is carried out in the frequency range from 10⁻¹ to 10⁷ Hz (0.1 V amplitude) using a Solartron 1260 frequency analyser to measure the conductivity of the various electrolytes in a previously developed gold-plated cell [90].

3.1.6 Rheology

A Malvern KINEXUS Pro+ device with a plate–plate configuration (upper plate d = 60 mm) and 350 μm gap distance has been employed to measure the viscosity in the shear rate range of 10–100 s⁻¹.

3.2 Results and Discussion

3.2.1 IR

Information on the molecular structure and concentration of different molecular species in LiTf/ triglyme electrolytes with regard to salt concentration and addition of the ceramic filler is obtained using the triflate IR stretching band. Figure 3-6 indicates the $-\text{CF}_3$ symmetric deformation mode in IR spectra of the 1M LiTf/triglyme.

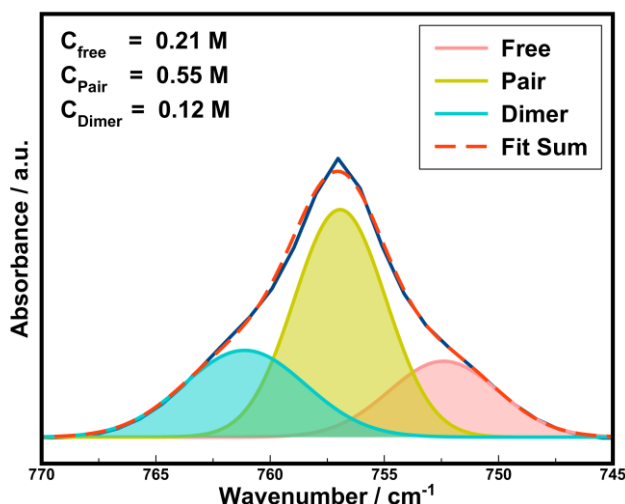


Figure 3-6 Infrared spectra of the triflate stretching band for 1M LiTf/triglyme electrolyte. The concentration of the free ions (green), ion pairs (purple) and dimers (orange) has been determined from the Gaussian-Lorentzian fit (dashed red line) of the total measured spectra (continuous blue line).

Both the peak positions and the relative areas can provide information about ion pairing in the liquid electrolytes. The three bands detected in this region are attributed to Li-Tf ion pairs (at 757 cm^{-1}), free Tf ions (753 cm^{-1}) and Li_2Tf_2 dimers (761 cm^{-1}) [77, 78]. The concentration of different species has been calculated using the total concentration value as explained in the experimental part of this chapter.

The fraction of these molecular species appears to be dependent on the c_{salt} , as the evolution in the vibrational frequency of CF_3 mode of triflate is observed in Figure 3-7, upon change in the concentration. The decrease in the c_{salt} from 1 to 0.2 M leads to the decrease of the ion pair fraction from 55% to 48% accompanied with the enhancement

in free ion fraction from 21% to 30%.

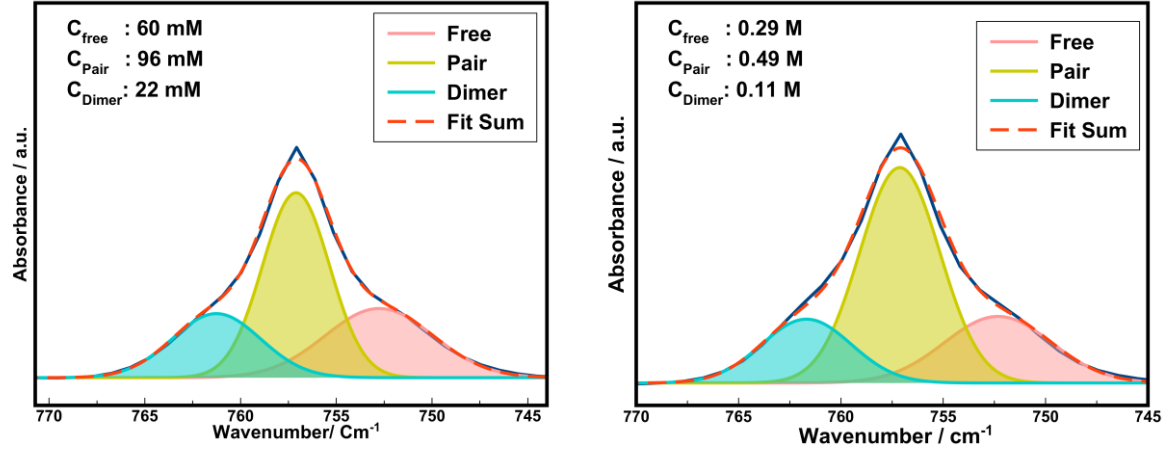


Figure 3-7 Infrared spectra of the triflate stretching band for left) 0.2 M LiTf/triglyme Right) 0.5 M LiTf/triglyme.

For ion pair dissociation in LiTf/triglyme, it holds that:

$$K_{diss}^{pair} = \frac{(\gamma_{Li^+})(c_{Li^+})(\gamma_{Tf^-})(c_{Tf^-})}{(\gamma_{LiTf})(c_{LiTf})} \quad \text{Equation 3-6}$$

where K_{diss}^{pair} is the respective mass action constant, c_i is the molar concentration of species i , and the concentration of the anion and cation are equal:

$$c_{Li^+} = c_{Tf^-} = c_{free} \quad \text{Equation 3-7}$$

Furthermore, mass balance requires:

$$c_{Li^+} + c_{LiTf} + 2 c_{Li_2Tf_2} = c_{salt} \quad \text{Equation 3-8}$$

with $c_{Li_2Tf_2}$ represents the concentration of dimers(Li_2Tf_2).

The activity coefficients of species i (γ_i) and in the Debye-Hückel range can be calculated using:

$$\gamma_{\pm}^2 = \frac{-2z_+z_- p\sqrt{I_M}}{1+qa\sqrt{I_M}} \quad \text{Equation 3-9}$$

where z_+ and z_- are cation and anion charges, respectively. The parameter a is the

average minimum distance between cation and anion in triglyme-LiTf (calculated to be 14\AA), and I_M is the ionic strength. Considering the charge of the lithium and triflate ions as well as Equation 3-7 results in:

$$I_M = \frac{1}{2}(z_{Li^+}^2 c_{Li^+} + z_{Tf^-}^2 c_{Tf^-}) = \frac{c_{Li^+} + c_{Tf^-}}{2} = c_{free} \quad \text{Equation 3-10}$$

The parameters p and q in Equation 3-9 are defined as [91]:

$$p = (2\pi N_A)^{1/2} \left(\frac{e^2}{5\pi\epsilon_0 \epsilon k_B T} \right)^{3/2} \quad \text{Equation 3-11}$$

$$q = e \left(\frac{2\pi N_A}{\epsilon_0 \epsilon k_B T} \right)^{3/2} \quad \text{Equation 3-12}$$

where, N_A is Avogadro constant, e is the proton charge, ϵ_0 is the permittivity of vacuum, ϵ is solvent dielectric constant, k_B is the Boltzmann constant and T is the absolute temperature. The γ values for the neutral species are set to 1. The calculated values of γ_{\pm}^2 and K_{diss}^{pair} for these three concentration of LiTf in triglyme are given in Table 3-2.

It appears that K_{diss}^{pair} is not constant and decreases with increasing c_{salt} , indicating that the Debye-Hückel regime has been considerably exceeded.

Table 3-2 The γ_{\pm}^2 and K_{diss}^{pair} calculated for different concentration of LiTf in triglyme.

Concentration/ M	γ^2	$K_{diss}^{pair} / \text{mol m}^{-3}$
0.2	0.010	0.80
0.5	0.011	0.71
1	0.015	0.59

However, as already explained, addition of fillers to liquid electrolyte changes c_{free} and c_{pair} , meaning that in 1M LiTf/triglyme doped with mica particles, owing to interfacial effect, Equation 3-7 is not valid anymore. In this case:

$$n_{Li^+} = n_{Tf^-} + n_s \quad \text{Equation 3-13}$$

where n_s is the overall number of adsorbed anions on the surface of particles. If this is considered equal to the amount of number of OH groups available on the surface in an ideal system, the molar concentration of the adsorbed anion (c_s) can be asserted using the total volume (V) of particles:

$$c_s = \frac{n_s}{V} = \frac{3\phi}{N_A a_s r} \quad \text{Equation 3-14}$$

Here, ϕ is the volume fraction and r is the radius of added particles, N_A the Avogadro constant, a_s is the surface area on the mica occupied with adsorbed ions calculated to be 0.1 nm^2 taking into account the 5 nm^{-2} as the density of the surface -OH groups.

Such estimated c_s indicates that visibility of the changes in concentration of different ionic species requires relatively high volume percent of particles. Indeed, in the case of mica, as it dissociates a smaller amount of Li-Tf ion pairs due the larger particle size of $d \approx 150 \text{ nm}$ after 1h ball-milling, Figure 3-8, an enhancement in the dissociation in IR Spectra would be observable for volume fraction of particles above 4 vol %, which was unfortunately not feasible experimentally due to the lack of transparency in such dispersions.

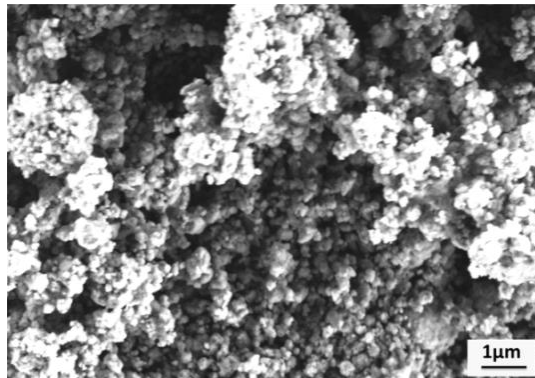


Figure 3-8 SEM image of dry ball-milled mica particles [92].

3.2.2 Viscosity, Zeta Potential and Conductivity

Figure 3-9 shows the viscosity measurement of 1 vol% Mica: (1 M LiTf/triglyme) that is independent of shear rate, indicating absence of gel formation. Simultaneously, dynamic light scattering (DLS), shown in appendix (A Figure 2) reveals agglomeration of mica in 1M LiTf/triglyme.

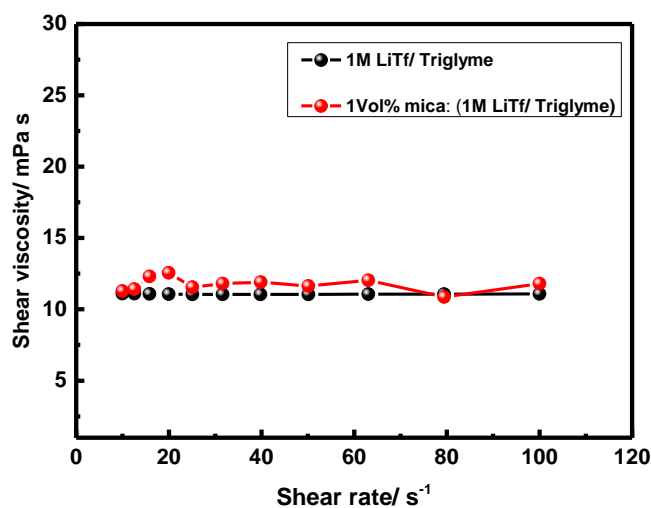


Figure 3-9 Shear viscosity of 1 M LiTf/triglyme compared to 1 vol% Mica: (1 M LiTf/triglyme) [92].

In order to determine the surface charge of the mica particles in 1M LiTf/triglyme electrolyte the zeta potential technique was employed. Figure 3-10 represents the effective zeta potential (ζ_{eff}) of 1 M LiTf/triglyme as a function of mica volume fraction. As it can be seen, in this system, ζ_{eff} is negative for all volume fractions indicating predominant anion adsorption on the surface of mica. A ζ_{eff} value of -48 mV is observed at 1 vol%, which decreases by increasing volume fractions until it reaches -7 mV at 6 vol%. The changes in ζ_{eff} are strongly influenced by the enhancement in the effective size via particle agglomeration and do not represent the local behaviour.

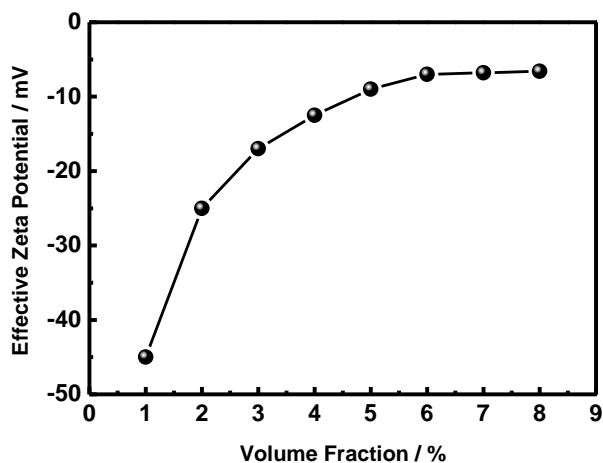


Figure 3-10 The effective Zeta potential of 1M LiTf/triglyme as a function of mica particle volume fraction [92].

The measured total AC-conductivities of the pure 1M LiTf/triglyme electrolyte and the one containing 1 vol% of ball-milled mica particles are given in Figure 3-11. A small decrease in conductivity from 1 to 0.9 mS cm⁻¹ is observed by addition of mica to 1M LiTf/ triglyme.

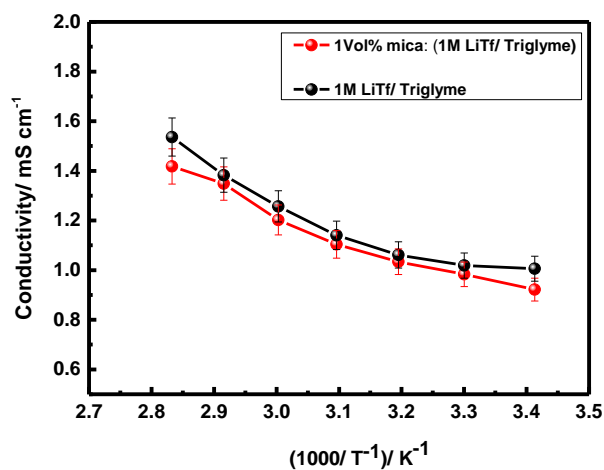


Figure 3-11 Temperature dependent ac-conductivity 1M LiTf/triglyme and 1 vol% Mica: (LiTf/triglyme).

Although zeta potential measurements indicate preferential adsorption of anion on the mica particles surface, there is no enhancement in the ionic conductivity due to the lack of percolating pathways which is crucial for good overall electrochemical performance.

3.2.3 SFA

Figure 3-12 illustrates force versus distance characteristics (FD-characteristics) of pure triglyme with respect to mica interface. FD-characteristics were acquired 5, 30, 120 and 240 minutes after introduction of the liquid in the SFA setup. After injection of triglyme, FD-characteristics were recorded with fast approach rates, maintaining a time resolution that can capture potential changes of the interfacial structuring.

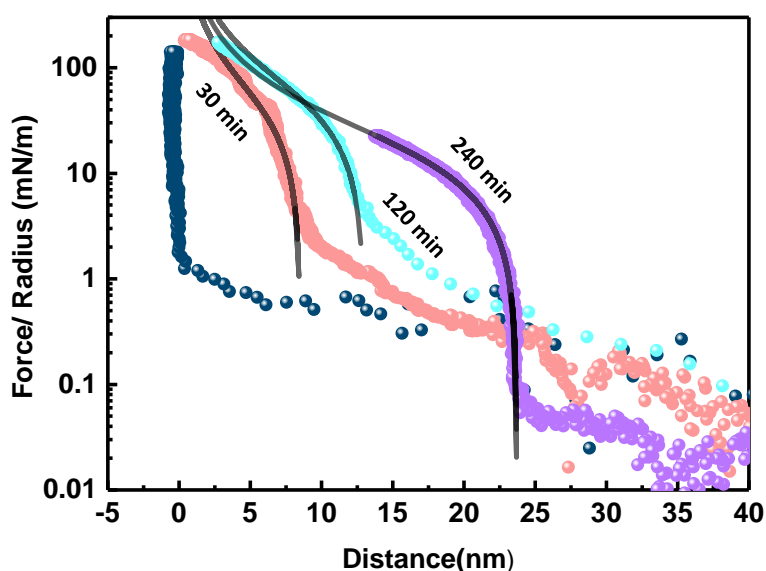


Figure 3-12 Force distance plot of specific interactions between two mica surfaces in contact with the pure triglyme and corresponding interfacial structuring through time. Black lines are the fitting curves according to de Gennes theory describing the force-distance characteristics across two approaching cylindrical surfaces covered with interfacially bound polymer layers [92].

The initially measured FD profile shows no specific liquid structuring between two mica surfaces, indicating that the polymeric solution was squeezed out when the pressure was higher than 2 mN m^{-1} (blue line). A prominent interfacial structuring appears during 30 min which is the essential time needed to record a slow quasi-static compression. This structure continually grows in subsequent scans, and eventually equilibrated with a 24 nm thick polymeric layering between two opposing mica surfaces. Interestingly, the characteristic compression profiles seen in the semi-

logarithmic plot in Figure 3-12 are analogous to the formation and growth of the immobilized brush-like polymeric structures, observed in SFA experiments in pure polymer systems [93]. The formation of a polymeric layer at mica interfaces is most likely related to a charging and complexation through the surface K^+ , as depicted schematically in Figure 3-13. In fact, it has been previously reported that glymes form tetra-coordination complexes with alkali metals via Arrhenius acid/base reactions [74]. The growth of a polymeric network is limited by the surface charge. For the sake of the charge neutrality, the K^+ should remain in the vicinity of the surface, causing polymer growth suppression through time.

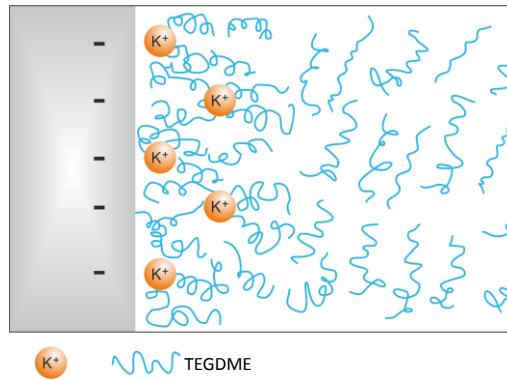


Figure 3-13 Brush-like polymer layer growing due to K^+ complexation centers [92].

The formation and growth behaviour of such brush-like polymer layers have been analysed by de Gennes theory, which can be employed here to describe the compression of the glyme across a symmetric mica interface [94]:

$$F(D)/R = \frac{2\pi k_B T}{s^3} \left[\frac{4}{5} D \left(\frac{2L}{D} \right)^{9/4} - \frac{4}{7} D \left(\frac{D}{2L} \right)^{3/4} \right] \quad \text{Equation 3-15}$$

where D is the separation distance between two mica surfaces, s is the mean distance between two immobilized polymer structures, L is the thickness of the polymer layer, T is the temperature and k_B is the Boltzmann constant. The brush-like polymer layer will grow constantly over 240 min from 3.8 nm up to 10.6 nm, Table 3-3. Nevertheless, the model and the experimental data deviates at higher force values, implying the weak breakable coordination bond between the mica and polymer.

Table 3-3 Fitted properties of the polymer layer growing between two opposing mica surfaces in pure triglyme as a function of immersion time.

Parameter	30 min	120 min	240 min
Layer thickness, L (nm)	3.8	5.8	10.6
Mean distance, s (nm)	1.6	1.7	3.0

In stark contrast, the interfacial structuring changed substantially after addition of LiTf salt above 0.2 M concentrations. Figure 3-14 compares SFA FD-characteristics of 0 M, 0.2 M and 1.0 M of LiTf concentrations in triglyme.

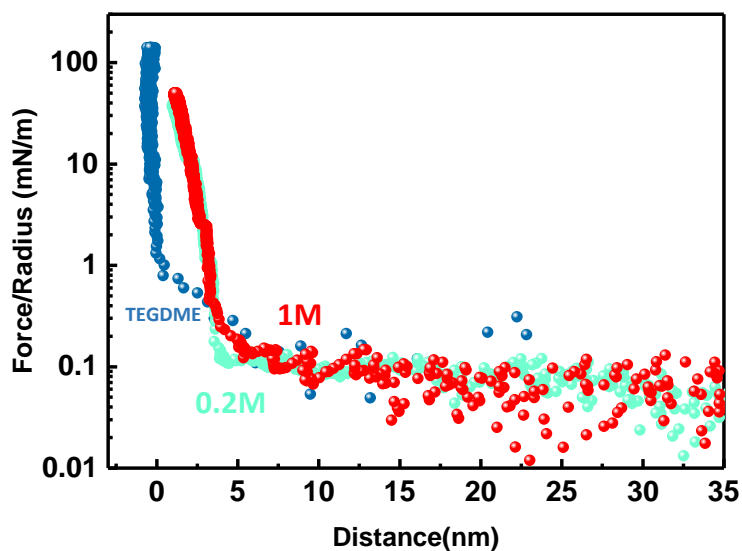


Figure 3-14 Force distance plot of specific interactions between two mica surfaces in contact with pure triglyme (blue), 0.2M LiTf/triglyme (green), and 1M LiTf/triglyme (red).

In these systems contrary to pure triglyme, a 15 nm thick layer with two distinct regimes was recorded during compression with no indications for interfacial polymer growth were observed. This reveals a transition of the interfacial structure formation from a polymeric structure to a structure that indicates specific ion adsorption in an inner and

outer diffuse layer. Figure 3-15 depicts the suggested structure of the formed electrical double layer on the mica surface in contact with such electrolytes considering the negative net charge on the surface observed in zeta potential measurement. The inner layer most likely consists of solvated triflate anions that have an estimated radius in the range of 13-15 Å. The diffuse layer with weak force outside the surface adsorbed anion layer ($D > 4$ nm), indicates further layering of larger ionic species.

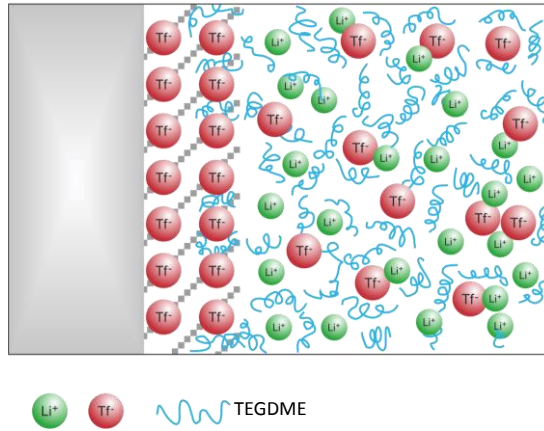


Figure 3-15 Schematic of interfacial structuring on mica surface exposed to LiTf/triglyme electrolyte [92].

In order to understand the formed electrical double layer structure in the vicinity of mica surface and its influence on the degree of ionic dissociation, Debye length values have been evaluated both experimentally (from the SFA and IR measurements) and theoretically from the *DH* theory. In force-distance profiles, further in the long range distances, where the *GC* model can be more confidently applied, the value of the Debye length can be measured by fitting the measured force to a linearized *PB* equation of electrostatic double layer interaction potential [95]:

$$\frac{F(D)}{R} = 2\pi E = \frac{8\pi e^2 n}{k_B T \kappa} \frac{\psi^2 (1 - \exp(-\kappa D))}{\exp(\kappa D) - \exp(-\kappa D)} \approx \frac{8\pi e^2 n}{k_B T \kappa} \psi^2 \exp(-\kappa D) \quad \text{Equation 3-16}$$

where $\kappa^{-1} = \lambda_{SFA}$ is the effective Debye screening length, D is the distance between two mica sheets, ψ is the diffuse double layer potential, T is the temperature, e is the elementary charge, n is the number density of dissociated ions, and k_B is the Boltzmann constant.

To study the long range forces and diffuse layer decay length, experiments with a mica approach rate of 0.3 and 2 nm s⁻¹ for the 0.001-1 M LiTf concentrations are performed. Herein, mica surfaces with larger radii (lower curvatures) ($R = 2$ cm) have been used as this increases the measurements precision in the long range regime of the F-D profiles. Figure 3-16 represents two subsequent run and corresponding exponential decay fits for 1 and 0.001 M LiTf. The fitted Debye lengths λ_{SFA} are around 8 nm for salt concentration ($c_{salt} \geq 0.2M$).

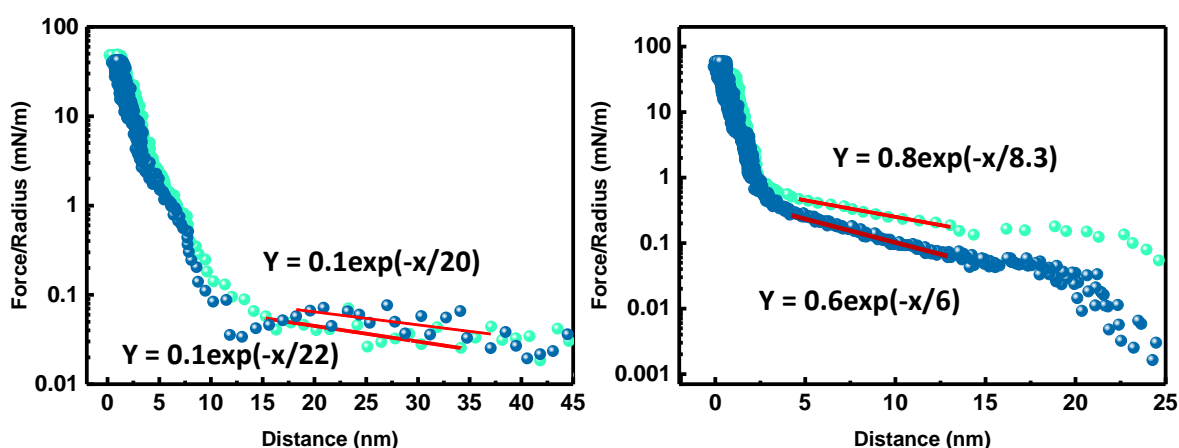


Figure 3-16 Two subsequent recorded SFA force-distance of Mica sheets in contact with triglyme (black and green) and the corresponding fitted exponential decay (red) for LiTf concentrations: a)

1mM, b) 1 M[92]. The $\frac{F}{R} = Y$ and the distance= X .

The SFA F-D profile and fitted exponential decay for other concentration are illustrated in appendix (A Figure 3). To exclude the observed polymer growth (under 10 nm) for lower salt concentration including 0.01 M and 0.001 M LiTf in triglyme, the exponential decay is fitted in the 15-40 nm range [92].

The theoretical λ values are calculated using the classical concept of electrostatic interactions in electrolytes that has been already discussed in chapter 2.1. Assuming a completely dissociated system in 1M LiTf/ triglyme (purely free ion contributing to formation of diffuse layer) with a dielectric constant of 7.5, would yield a λ_{calc} of 0.1 nm. Inserting free ion concentration values obtained from IR experiments would result in similar λ_{IR} of 0.2 nm. Both of these values are an order of magnitude lower than λ_{SFA} as seen in Figure 3-17.

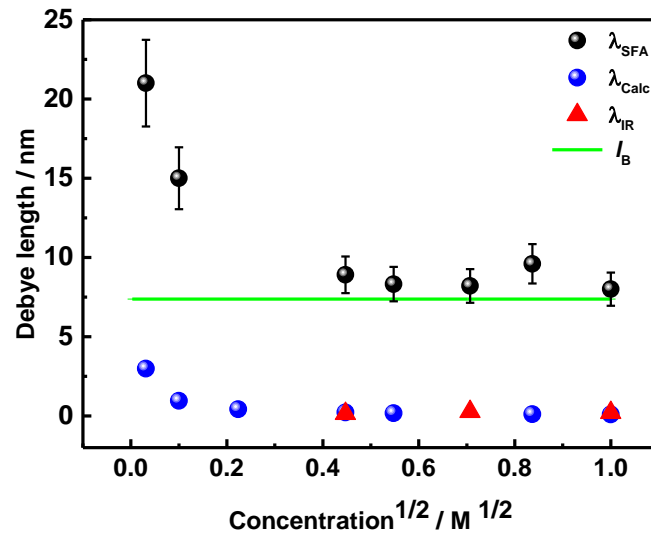


Figure 3-17 Debye length for solutions of LiTf/triglyme plotted as a function of $c^{1/2}$: measured by surface force measurements (black), using measured concentration of free ions by infrared spectroscopy (red) and calculated from DH theory (blue). The straight green line is the value of the Bjerrum length for the mentioned system [92].

The measured λ_{SFA} values are fairly higher than the Bjerrum length (Equation 2-9) for the concentrated electrolytes in this system, suggesting the mean field approach to be still applicable. The fact that very high λ_{SFA} values are measured for diluted systems with low ϵ_r is not surprising, as the values of screening lengths increase as l_B increases [96]. Even at concentration of 1mM, λ_{SFA} exceeds λ_{calc} , indicating non-ideal behaviour.

Additionally, the difference in concentration of free ions measured by IR and SFA most probably originates from their sensitivity to ion interaction. It appears that the true contact ion pairs are observable by spectroscopy while SFA is able to detect any other

kind of ion-ion interaction (or proximity), even in the longer interaction range.

In the references [97, 98] a statistical mechanical formalism for electrolyte systems was developed that provides a superior description of ion-ion correction in the concentrated systems. In this theory, instead of the bare ion in *PB* approximation, "dressed ions" have been considered. In this way, effective free ion concentration and dielectric constants have been renormalized in Equation 2-8 (*DH*) by taking into account non-local electrostatics. This concept should lead to more realistic values for the screening length. Crucial to this theory is the assumption that the ion density at one point in the solution is influenced by the electrostatic potentials in the whole neighbourhood of this point, rather than just the local value as assumed in *PB* approximation.

3.3 Conclusions

In the present chapter, the interfacial behaviour of pure and LiTf containing triglyme on cleaved muscovite mica has been investigated.

Pure triglyme primarily does not show interfacial layering. However, an interfacial layer forms and grows upon further SFA runs. The compression behavior appears identical to reported polymeric layer at mica interface. This is likely related to a charging and complexation of surface K^+ . The polymeric layer is immobilized by the surface charge on mica that evolves over 240 minutes during initial wetting.

The interfacial structure of LiTf/triglyme electrolytes comprises two distinct interfacial regions. An inner layer ranging from $D = 0$ to $D \sim 4$ nm is dominated with triflate anion based on the negative zeta potential. Consequently, an outer layer ranging from $D \sim 4$ nm to $D \sim 15$ nm consists of cation and ionic aggregates. It has been found that the thickness of the double layer is much higher than expected according to Debye-Hückel theory which can be explained considering distinct ion-ion correlation.

Chapter 4 Solid-Liquid Glyme-Based Composite Electrolyte

4.1 Experimental

4.1.1 Materials

Solid: Anodic Alumina

Anodic aluminium oxide (AAO) with the uniform nano-porous structure is fabricated through a self-assembling mechanism during a 2-step anodization of aluminium metal in acidic electrolytes [99, 100]. The fabrication process leads to the formation of porous hexagonally arranged pores. AAO has been vastly utilized as membrane, separator and template in energy storage systems due to the economical and controllable electrochemical anodization. In this study the nano-porous AAO ($d = 13 \text{ nm}$, $60 \text{ }\mu\text{m}$ thickness) Whatman Anodisc® was purchased from Sigma-Aldrich and has been utilized as the solid part of the electrolyte.

Liquid: Triflate/triglyme

0.02 - 1 M lithium trifluoromethanesulfonate (LiF_3CSO_3 , Sigma-Aldrich, 99.995%, LiTf) was dissolved in tri (ethylene glycol) dimethyl ether ($M_w = 178.2 \text{ g mol}^{-1}$, Sigma-Aldrich, triglyme, distilled prior to use, keeping the water content $<150 \text{ ppm}$).

The composite electrolyte has been prepared by infiltrating the nano-porous anodic alumina oxide with the solution of 0.02-1 M LiTf/triglyme.

4.1.2 Characterisation Techniques

The structures of the AAO monoliths and dendrite formed upon cycling were investigated using scanning electron microscopy (Zeiss Merlin operating at 5 kV). The

discoloured AAO after failure of the cell in stripping-plating experiment is crushed and dispersed in ethanol and subsequently deposited on carbon grids for transmission electron microscopy (TEM) measurements using JEOL, CM200. X-ray diffraction pattern was obtained using a Philips device with Cu Ka 1 ($\lambda = 0.154$ nm) radiation. A N₂ adsorption-desorption apparatus (BELSORP-mini II, Bel Japan Inc.) was operated to characterize the porosity of the AAO membranes. Samples were degassed overnight at 120 °C under vacuum beforehand. The ion exchange capacity of –OH groups on the surface of AAO has been determined employing potentiometric titrations. In this method the defined amount of the crushed AAO particles has been dispersed in a 0.1 M NaCl aqueous solution, stirred continuously for 1h, subsequently titrated by 0.01 M NaOH solution and back-titrated with a 0.01 HCl up to the neutral pH values [90].

4.1.3 Impedance Spectroscopy

One useful method to investigate the resistances and capacitances originating from the different processes such as bulk of liquid electrolyte or interfacial layer form on the electrode in contact with liquid electrolyte is the electrochemical impedance spectroscopy (EIS). EIS measures the alternating current $I(\omega)$ as a response to an applied alternating voltage $U(\omega)$ as a function of different frequencies typically ranging from the mHz to the MHz regime:

$$I^*(\omega) = I_0 \cos(\omega t) \quad \text{Equation 4-1}$$

$$U^*(\omega) = U_0 \cos(\omega t + \theta) \quad \text{Equation 4-2}$$

In Equation 4-1 and 2, ω is the angular frequency and θ is the phase shift. The complex impedance Z^* can be determined using:

$$Z^* = \frac{U^*(\omega)}{I^*(\omega)} = Z' - iZ'' \quad \text{Equation 4-3}$$

Plotting the negative imaginary part (Z'') versus the real part (Z') of the impedance gives the Nyquist diagram that can be evaluated by fitting it to an appropriate equivalent

circuit. The equivalent circuit includes capacitances and resistors to describe the electrochemical behaviour. In the simplest case where there is just the bulk response this equivalent circuit consists of a resistor parallel to a capacitor (RC). The complex impedance of this single RC parallel circuit is:

$$Z^* = \frac{R}{1+i\omega R} \quad \text{Equation 4-4}$$

The Nyquist plot of RC element appears as a semicircle with a radius of $(\frac{R}{2})$. The relaxation time (τ) of each process corresponding to the semicircle can be derived using the frequency at the maximum of the semicircle:

$$\tau = \omega_{max}^{-1} \quad \text{Equation 4-5}$$

However, in a real system normally processes such as interfacial layers or grain boundaries are involved which can appear as multiple contributions to impedance spectra depending on the relaxation times. In such cases, the impedance spectra can be fitted using several RC elements in series.

The ionic conductivity of the bulk (σ_{Bulk}) can be calculated using the fitted resistance (R_{Bulk}) obtained from diameter of the arc:

$$\sigma_{Bulk} = \frac{L}{R_{Bulk} A} \quad \text{Equation 4-6}$$

with L and A representing thickness and area of electrode, respectively.

Bulk capacitances (C_{Bulk}) can be derived from the maximum frequency (ω_{Max}):

$$\omega_{Max} = (R_{Bulk} C_{Bulk})^{-1} \quad \text{Equation 4-7}$$

However, the semicircles are usually depressed due to inhomogeneity or porosity, and in these cases it is possible to calculate the true capacitances (c_{Bulk}^{Tr}), taking into account the elements of the equivalent circuit according to:

$$c_{Bulk}^{Tr} = (C_{Bulk}^{1-\alpha} Q_{Bulk})^{1/\alpha} \quad \text{Equation 4-8}$$

where α and Q are parameters (CPE-P and CPE-T) from the corresponding fit of the semicircle.

Additionally, C_{Bulk} is related to the electrodes area (A) and the distance between the electrodes d_{Bulk} via:

$$C_{Bulk} = \epsilon_0 \epsilon_{Bulk} \frac{A}{d_{Bulk}} \quad \text{Equation 4-9}$$

where (ϵ_{Bulk}) is the dielectric constant of the medium. Similar relations are valid for interlayers such as SEI. Hence the thickness of the interfacial layer (d_{SEI}) can be calculated from the capacitances ratio with the assumption that the dielectric constants of SEI and bulk are identical:

$$\frac{C_{SEI}}{C_{Bulk}} = \frac{d_{Bulk} \epsilon_{SEI}}{d_{SEI} \epsilon_{Bulk}} \approx \frac{d_{Bulk}}{d_{SEI}} \quad \text{Equation 4-10}$$

Electrolytes were sandwiched between two lithium electrodes in a self-designed stainless steel cell. Impedance spectroscopy was recorded in the frequency range from 10^{-1} to 10^7 Hz (0.1 V amplitude) using a Solartron 1260 frequency analyzer. Temperature was controlled by a RC6CP Lauda thermostat. The spectra have been analysed using the *ZView* software. Figure 4-1 shows the typical recorded impedance spectra and fitted equivalent circuit in this study.

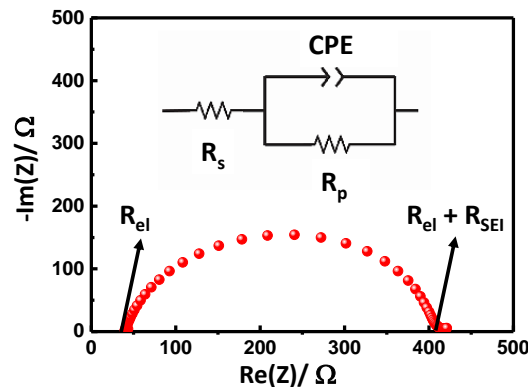


Figure 4-1 Typical impedance spectra recorded in the Li|AAO:(LiTf/triglyme)|Li cell and the corresponding fitted equivalent circuit.

4.1.4 Galvanostatic Polarization

The cation transference number (t_+) is one of the important electrochemical properties of the electrolyte with great relevance for high power application. The t_+ value represents the conductivity contribution of the free cation to the overall value in the electrolyte:

$$t_+ = \frac{\sigma_+}{\sigma_+ + \sigma_-} = \frac{\sigma_+}{\sigma} = \frac{R}{R_+} \quad \text{Equation 4-11}$$

with R_- being the anion and R_+ cation contributions to the R_{tot} .

A single ion conducting electrolyte ($t_+ \approx 1$) is favourable to avoid concentration gradients and suppress the cell failure.

In this study the galvanostatic polarization, which has been extensively used in solid state electrochemistry typically in terms of electron as counter carrier to the mobile ion, is used as transference number measurement. In this experiment, a constant current (I) is applied to a Li| electrolyte | Li symmetric cell, where lithium acts as a semi-blocking electrode (reversible to cations and blocking for anions). The time dependent voltage change is recorded until the steady state is reached (U_{ss}). Initially, both anions and cations start to migrate as a consequence of the voltage as a driving force. However, the anion flux is not supported by the blocking electrode and eventually stops at the steady states. Forced by electro-neutrality, the cations will flow to compensate the concentration gradient, meaning that the steady state voltage solely corresponds to the cation transport. From both initial IR jump and steady state respond the transference number can be obtained. Hence, it has to be paid attention to the fact the IR jump also contains contribution from the passivation layer formed on the electrode in contact with electrolyte, the so called SEI, and any other interlayers. The reason why all the contributions appear in the IR jump (if the time axis is on the order of the relaxation times of the compositional variation) is due to the much quicker relaxation times; meaning $R_{Bulk}C_{Bulk}$ or $R_{SEI}C_{SEI}$ when compared to the build-up of the concentration polarization (see below).

Nonetheless, the SEI layer may grow during the polarization process. Therefore, we have to distinguish between $R_{SEI,0}$ (the resistance at the beginning of the galvanostatic polarization) and $R_{SEI,\infty}$ (the value at the steady state). For the galvanostatic polarization with the constant current (I), the initial total resistance ($R_{tot,0}$) can be described using:

$$R_{tot,0} = R_{SEI,0} + R = \frac{U_0}{I} \quad \text{Equation 4-12}$$

In the steady state the resistance can be defined as ($R_{tot,\infty}$),

$$R_{tot,\infty} = R_{SEI,\infty} + R_+ = \frac{U_\infty}{I} \quad \text{Equation 4-13}$$

with U_∞ being voltage at the steady state.

The change in resistances is observed by impedance spectroscopy before polarization and after the steady state has been reached, Figure 4-2 (Right). It is essential to avoid a lower frequency range (yellow and red) in the initial AC measurements, preventing the early polarization of the sample.

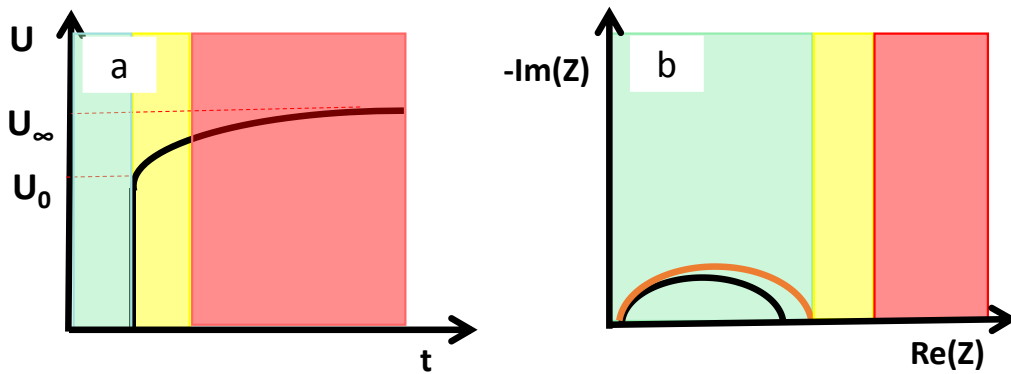


Figure 4-2a) Schematic galvanostatic polarization profile b) Schematic impedance spectroscopy before and after galvanostatic polarization. The colours represent different time regimes.

Combining Equation 4-11, 12 and 12, t_+ can be rewritten as:

$$t_+ = \frac{I(R_{tot,0} - R_{SEI,0})}{U_\infty - IR_{SEI,\infty}} \quad \text{Equation 4-14}$$

The time behaviour of voltage changes in the galvanostatic polarization exhibits an exponential behaviour for long times ($t > \tau^\delta$) [101]:

$$\ln(U(t) - U(\infty)) = \text{Const} \pm t/\tau^\delta \quad \text{Equation 4-15}$$

with τ^δ being the time constant.

For short polarization times the voltage change follows a \sqrt{t} law [101]:

$$U(t) = \text{Const} \pm \gamma^* \frac{4}{\pi^{3/2}} \sqrt{\frac{t}{\tau^*}} \quad \text{Equation 4-16}$$

The parameter γ^* is given by:

$$\gamma^* = U(\infty) - \frac{i_p L}{\sigma} \quad \text{Equation 4-17}$$

where i_p is the polarization current density and $L = d_{Bulk}$ represents the thickness (electrode distances).

This enables us to calculate the salt diffusion coefficient according:

$$D^* = \frac{l^2}{\tau^* \pi^2} \quad \text{Equation 4-18}$$

4.1.5 Stripping-Plating Experiments

Repeated galvanostatic polarization and depolarization of a symmetric lithium cell with reversible electrode provides the means to explore the cyclability of the cell. In this method, the lithium is being stripped from one electrode and plated on the other electrode for a specific time interval, followed by the same procedure in the other direction. The corresponding voltage response to the constant applied current value is recorded as a function of time. Any cell failure as a result of short circuit can be seen in a sudden voltage drop.

Herein, AAO:(LiTf/triglyme) electrolytes have been explored employing lithium electrodes, with a cyclic lithium plating-stripping procedure consisting of one-hour charging followed by one-hour discharging [102].

4.2 Results and Discussion

4.2.1 Characterization of the AAO

The AAO sample has been characterized in terms of its nature and structure of nanopores. Shape, size and orientation of pores in AAO membrane can be observed from the SEM micrographs shown in Figure 4-3. The pores appear to have conical frustum form with one base average diameter being 40 nm and the other base diameter being 200 nm.

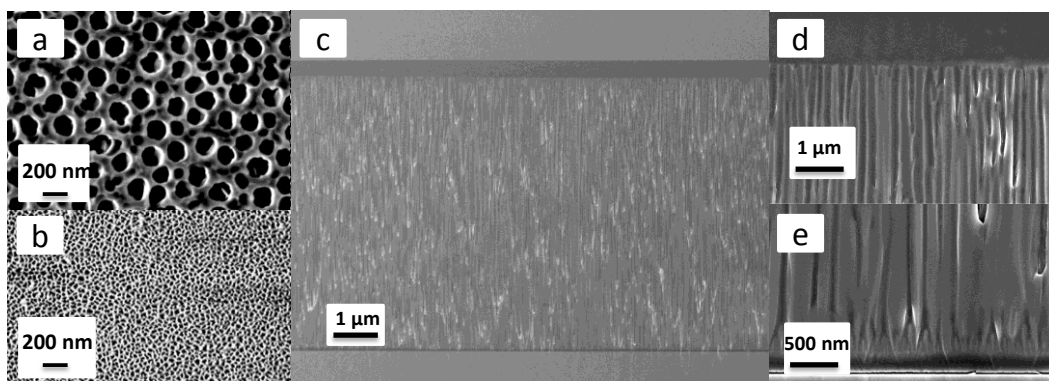


Figure 4-3 Characterization of the AAO membranes: a,b) scanning electron micrographs(top view) of 2 sides of the membrane. c) cross-section of the pores d,e) the cross section of the AAO sides corresponding to a and b.

A rough value of $35 \text{ m}^2 \text{ g}^{-1}$ is calculated for the surface area, considering the geometry and approximate number of pores from the SEM micrographs. The surface area measurement using nitrogen adsorption and Brunauer-Emmett-Teller (BET) analysis yields a similar surface area of $24 \text{ m}^2 \text{ g}^{-1}$. The XRD results indicates that the AAO is amorphous, as no peaks can be detected (appendix A Figure 4). In ^1H MAS-NMR spectra of the amorphous samples, a broad peak around 5 ppm is observed, as shown in Figure 4-4. The spectrum can be fitted by three Gaussian components. The peak at 5.88 ppm is assigned to physically adsorbed water, while peaks at 3.53 and 1.33 ppm are assigned to the proton in -OH groups bound to aluminium. Indeed, it has been shown that amorphous alumina is composed of octahedrally and tetrahedrally coordinated

Al^{3+} , explaining the appearance of two types of hydroxyl groups in NMR spectra based on how $-\text{OH}$ is coordinated to Al atoms [103].

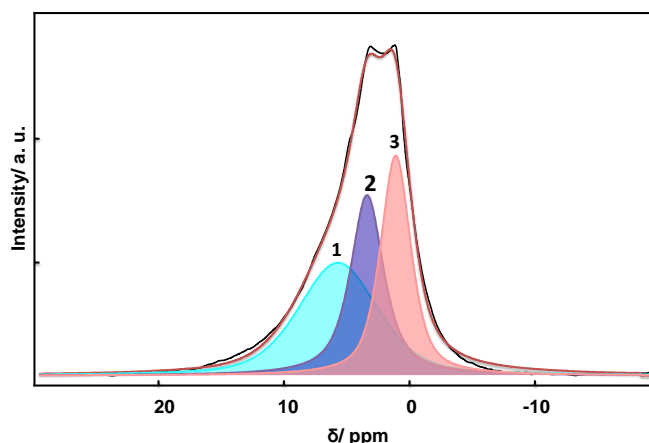


Figure 4-4 ^1H MAS-NMR spectra of a crushed AAO membrane (black line) was fitted with three Gaussian component (blue, purple and orange line) to estimate the total number of available surface $-\text{OH}$ groups.

Taking into account the total number of $-\text{OH}$ groups measured w NMR and the estimated surface area, the density of the $-\text{OH}$ groups is calculated to be 6.5 nm^{-2} . This number corresponds to all the $-\text{OH}$ groups available in bulk and on the surface. However, the relevant number is the percentage of these $-\text{OH}$ groups allocated on the surface, and how many of these surface groups are indeed active.

The activity of $-\text{OH}$ groups has been corroborated using ion exchange capacity experiment for ball-milled AAO (1h), giving values of $7.16 \times 10^{-2} \text{ mmolg}^{-1}$ which is an order of magnitude lower value than reported for porous SiO_2 particles in the similar solvent [11].

4.2.2 Electrochemical Properties of AAO: (1 M LiTf/triglyme)

The effective surface Zeta potential (ζ_{eff}) for 1 vol% of crushed AAO particles dispersed in 1M LiTf/triglyme electrolyte is negative ($\zeta_{\text{eff}} = -28 \text{ mV}$), indicating interfacial effects through Tf^- adsorption. Nevertheless, ζ_{eff} values are relatively smaller in comparison to SiO_2 , disclosing a weaker interfacial adsorption which is in line with the lower IEC.

The thermal properties of the solid-liquid electrolyte have been studied using DSC measurement. The DSC thermogram indicates that 1M LiTf/triglyme crystallizes around -70°C and starts to melt at -50°C . The melting temperature slightly increases (5°C) for AAO: (1M LiTf/triglyme), while crystallization temperature decreases to the lower temperatures, suggesting fairly similar thermal properties (appendix A Figure 5).

The lithium transference number was measured using the galvanostatic polarization method explained in chapter 4.1.4. In this galvanostatic polarization, the voltage reaches steady state quite fast after just 200s, partly due to the rather thin electrolyte. The lithium transference number using Equation 4-14 for AAO: (1 M LiTf/triglyme) results in enhanced value of $t_{\text{Li}} = 0.46 \pm 0.02$ in comparison to measured value of $t_{\text{Li}} = 0.15$ for 1 M LiTf/triglyme (appendix A Figure 6). This enhanced value is expected according to anion adsorption as signified by the zeta potential.

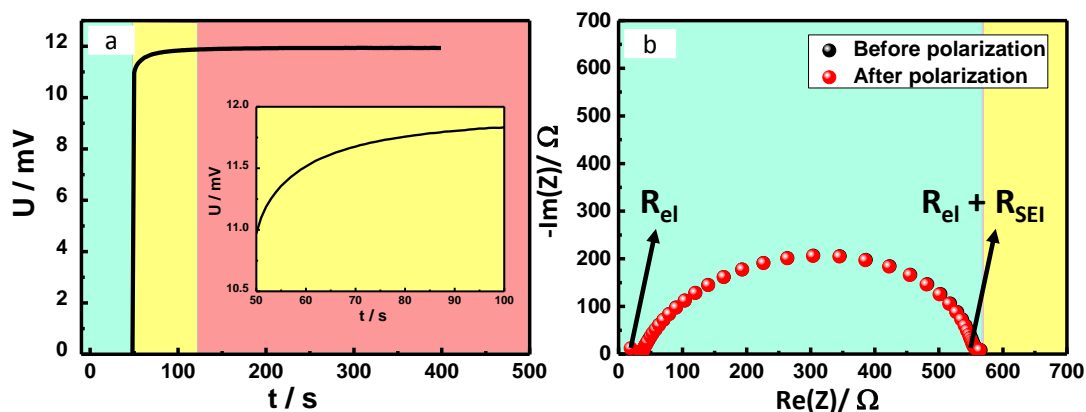


Figure 4-5 a) Time dependent galvanostatic polarization of AAO: (1 M LiTf/triglyme) in an anion blocking Li| electrolyte |Li cell with current of $0.176 \mu\text{A}$, b) impedance spectra recorded before (black) and after (red) the galvanostatic polarization. Different colours correspond to different time regimes.

Figure 4-5b illustrates the impedance spectra before and after the galvanostatic polarization. The observed semicircle corresponds to the SEI formed on the lithium electrode in contact with the electrolyte and appears to be stable during the polarization process ($R_{\text{SEI},0} = R_{\text{SEI},\infty} = 500 \Omega$). This is reassured by fitting the capacitances and deriving the corresponding thicknesses. The approximate thickness around 10 nm is calculated considering the dielectric constant of 7.5. The calculated room temperature

ionic conductivity of the electrolyte using the sample geometry and resistance (R_{el}) from impedance measurement yields value of $\sigma_m = 0.3 \text{ mS cm}^{-1}$, slightly lower than that of the corresponding liquid electrolyte $\sigma_\infty = 1 \text{ mS cm}^{-1}$. This conductivity depression will be discussed in the next part (4.2.3) in details.

As expected the voltage-time curve exhibits an exponential behaviour for longer times ($\tau > \tau^\delta$), enabling us to calculate the LiTf diffusion coefficient ($D^\delta = \frac{l^2}{\tau^\delta \pi^2}$), as shown in Figure 4-6. The time constant is determined from the slope of the linear fit (red line) of the $\ln |U - U_{ss}|$ vs. time. The calculated $D^\delta = 4 \times 10^{-8} \text{ cm}^2 \text{ s}^{-1}$ is in good agreement for the values previously reported for this salt [12].

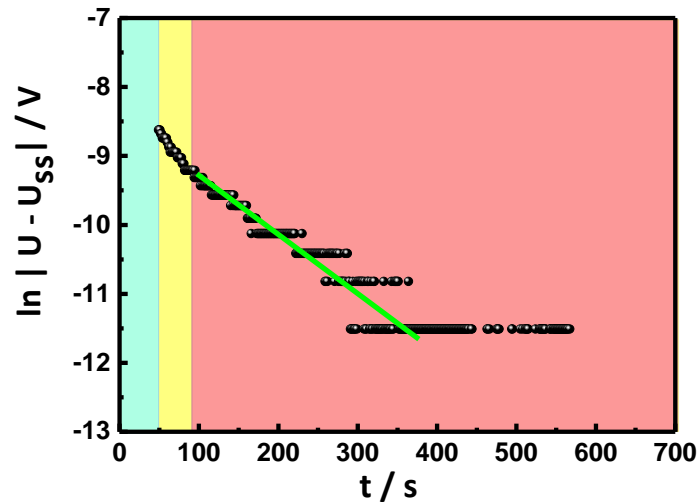


Figure 4-6 Exponential behaviour of voltage as a function of time. Extraction of the salt diffusion coefficient from the long polarization times.

It is not feasible to calculate the salt diffusion coefficient for the very short polarization time, where the voltage changes follows \sqrt{t} law, as the polarization is quite fast here.

This diffusion coefficient includes the ambipolar motion of cation and anion force by electro-neutrality and the ion pair itself and is composed of chemical resistance ($\propto 1/\sigma^\delta$) and chemical capacitance ($\propto dc_s/d\mu_s$) [104]:

$$D^\delta = \frac{1}{F^2} \left(s + \frac{\sigma_+ \sigma_-}{\sigma} \right) \frac{d\mu_s}{dc_s} \quad \text{Equation 4-19}$$

where F is Faraday constant and s is corresponding to the transport parameter of the ion pairs.

The controlled porous structure of AAO makes the galvanostatic polarization experiment fairly reproducible providing the opportunity to investigate the influence of other parameters on the lithium transference number in solid-liquid composite electrolyte including temperature and salt concentration. This investigation will be discussed in the following sections.

4.2.3 Influence of Salt Concentration on Electrochemical Properties of AAO: (LiTf/triglyme)

The influence of salt concentration on ionic conductivity and lithium transference number in the AAO: 0.02-1 M LiTf/triglyme has been elucidated. Figure 4-7 shows the polarization and AC measurements for the two extreme cases of 0.02 M and 1 M LiTf. The data for the other concentrations can be found in appendix A Figure 9.

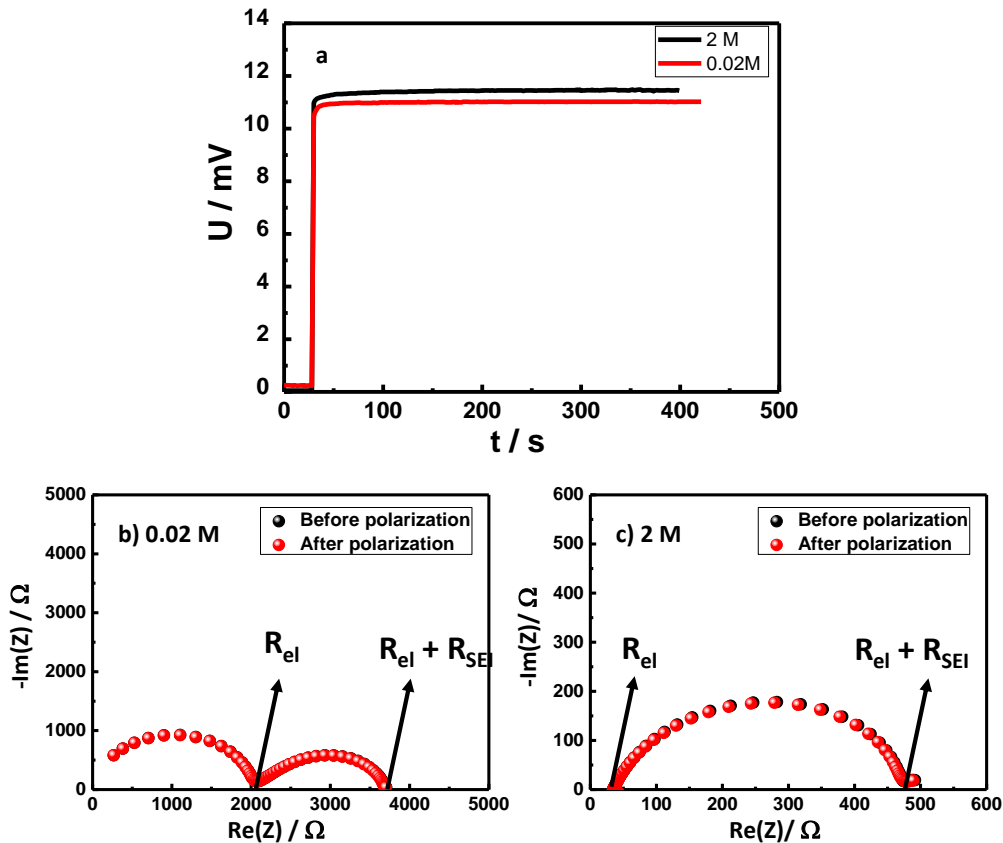


Figure 4-7 a) Galvanostatic polarization for 0.02 and 2 M LiTf/triglyme: AAO in symmetric Li/electrolyte/Li cell b) AC measurement before and after polarization for 2 M LiTf c) AC measurement before and after polarization for 0.02 M

The impedance spectra of 0.02M consists of two semicircles corresponding to the bulk of the electrolyte (higher frequency) and to the SEI (lower frequency) according to the fitted capacitances. For 0.02M, the SEI resistance is larger than for 1M, however the voltage response is lower indicating that there the polarization is very small(high t_{Li}). The effect of concentration on the SEI will be discussed in more detail in Chapter 5. Here, Figure 4-8 shows salt concentration dependent ionic conductivities and lithium transference numbers for AAO: (0.02-1 M LiTf/triglyme)

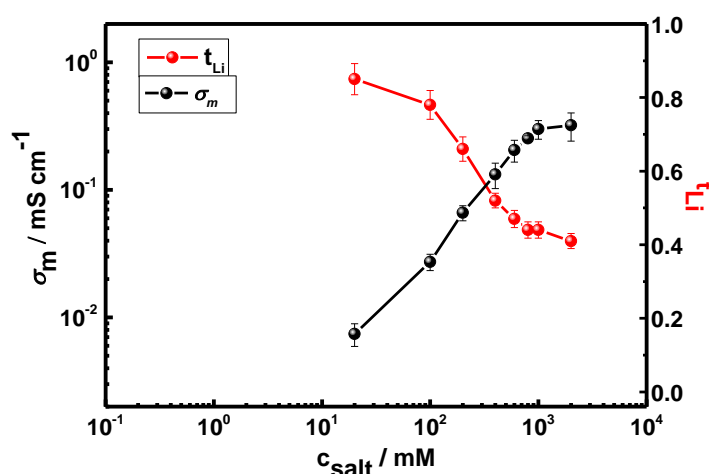


Figure 4-8 Effects of lithium salt concentration variation in AAO: (LiTf/triglyme) electrolyte on: ionic conductivity (black) and lithium transference number (red) measured by galvanostatic polarization.

A sharp rise of about 2 order of magnitude in ionic conductivity upon increasing the concentration from 0.02 M to 0.4 M is observed. The ionic conductivity eventually reaches a plateau. The lithium transference number on the other hand shows a significant decrease with the addition of salt from 0.02 to 0.4M and the trend continues with a lower rate between 0.4-2M LiTf.

To interpret the adsorption and interfacial effect in the present system, two extreme cases of the strong and weak adsorption shall be considered.

In the case of strong adsorption any surface site adsorbs an anion. Taking into account the volume fraction of the AAO (0.24) and number of -OH groups on the surface, at salt concentrations smaller than 0.47M the bulk will be completely exhausted of all ionic species (appendix A Figure 10). As a consequence, the bulk conductivity will entirely disappear as shown in Figure 4-9.

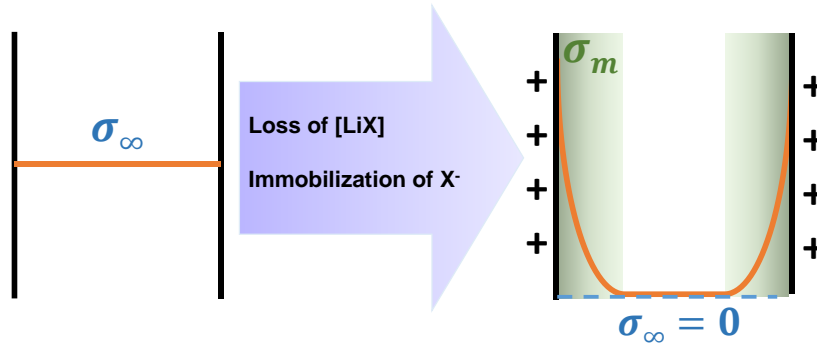


Figure 4-9 Schematic of purely bulk conduction (left) and conduction in strong adsorption case (right).

Here, the conductivity of the composite (σ_m) is given by the lithium ion conductivity in the space charge zones. As all the lithium ions of the salt find themselves as free ions in the space charge zones, we have:

$$\sigma_m = (1 - \varphi)(c_{salt} u_{Li^+}) \quad \text{Equation 4-20}$$

Here we assume the lithium ion mobility in bulk and the space charge zones is the same and the AAO content leads to the reduction according to the volume fraction (φ).

On the other hand, the conductivity of the bulk without interfacial effect can be written:

$$\sigma_\infty = c_{Li^+} (u_{Li^+} + u_{X^-}) \quad \text{Equation 4-21}$$

The conductivity of composite at $c_{salt} \approx 1\text{M}$ can hence be calculated as (details in appendix A Equation 7-9):

$$\frac{\sigma_m}{\sigma_\infty} = \frac{(1-\varphi)c_{salt} u_+}{(c_{salt}/5)(u_+ + u_-)} \approx 0.15 \quad \text{Equation 4-22}$$

In the case of strong adsorption and sufficiently high volume fraction of AAO, $\sigma_- \approx 0$ and:

$$t_+ = \frac{\sigma_+}{\sigma_+ + \sigma_-} \approx 1 \quad \text{Equation 4-23}$$

follows.

The depression in conductivity for the 0.2M is calculated to be smaller (50%) due to the fact that the increase in mobility of cation is higher than that of anion in diluted regime (appendix A Equation 9-11) [79]:

The other extreme case is the case of weak adsorption. Here, we assume the space charge effects to be negligible. Then the conductivity of the composite is given by:

$$\sigma_m = (1 - \varphi)\sigma_\infty \quad \text{Equation 4-24}$$

and a depression by 24% of the bulk value is expected ($\varphi=0.24$).

Here, the transference number remains identical to the liquid system. Likewise, the slope of the concentration dependent conductivity for the composite is analogous to the liquid system due to similar association and mobilities.

Figure 4-10a, shows the effect of salt concentration on the ionic conductivity of the liquid and composite in $c_{salt} = 0.001$ to 1M in the present study, where the slope of the composite is fairly analogous to the liquid glyme electrolyte system.

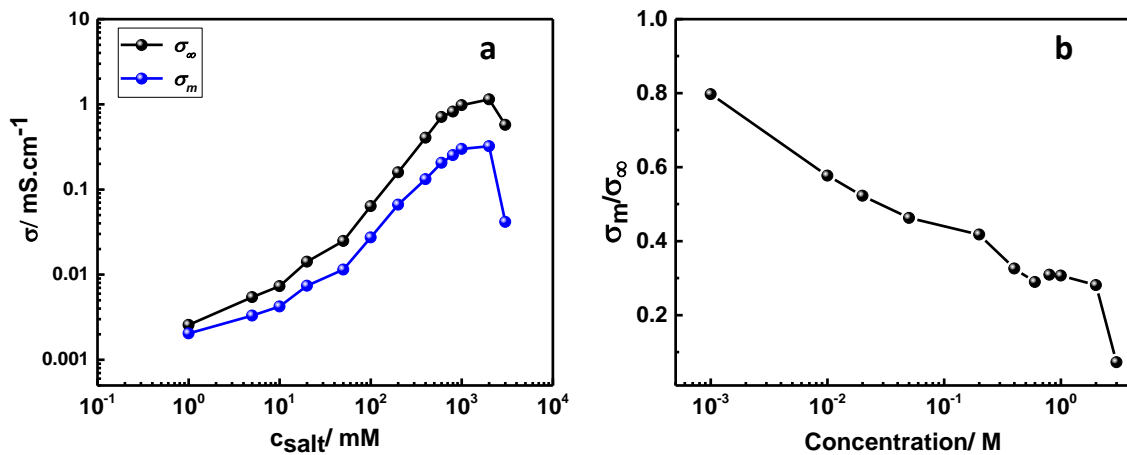


Figure 4-10 a) concentration dependent conductivity for LiTf/triglyme (black) and AAO: (LiTf/triglyme) (blue) and b) depression in σ_m for different salt concentration.

In fact all the measured results lie in between the two extremes. A depression by 70 % in the conductivity at 1M is measured which increases upon increasing the salt concentration, corroborating the discussed effect in strong adsorption.

The lithium transference number shows a substantial enhancement in the low concentration range as well, but not as much as expected for strong adsorption.

At the first glance the plateau measured around $c_{salt} = 0.5$ M in conductivity-concentration plot of composite electrolyte (blue line), seems to be caused by the total exhaustion of the salt. However, the comparable slope to the liquid system suggests that this could originate from the viscosity (appendix A Figure 11) and hence mobility effect.

In summary, the studied system here appears to meet some criteria from both cases (Table 4-1), indicating the medium level of adsorption.

Table 4-1 The characteristic of the presented system in comparison to strong and weak adsorption.

Electrochemical properties	Strong Adsorption	Weak adsorption
$\frac{\sigma_m}{\sigma_\infty}$	15%: dilute regime 50%: concentrated regime	76%: dilute and concentrated regime
Exhaustion	0.47 M	-
t_+	100%	15%
Slope of (Log(σ) vs. Log(c_{salt}))	1	Similar to liquid

4.2.4 Influence of Temperature on Electrochemical Properties of AAO: (1 M LiTf/triglyme)

Temperature controlled galvanostatic polarization has been implemented in the range of 10 to 80 °C for the AAO: (1 M LiTf/triglyme). Figure 4-11 demonstrates the voltage versus time curve and impedance spectra before and after the polarization experiment for 10 and 80 °C. The polarization and impedance data for other temperatures is reported in appendix (A Figure 7).

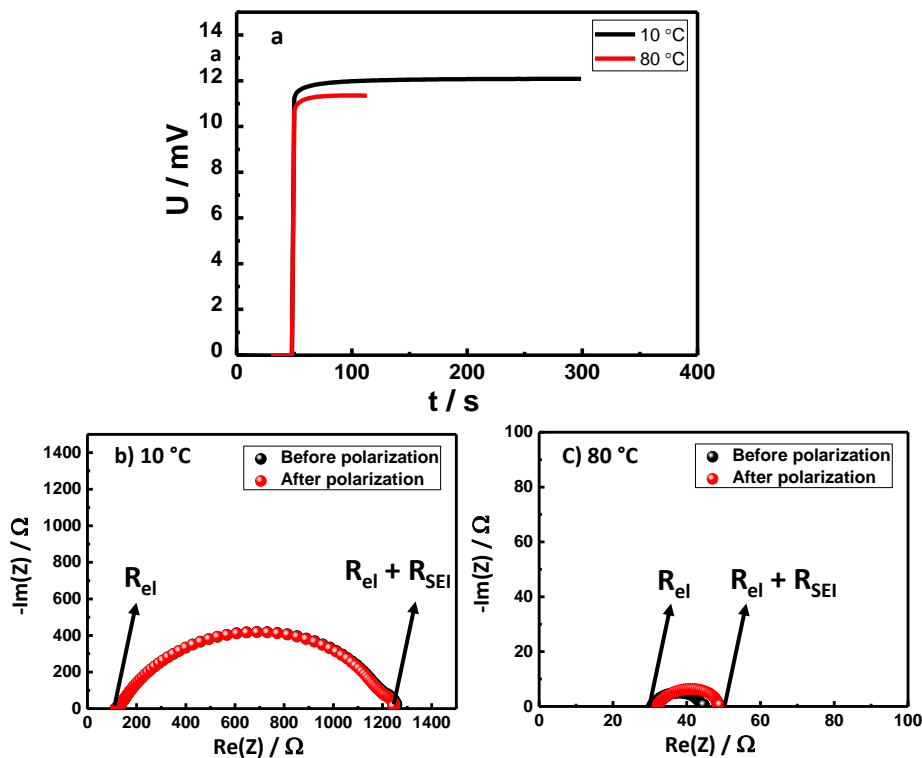


Figure 4-11. Temperature controlled galvanostatic polarization of a Li/AAO: (1 M LiTf/triglyme)/Li cell: a) voltage-time curve for 10 and 80 °C, b) AC impedance before and after polarization at 10 °C, c) AC impedance before and after polarization at 80 °C.

As it is expected and observed, the polarization occurs faster upon increasing temperature. Additionally, the resistance of the electrolyte (R_{el}) decreases slightly while

the depletion in resistance of the SEI layer (R_{SEI}) is quite significant amid increasing temperature, suggesting chemical composition or morphological changes in the passivation layer. This will be discussed in details in Chapter 5.

Figure 4-12 shows temperature-dependent ionic conductivity and lithium transference number of AAO: (1 M LiTf/triglyme) in the range from 10 to 80 °C. The AC conductivity of composite liquid/solid electrolyte enhances from 1.8 to 2.6 mS cm⁻¹ in this range. The analogous rising trend has been observed for lithium transference number to value of $t_{Li}=0.80$ at 80 °C, which could be explained by the changes in the molecular speciations and mobilities upon heating.

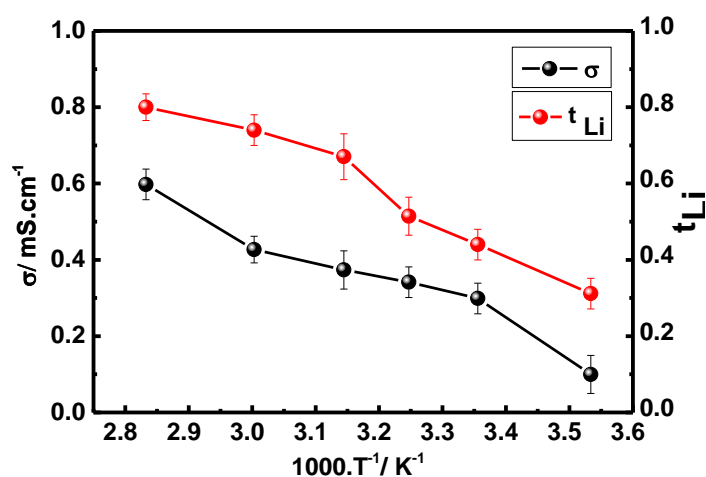


Figure 4-12 Temperature dependent ionic conductivity (black) and lithium transference number (red) in AAO: (LiTf/triglyme).

The presence of different ionic species in 1M LiTf/triglyme has been detected using temperature controlled IR spectroscopy as shown in Figure 4-13. Temperature elevation from 20 to 80 °C enhances the fraction of ion pair and dimers fraction while lowering that of the free ions, corroborating the reported association behaviour in similar system [78]. This suggests that the association reaction is counterintuitively endothermic ($\Delta H_{ass}^{\circ} > 0$). Obviously- and this is well-known in the literature- it is the strong solvation of the free ions that causes this effect. The same solvation effect also causes the necessary entropy gain for the association to occur [78]. The bare association of free ions into the ion pair is expected to have a negative entropy. However, each free

lithium ion is solvated by about 3 glyme molecules, while the contact ion pair is solvated by about one glyme molecule. This solvation contribution explains both the negative entropy and endothermicity of association.

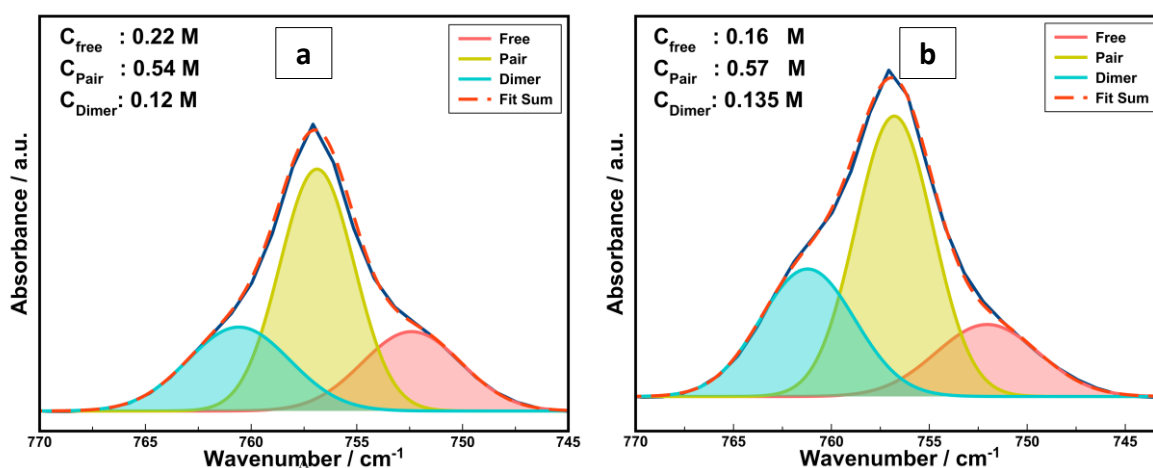


Figure 4-13 Infrared spectra of the triflate stretching band for 1 M LiTf/triglyme at a) 20 °C, b) 80 °C. Concentration of the free ions (green), ion pairs (pink) and dimers (yellow) has been determined from the Gaussian-Lorentzian fit (dashed red line) of the total measured spectra (continuous blue line).

Furthermore, the increase in conductivity from 0.3 to 0.6 mS cm⁻¹ in this temperature range accompanied with the depression in percentage of concentration of free ions from 0.22 to 0.16 M implies the increase in total mobility of about 4 times:

$$\frac{(u_+ + u_-)_{80\text{ }^\circ\text{C}}}{(u_+ + u_-)_{20\text{ }^\circ\text{C}}} = \frac{\sigma_{AC,80\text{ }^\circ\text{C}} c_{free,20\text{ }^\circ\text{C}}}{\sigma_{AC,20\text{ }^\circ\text{C}} c_{free,80\text{ }^\circ\text{C}}} \approx 4 \quad \text{Equation 4-25}$$

This is indeed corroborating to recorded temperature dependent viscosity measurement, Figure 4-14, indicating reduction in viscosity (4 times) upon elevating temperature.

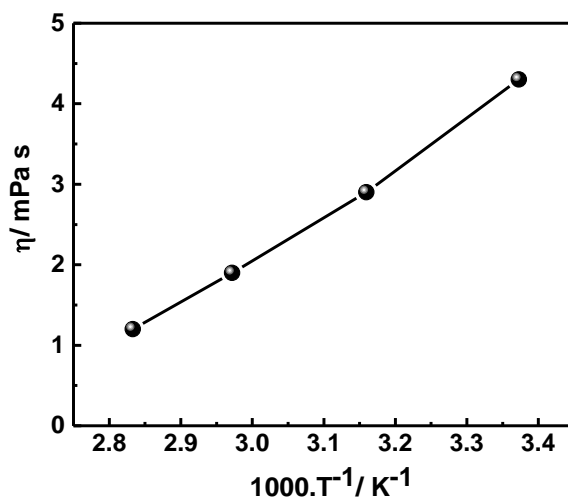


Figure 4-14 Viscosity changes upon increasing temperature in the range of 20 to 80 °C.

The temperature effect on the chemical diffusion coefficient of the salt (D^δ), which is calculated by fitting the exponential part of the DC polarization curve for different temperature (Figure 4-15) is in agreement with the mobility variation. The fits and slopes are reported in appendix (A Figure 8). D^δ increases an order of magnitude upon increasing temperature from 10 to 80° C, qualitatively comparable trend to the conductivity of the system.

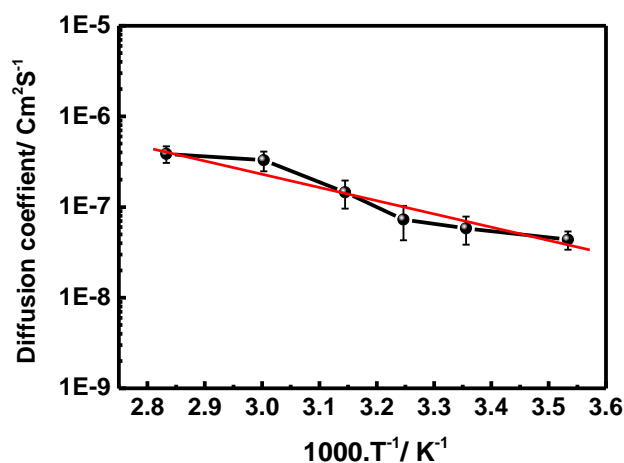


Figure 4-15 Temperature dependent diffusion coefficient determined at long galvanostatic polarization times.

4.2.5 Lithium Stripping-Plating Experiments

The cyclability of liquid/solid electrolytes with lithium electrodes is explored using stripping-plating experiments. Figure 4-16 a and b illustrates the time-dependent voltage profile in a long time procedure with subsequent one hour stripping and one hour plating under a constant current density of 0.3 mA cm^{-2} in AAO: 1M LiTf/triglyme and Whatman glass fiber separator: 1M LiTf/triglyme.

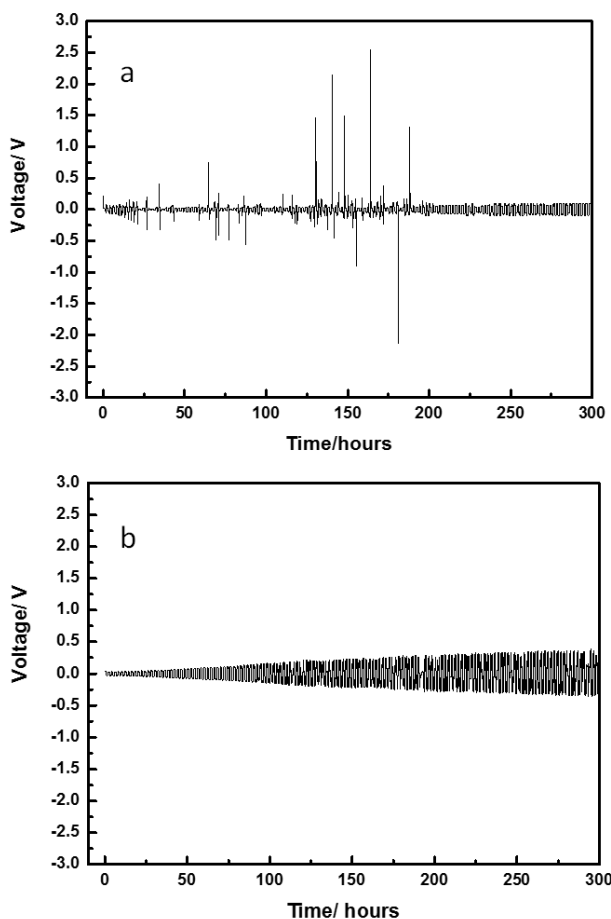


Figure 4-16. Lithium stripping-plating at 0.3 mA cm^{-2} in a symmetrical Li/electrolyte/Li cell for: a) AAO: (1 M LiTf/triglyme) b) Whatman: (1 M LiTf/triglyme).

The corresponding voltage response suggests that for the Whatman separator:(1M LiTf/triglyme) electrolyte, the steady-state value cannot be reached, and the voltage

constantly increases to values as high as 0.5 V after 300 hours, contrary to the AAO: (1M LiTf/triglyme), showing no over-potential. The cell failure in the AAO: 1M LiTf/triglyme electrolyte seems to occur later than in the AAO-free case (300h), implying that the solid-liquid electrolyte is able to partially hinder the dendrite formation and substantially enhance the lifetime of the cell. However, sudden and momentary instabilities of the voltage profile can be observed in this electrolyte (AAO-based). This is either initiated by the obstruction of the pores due to lithium deposition or salt decomposition inside the pores. Indeed, lithium deposition can be observed in SEM micrographs of AAO after 300 cycles. Growth of mossy lithium through the AAO monolith (Figure 4-17a, b) and on the lithium surface (Figure 4-17c, d) is detected by SEM after disassembling the long-cycled Li/AAO: (1M LiTf/triglyme)/Li cell under controlled atmosphere.

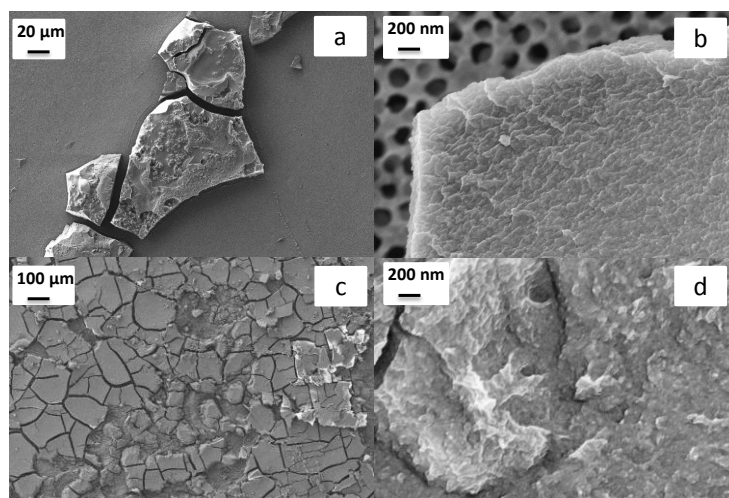


Figure 4-17 SEM images of mossy lithium formed during the stripping-plating experiment in Li|AAO: (1 M LiTf/triglyme) |Li cell: (a and b) mossy lithium on the surface of porous AAO (c and d) mossy lithium on the surface of lithium electrode.

Such mossy lithium is covered by a thin SEI layer as verified by corresponding energy-dispersive X-ray spectroscopy (EDS) elemental mapping images Appendix (A Figure 12) where C, F, and O are visibly detected. This is not surprising, since the deposited lithium is still in contact with the electrolyte and the new SEI can instantaneously form. Furthermore, the effect of salt concentration is probed as the increase in the lithium transference number suggests possible improved cyclability. Figure 4-18 shows the charge-discharge profile

versus time under constant current density of 0.3 mA cm^{-2} in AAO: (0.02 M LiTf/triglyme). However, the observed cyclability is poor in this low concentration probably due to the unstable SEI formed in this case. This will be discussed in detail in Chapter 5.

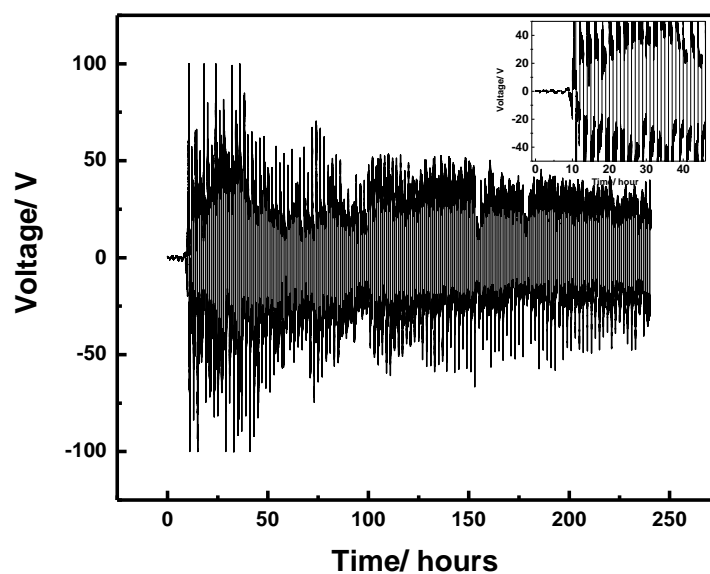


Figure 4-18 Lithium stripping-plating at 0.3 mA cm^{-2} in a symmetrical Li/electrolyte/Li cell for AAO: (0.02 M LiTf/triglyme).

4.3 Conclusions

In this chapter, the electrochemical properties of porous anodic aluminium oxide (AAO) infiltrated with LiTf/triglyme as a class of solid/liquid electrolytes is discussed. The preferential adsorption of anion on the surface of AAO is responsible for the enhancement in lithium transference number ($t_+ \approx 0.46$ for AAO: (1 M LiTf/triglyme)) linked with high ionic conductivity ($\sigma_m \approx 0.3 \text{ mS cm}^{-1}$). This enhanced lithium transference number and depression of 70% in ionic conductivity at 1M on one hand and identical concentration dependent ionic conductivity behaviour to the corresponding liquid electrolyte on the other hand suggests distinct but not exhaustive adsorption of anions.

The effect of temperature and salt concentration on the interfacial effects and electrochemical behaviour of this class of electrolyte have been investigated in detail. The lithium transference number increases upon increasing temperature and decreasing salt concentration, with t_{Li} reaching values of 80% at 80 °C in 1 M LiTf/triglyme and 85% at 25 °C in 0.02 M LiTf/triglyme.

Additionally, lithium dendrite growth is probed by galvanostatic stripping-plating in the Li| AAO: (1 M LiTf/triglyme) |Li symmetric cell, showing the ability of this kind of electrolyte in hindering the dendrite compared to its liquid counterpart infiltrated in glass fiber separator.

Chapter 5 SEI on Lithium Electrode in Contact with Glyme Electrolyte

5.1 Experimental

5.1.1 Materials

Lithium 4,5-dicyano-2-(trifluoromethyl)imidazole (LiTDI): Niedzicki et al. have developed this lithium salt, shown in Figure 5-1 [105, 106].

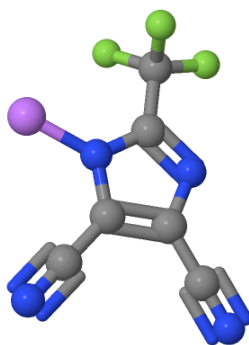


Figure 5-1 Molecular structure of LiTDI.

It has been reported that the 0.3 M LiTDI salt offers a conductivity of 5 mS cm^{-1} in EC:DMC comparable values to conductivity of salts such as LiPF_6 in EC:DMC(1:2) [107, 108]. This quite high ionic conductivity at even low concentration accompanied with relatively high lithium transference number ≈ 0.5 makes this salt a favourable candidate for conventional electrolytes [108]. It has been shown that this salt provides a thermal stability at temperatures over 200°C and electrochemical stability in liquid and solid polymer solvents up to $+4.6 \text{ V}$ vs. metallic lithium anode and Al

collectors, which makes it a proper choice for lithium-based batteries [106].

Chlorotrimethylsilane: Chlorosilanes are organosilicon compounds that have been used for surface modification of lithium metal to prevent formation and growth of the SEI layer [67, 109]. Chlorotrimethylsilane shown in Figure 5-2, with the formula $(\text{CH}_3)_3\text{SiCl}$, has been investigated.

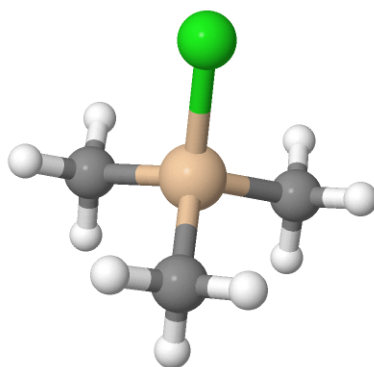


Figure 5-2 Molecular structure of chlorotrimethylsilane.

It has been suggested that the chlorosilanes derivatives are able to react with lithium hydroxide or lithium oxide existing in native film on the lithium metal surface to form LiCl and lithium alkyl silanolate or siloxanes [67].

5.1.2 X-ray Photoelectron Spectroscopy (XPS)

XPS is a spectroscopic method for chemical analysis of the material surface composition. The principle of this technique is the photoelectric effect, which is due to emission of electrons when the material is excited by photons. This effect can be described by the Einstein's photoelectric law based on the energy conservation equation [110]:

$$E_{\text{Binding}} = h\nu - E_{\text{Kinetic}} - \phi \quad \text{Equation 5-1}$$

where E_{Kinetic} is the kinetic energy of the electron expelled from the material by

irradiation of the photon with energy $h\nu$ and $E_{Binding}$ is the binding energy of the electron in the material, ϕ is the work function which depends on the setup and material i.e. an instrumental factor.

In an XPS setup, the material surface is irradiated by X-rays with sufficient energy resulting in core level electrons to be excited as illustrated in Figure 5-3 (left). The emitted photoelectron has a specific kinetic energy depending on the X-ray photon energy that can be measured using an appropriate electron energy analyser. In the relaxation process of the excited ion, shown in Figure 5-3 (right), the higher-level electron falls and fills the core hole. The energy transfer to a higher level cause the emission of an Auger electron through an internal transition, which is independent of the X-ray photon energy. Since the ejected electrons in the spectral peaks have a very short inelastic mean free path and only can travel few nano-meters, the method is suitable for surface analysis and has been implemented in the investigation of thin passivation layers such as SEI [111-115].

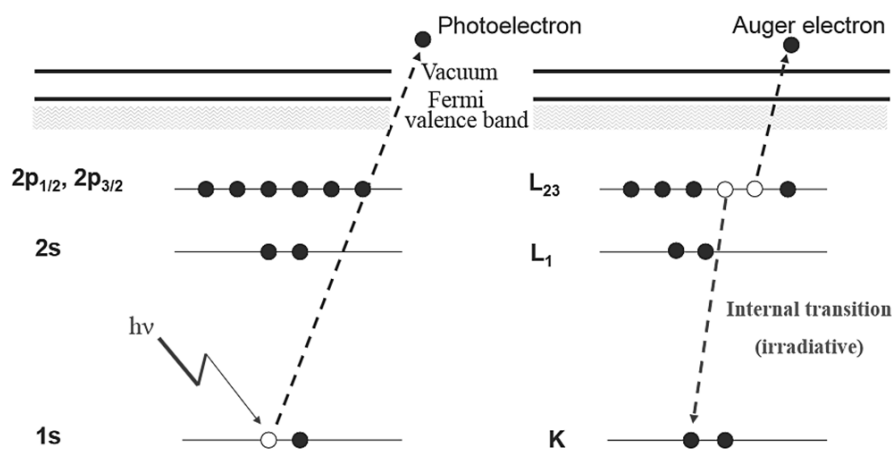


Figure 5-3 The photoemission process involved in the XPS surface analysis. The dots represent electrons and the bars represent energy levels within the atom [110].

The XPS mainly consists of an X-ray source, sample chamber and an electron analyser. The probe analysis is conducted in a vacuum chamber, under the best vacuum conditions achievable. This is to minimize the electron scattering, as XPS is very surface-sensitive, with a typical sampling depth of only a few nanometers. Additionally,

monoatomic depth profiling in XPS gives the possibility to etch layers of the surface or surface contamination using an ion beam in order to reveal the information about inner layers. The ion sputtering could provide insight into the thickness of the surface layer as well.

The XPS has been performed in the interfacial analytics group at Max Planck Institute for Solid State Research with Dr. Kathrin Müller and Prof. Ulrich Starke.

5.1.3 **Electrochemical Measurement**

The typical Li|AAO: (LiTf or LiTDI/triglyme)| Li cell described in chapter 4 are assembled in the glove box. The galvanostatic measurement is performed at different temperatures ranging from 20 to 80°C and for various salt concentrations in the range of 0.02-1M using Keithley 2604. The EIS spectra is recorded (Solatron 1260) before and after the polarization in the range of 10^{-1} to 10^7 Hz. After disassembling the cell, lithium metal electrodes are transferred from the glove box to the XPS chamber or the FIB-SEM setup using an airtight self-designed cells.

5.1.4 **Surface Modification:**

To form an artificial SEI on lithium metal, chlortrimethylsilane (Aldrich, $\geq 99\%$) is employed. Two punched lithium electrodes ($d=9$ mm) are immersed in 20 mL chlortrimethylsilane for 5 minutes. Dried electrodes are subsequently assembled in symmetric Li| AAO: (1M LiTf/triglyme) | Li. The typical galvanostatic polarization and impedance spectroscopy before and after polarization are recorded.

5.2 Results and Discussion

5.2.1 Chemical Composition and Morphology of the SEI on lithium

As it has been already mentioned in the chapter 3.3, the formation of a native surface film on lithium metal regardless of the storage and experimental conditions is inevitable for practical systems. In order to be able to assign the SEI spectra precisely, lithium metal as received and preserved in an Ar glovebox environment is probed by XPS. The surface analysis of the pristine lithium, Figure 5-4 a-i includes C 1s, O 1s and Li 1s signals.

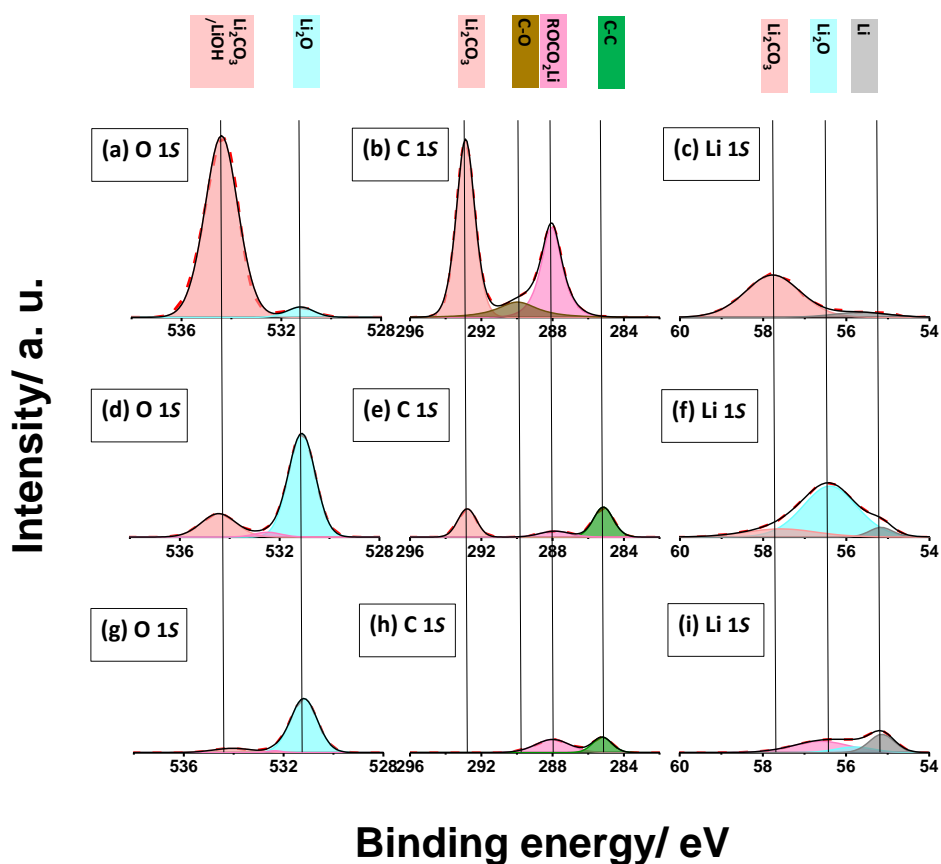


Figure 5-4 Detailed XPS spectra of pristine lithium: O 1s, C 1s and Li 1s. a-c) on the surface, d-f) after 5 minutes of Ar⁺ sputtering, g-i) after 60 minutes of Ar⁺ sputtering.

The surface contamination does not reveal any fluorine or sulphur species. The O 1s spectra can be deconvoluted in two different spectral signals assigned to the Li₂CO₃

(534.4 eV) and Li_2O (531.2 eV). The C 1s signal can be described by three components: Li_2CO_3 (292.9 eV) followed by a very weak signal corresponding to C-O band (290 eV) appearing probably due to existence of ether impurities during the XPS cell assembling in the glovebox, and the semi-carbonate such as ROCO_2Li (288 eV). The Li 1s signal reveals the same species previously mentioned, including Li_2CO_3 (57.8 eV), Li_2O (56.2 eV) and metallic Li (55.2 eV).

The XPS spectra of lithium metal after 5 and 60 minutes of Ar^+ ion sputtering (Figure 5-4 d-i) suggest that the carbonate and semi-carbonates are located on the surface (≈ 2 nm), while Li_2O exists in a deeper layer. The presence of Li_2O is detected even after 60 minutes of Ar^+ sputtering ($\approx 120\text{nm}$), in the material bulk. Nonetheless, the signal of the pure Li metal can be observed even at the surface. Furthermore, the FIB-SEM images of the same sample, Figure 5-5 a and b show the dense initial layer following by lithium accompanied by partial impurities. The SEM image of lithium metal (Figure 5-5 C) indicates that the impurities are mostly decorate lithium metal grain boundaries. Considering the XPS data and SEM-FIB images, a structural sketch of lithium metal is proposed in Figure 5-5 d.

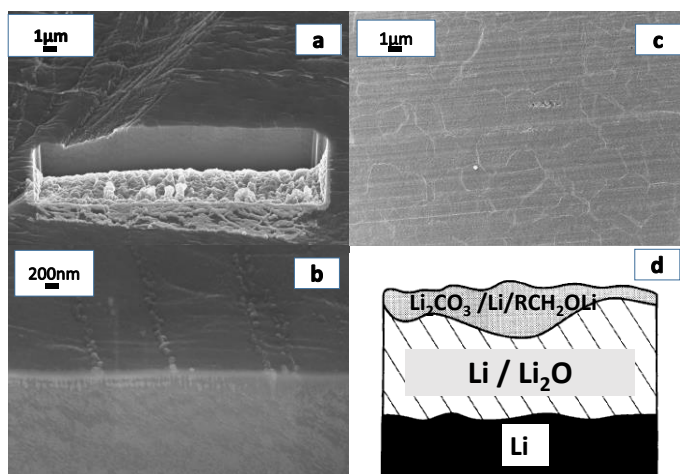


Figure 5-5 FIB-SEM images of lithium: a and b) cross section morphology of the lithium metal depicting the native passivation film. b) SEM image of the lithium showing the precipitated impurities on the grain boundaries. d) structural sketch of native passivating layer on lithium.

Subsequently, the lithium metal is chemically passivated by immersion in the 1 M LiTf/triglyme electrolyte. Figure 5-6 represents the detailed XPS spectra of F 1s, O 1s, C 1s and S 2p on the surface(a-d) and after 1(f-i) and 60 (k-n) minutes of Ar⁺ sputtering for the immersed sample.

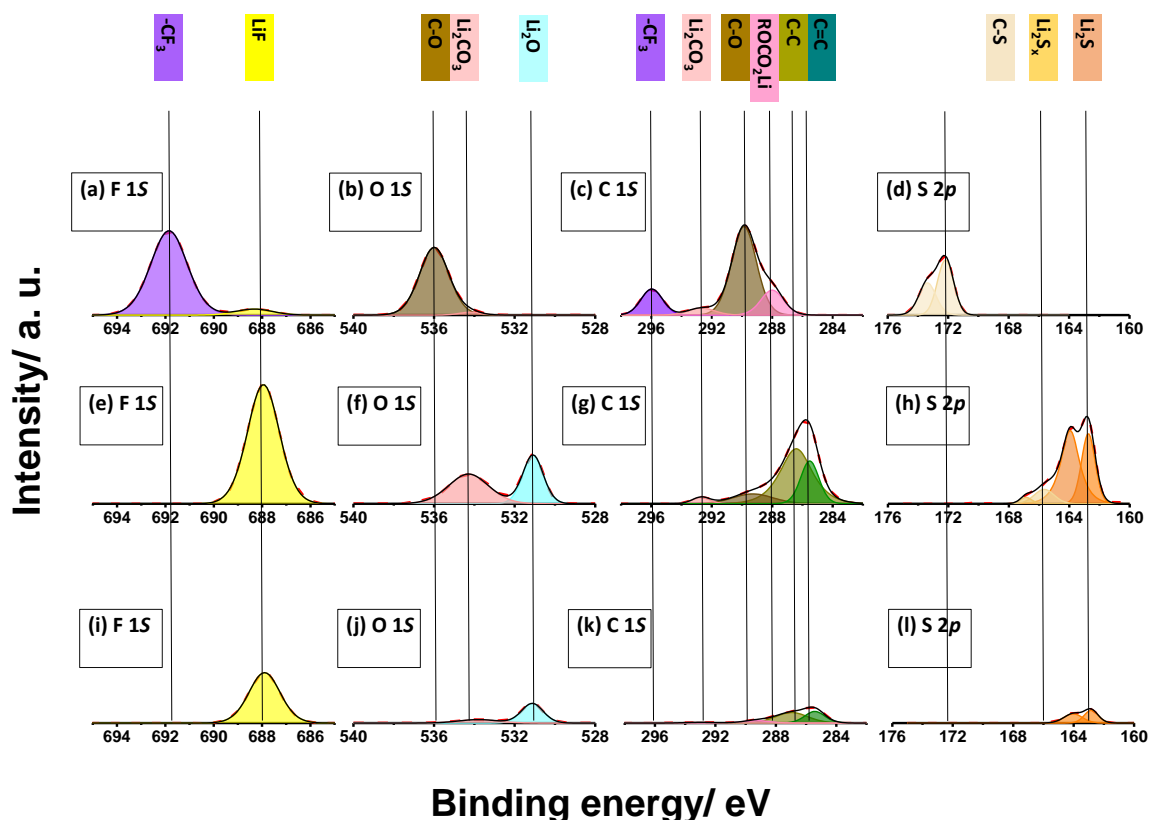


Figure 5-6 Detailed XPS spectra for lithium immersed in 1M LiTf/triglyme: F 1s, O 1s, C 1s and s 2p. a-d) on the surface, e-h) after 1 minute of sputtering, i-l) after 60 minutes of sputtering.

The signals can be assigned to species that are well-known to form in the SEI on metallic lithium anodes in contact with salt containing aprotic solvents, Appendix(A Table 1). The F 1s signal on the surface is composed of two components, LiF contribution at 688 eV and the ($-\text{CF}_3$) band of LiTf at 691.9 eV. The latter one disappears after 1 minute of Ar⁺ sputtering while the LiF is still present in the bulk even after 60 minutes of sputtering. In addition to that, the decomposition products of LiTf have been also observed in S 2p spectra upon sputtering, corresponding to Li_2S_x (166.43 eV) and Li_2S (162.8 eV), respectively. The O 1s spectra reveals a (C–O) band of strong intensity on the surface, attributed to the triglyme solvent residual on the

surface. The signal disappears after 1 minute of sputtering, while Li_2O and Li_2CO_3 become visible in the inner layers of the SEI. The C 1s signal on the surface can be described with four components. The component with the highest binding energy corresponding to the $(-\text{CF}_3)$ group in LiTf (296 eV), followed by carbonates (293 eV). The maximum at the C 1s signal at 290 eV is referred to the $(\text{C}-\text{O})$ band due to ether-based solvent residual, since it almost vanishes after one minute of Ar^+ sputtering. The C1s signal in sputtered spectra reveals the presence of C-C (287 and 285.5 eV) which is probably due to the degradation of glyme upon sputtering.

Information on the thickness of the SEI formed on the lithium metal after immersion in the electrolyte can be derived from the Li 1s signal, Figure 5-7. The peaks corresponding to the pure lithium appear after 16 minutes of Ar^+ sputtering, suggesting the formation of the passivation layer with the thickness of less than 30 nm.

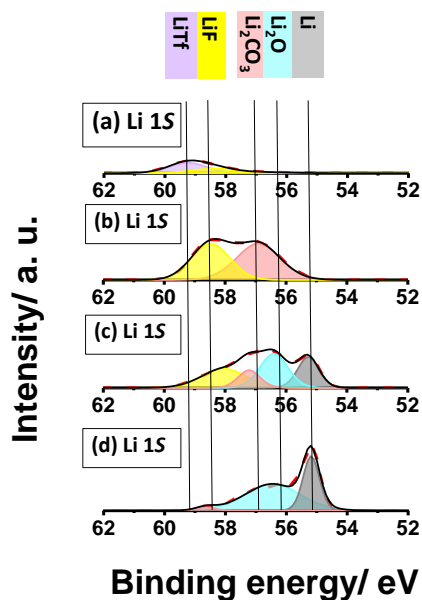


Figure 5-7 Detailed XPS spectra of Li 1s signal for the lithium electrode immersed in 1 M LiTf/triglyme electrolyte: a) on the surface b) after 1 minute of Ar^+ sputtering c) after 16 minutes of sputtering d) after 60 minutes of Ar^+ sputtering.

Furthermore, the mechanism of SEI growth under OCV conditions has been investigated. Figure 5-8 demonstrates the thickness of the SEI (L_{SEI}) as the function of square root of time (\sqrt{t}), with the presumption that resistance of the SEI (R_{SEI}) is proportional to the thickness (L_{SEI}).

At the beginning, the growth of SEI follows a linear behavior, indicating predominantly surface reaction-controlled growth mechanism given by [46]:

$$l_{short} = (s\Delta\mu_{Li})t \quad \text{Equation 5-2}$$

Here ($s\Delta\mu_{Li}$) is extracted from the slope of linear fit in $l - t$ plot, with s and μ_{Li} being the reaction constant and the chemical potential of the lithium, respectively.

On the other hand the growth behavior is square root-like with t in the longer period of time (l_{long}), suggesting a diffusion-controlled mechanism [46], where ($\sigma^\delta\Delta\mu_{Li}$) is derived from the slope of linear fit in $l - \sqrt{t}$ plot:

$$l_{long} = \sqrt{2(\sigma^\delta\Delta\mu_{Li})}t \quad \text{Equation 5-3}$$

where σ^δ is the ambipolar conductivity of Li .

If these two mechanism refer to different t-regimes of the same process, the total behavior should be describable in the form of [116]:

$$L_{SEI} = -\frac{\sigma^\delta}{s} + \sqrt{\frac{\sigma^{\delta 2}}{s^2} + 2\sigma^\delta\Delta\mu_{Li}t} \quad \text{Equation 5-4}$$

However, this equation does not fit the presented plot (Figure 5-8, red line). Indeed, the intersection point at around four hours rather suggests two independent interfacial and diffusion controlled processes as indicated by the dashed lines in Figure 5-8. The fact that the measured resistance corresponds to the lower resistance branch of each

mechanism indicates that these two are parallel and not in series.

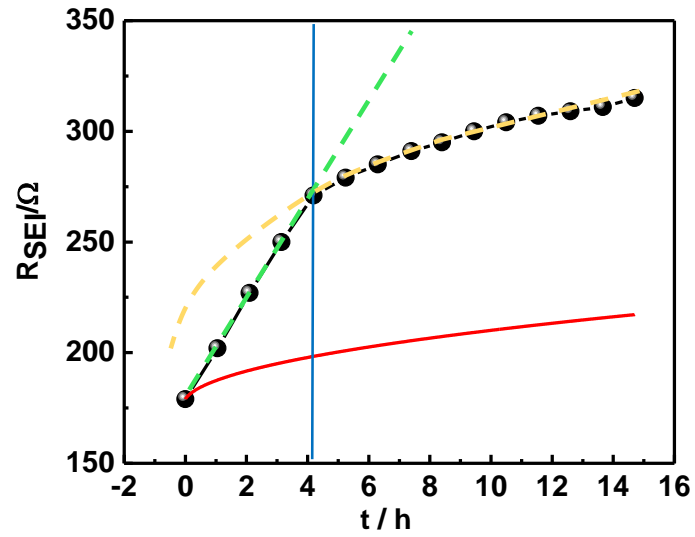


Figure 5-8 The increase in resistance of SEI upon time under OCV condition. Red line is the corresponding fit by assuming that a single process occurs. The dashed lined are obtained by extrapolation assuming two independent process.

To investigate the effect of galvanostatic polarization on the SEI composition, the XPS spectra of one-time polarized sample (1Cy) is obtained. It appears that the composition on the surface and the thickness of the passivation layer varies in comparison to the immersed sample. Figure 5-9 shows the comparison of the XPS spectra of immersed (black) and electrochemically (red) formed SEI layer on the surface compared to the spectra after 16 and 60 minutes of Ar^+ ion sputtering.

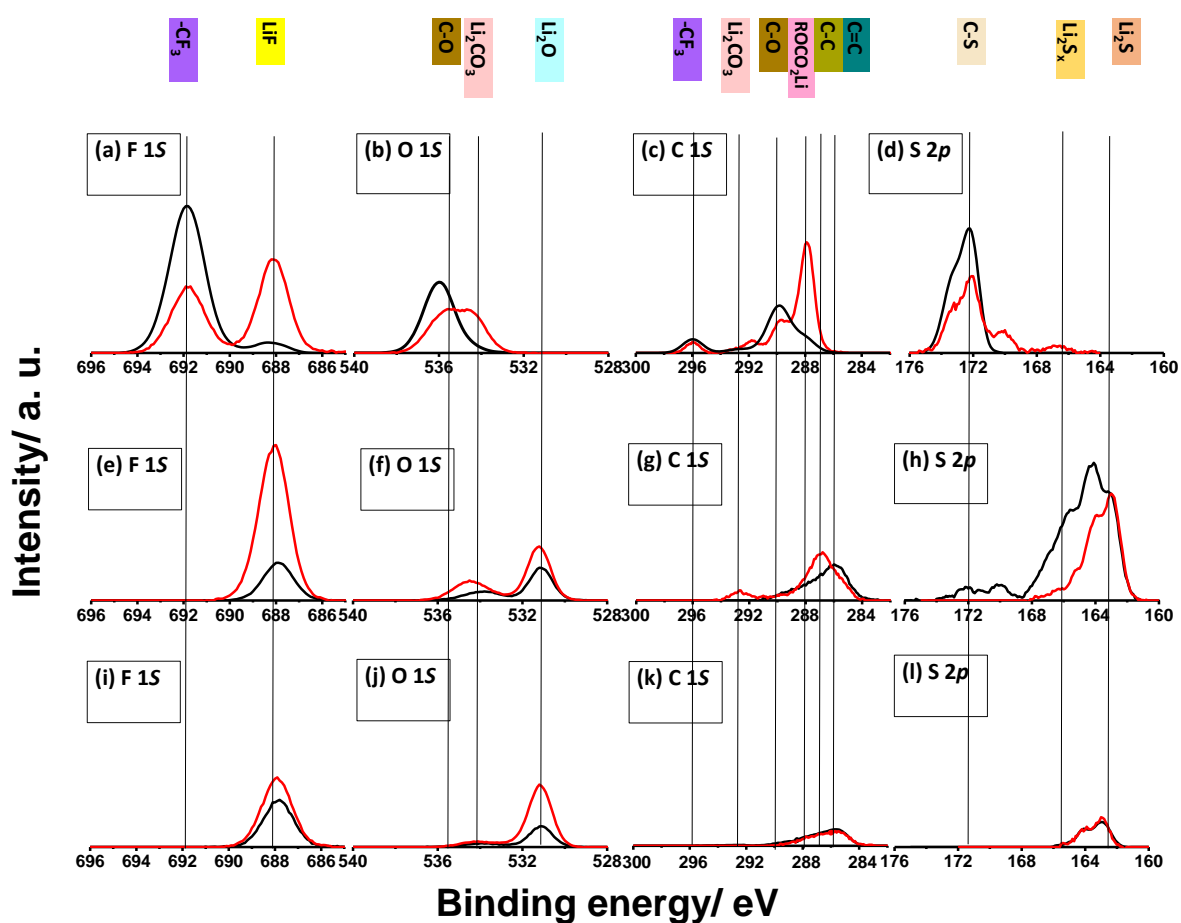


Figure 5-9 Detailed XPS spectra for immersed sample (black) and 1Cy polarized (red): F 1s, O 1s, C 1s and S 2p. a-d) on the surface, e-h) after 16 minutes of Ar^+ sputtering, i-l) after 60 minutes of Ar^+ sputtering.

Indeed, the presence of LiF, Li₂CO₃ and semi-carbonates on the surface on lithium electrode after galvanostatic polarization (Figure 5-9 (a-d)) implies that the reduction reactions are enhanced upon applying voltage. The difference in the SEI thickness is explored using Li 1s signal, shown in Figure 5-10.

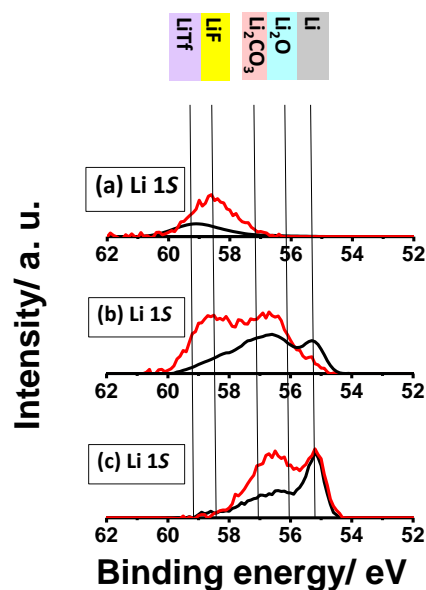


Figure 5-10 Detailed XPS spectra of Li 1s signal for immersed sample (black) and 1Cy polarized (red): a) on the surface b) after 16 minutes of sputtering c) after 60 minutes of sputtering.

Indeed, Li metal signal (55.2 eV) can be detected only after 60 minutes in the 1Cy sample, proving the existence of a thicker passivation layer.

5.2.2 Temperature and Salt Concentration Influence on the SEI

The influence of temperature on the SEI evolution has been investigated by impedance spectroscopy and XPS. The increase of temperature from 20 °C to 80 °C leads to a decrease of SEI resistance, R_{SEI} from 350 Ω to 25 Ω , indicating either a morphological or chemical change of the SEI, Figure 5-11. The changes in the SEI resistance are

reversible upon cooling.

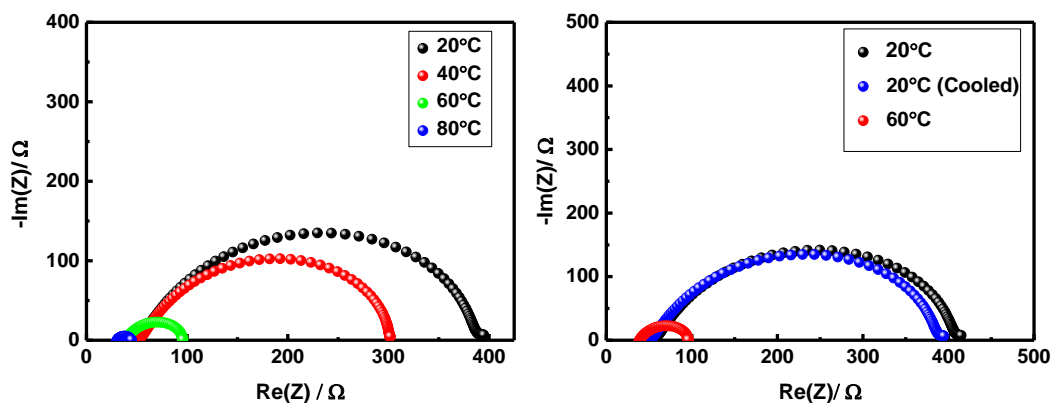


Figure 5-11 Temperature dependent impedance spectroscopy of Li | AAO: (1M LiTf / triglyme) | Li a) in the temperature range of 20°C to 80°C. b) reversibility of R_{SEI} amid changing the temperature.

To elucidate the chemical changes occurring during temperature increase the XPS spectra has been achieved at room temperature and in-situ at 60 °C, Figure 5-12.

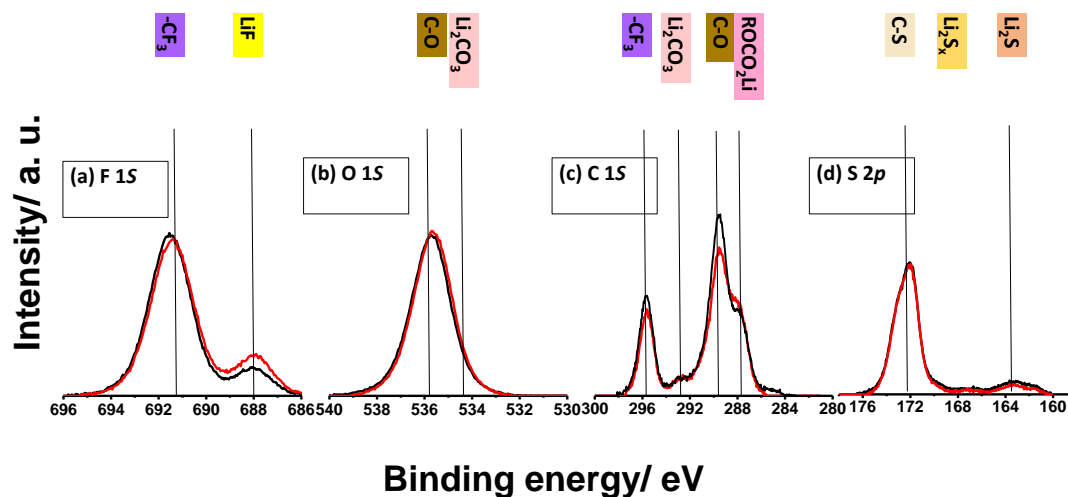


Figure 5-12 Detailed XPS spectra for sample at 20 °C (black) and sample at 60 °C: a-d) F 1s, O 1s, C 1s and s 2p.

No significant changes in chemical composition are detected during heating. The minor changes in LiF concentration originates from the decomposition of the residual LiTf salt on the surface. It implies that the SEI conductivity enhancement is most probably due to the morphological reformation possibly involving porosity evolution.

Additionally, the R_{SEI} shows the concentration dependant behaviour at $C_{salt} < 0.4$ M, Figure 5-13. In the concentration range of 0.4-1 M, R_{SEI} shows a constant value of 400 Ω . On decreasing the concentration to 0.02 M, R_{SEI} increases to exceptionally high values of 1600 Ω . The thickness derived from fitted capacitances is 0.1 nm for 0.02 M.

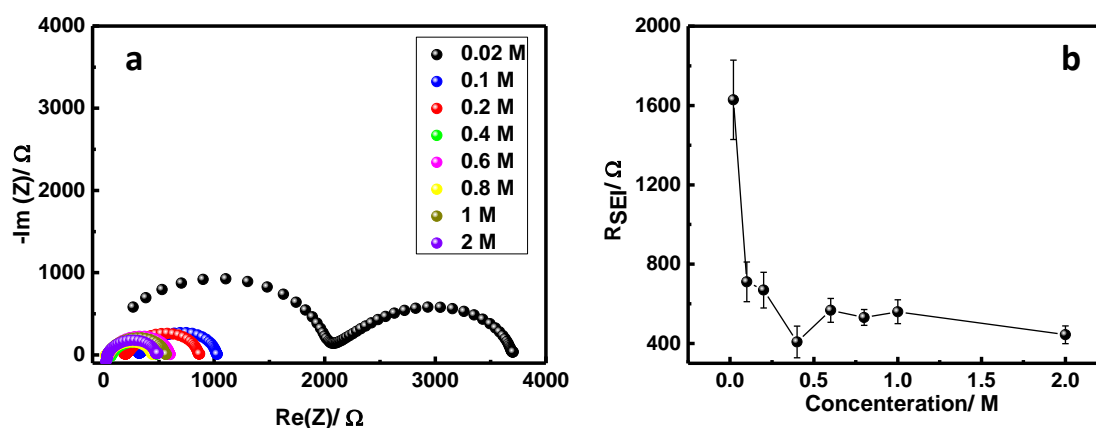


Figure 5-13 Salt concentration dependence of R_{SEI} a) in Li | AAO: (0.02-1 M LiTf)/triglyme | Li at RT.
b) the R_{SEI} vs. salt concentrations plot.

This concentration dependent behaviour is explored in detail using XPS. The XPS spectra for one time galvanostatically polarized sample in 0.02 M (Red) and 1 M (Black) LiTf/triglyme can be observed in Figure 5-14. The composition of the SEI differs substantially on changing salt concentration. The absence of LiF and Li_2S_x in 0.02 M is noticeable on the surface, while Li_2CO_3 , Li_2O and solvent residue are visible. Naturally, the lack of accessible fluorine leads to formation of more Li_2O and Li_2CO_3 and decrease in the conductivity of the SEI layer.

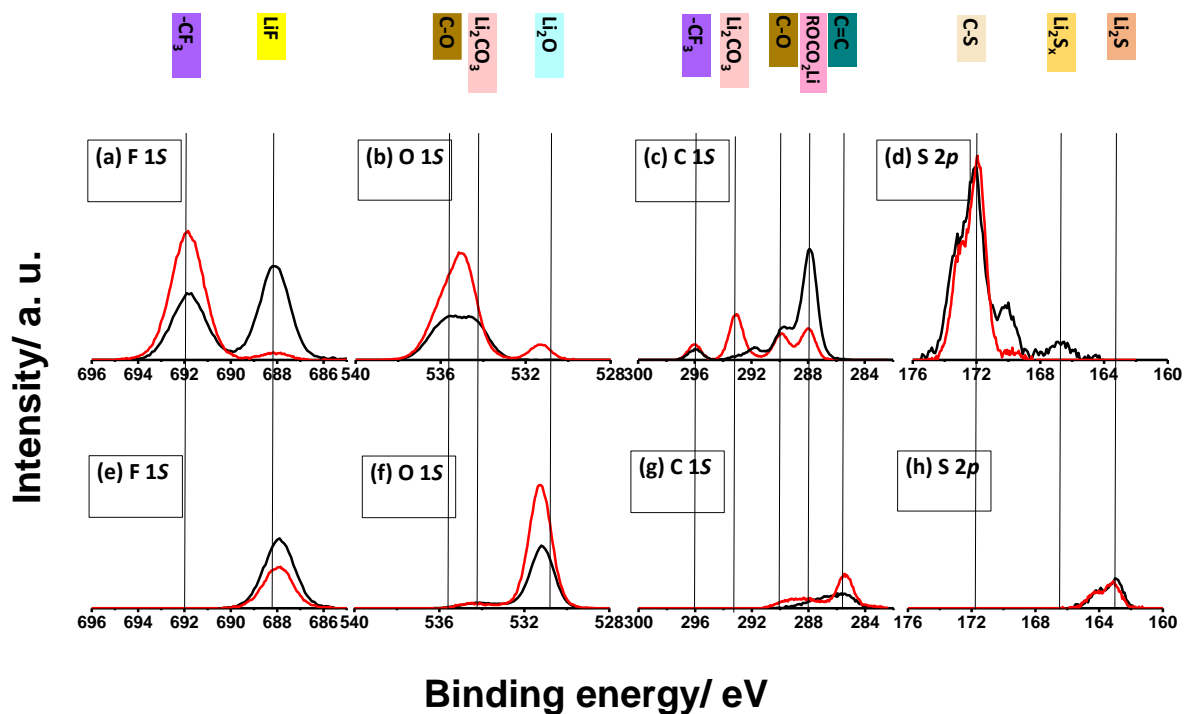


Figure 5-14 Detailed XPS spectra for one-time galvanostatically polarized for AAO: (1 M (black) and 0.02 M (red) LiTf/triglyme) : a-d) on the surface, e-h) after 60 minutes of Ar^+ sputtering.

Counterintuitively to the conductivity decrease on decreasing the salt concentration, the contribution of the pure Li signal to the Li 1s spectra at the surface for 0.02 M (red), Figure 5-15, indicates that the thickness of the SEI is comparatively smaller at $C_{\text{salt}} = 0.02 \text{ M}$.

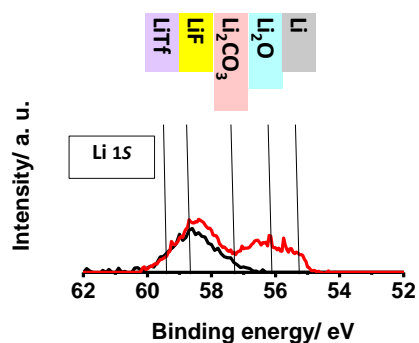


Figure 5-15 XPS spectra of Li 1s signal for one-time galvanostatically polarized AAO: 1 M (black) and 0.02 M (red) LiTf/triglyme).

5.2.3 Electrochemical Cycling Influence on the SEI

It is observed that polarization cycles lead to R_{SEI} changes as shown in Figure 5-16. Interestingly, the time and cycling aging effects evolve the SEI differently.

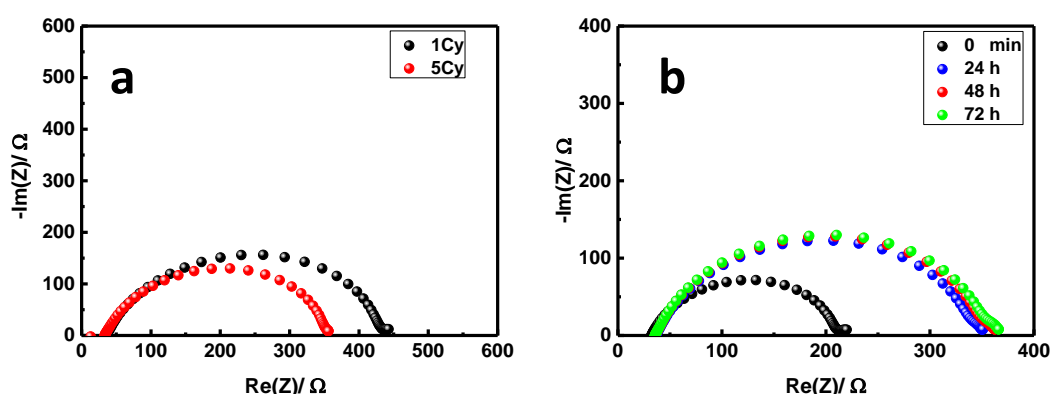


Figure 5-16 Impedance spectroscopy of Li | AAO: (1 M LiTf / triglyme) | Li cell: a) changes upon galvanostatic polarization. b) changes upon time aging at OCV conditions.

The R_{SEI} keeps growing from 150 to 350 Ω under OCV condition in the first 24h. The growth continues with a lower reaction rate afterwards. However, upon galvanostatic polarization cycles, a decrease of R_{SEI} from 400 Ω to 300 Ω is observed. The XPS spectra (after 60 minutes of sputtering with Ar^+ ions) of the SEI layer formed after 1Cy polarization (black) and 5Cy polarizations (red) are shown in the Figure 5-17.

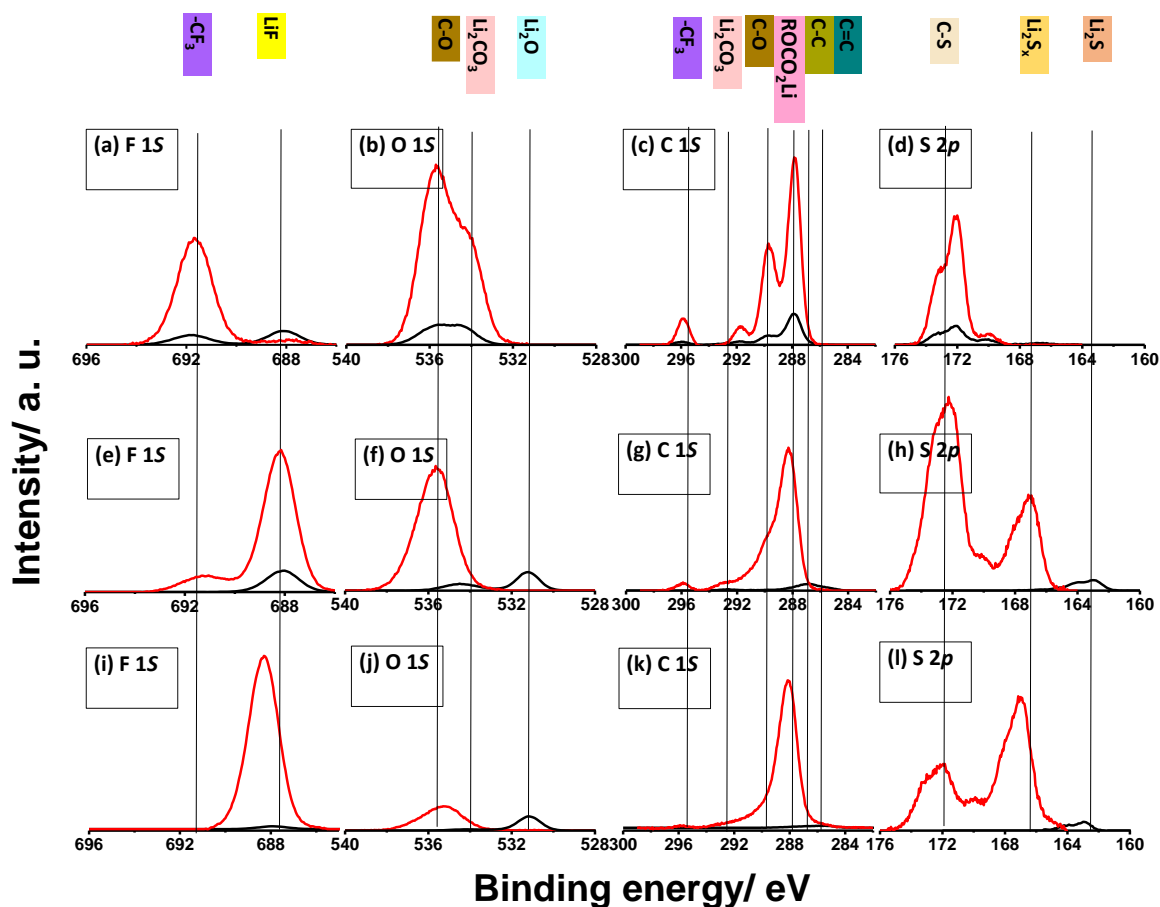


Figure 5-17 Detailed XPS detail spectra of) F 1s, O 1s, C 1s and s 2p for 1Cy (black) and 5Cy (red): a-d) on the surface, e-h) after 16 minutes of Ar⁺ sputtering, i-l) after 60 minutes of Ar⁺ sputtering.

The chemical compositions of the SEI layers in both samples are comparable, while the amount of each compound and thickness of the SEI vary remarkably. As it can be seen in the XPS spectra of the 5Cy, there is a strong contribution of LiF in the F 1s signal and of Li₂CO₃ in C 2p signal on the surface and after sputtering, indicating further formation of these compounds upon cycling. On the other hand, no Li₂O is observed in the 5Cy sample. Furthermore, the solvent residual is detected even in the inner layer of the SEI, suggesting the absence of bilayer structure of the SEI after the cycling. The comparison of Li 1s signal and FIB-SEM images of these two samples, Figure 5-18, complement the previous XPS results. Even after 60 minutes of sputtering, no contribution from the pure Li metal is visible in 5Cy sample, suggesting SEI thickness

being greater than 200 nm.

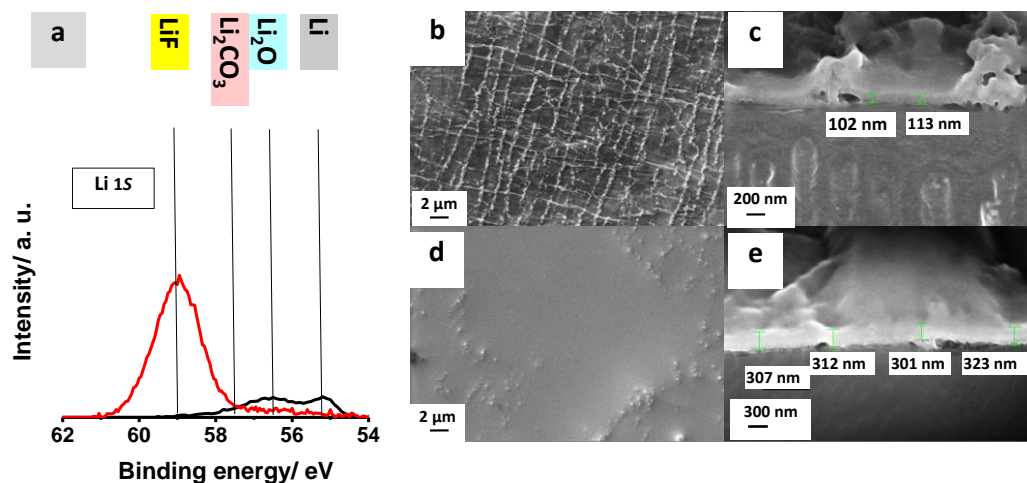


Figure 5-18 a) Li 1s signal after 60 minutes of Ar⁺ sputtering 1Cy (black) Vs 5Cy (red); b and c) SEM-FIB images of the 1Cy; c and d) SEM-FIB images of 5Cy.

This is consistent with the thickness observed in FIB-SEM images. It seems that the resistance and thickness of the SEI behave unexpectedly; the thickness increases upon cycling while the R_{SEI} decreases. To explain this obvious strong increase in the ionic conductivity of the SEI layer, more insight into the volume fraction of different phases, their bulk conductivities as well as the morphology evolution upon cycling would be essential. For example one possible explanation could be that the formation of highly conducting LiF /Li₂CO₃ interfaces might be responsible for the increase in ionic conductivity of SEI upon cycling. Indeed, the space charge layer formation at such interfaces has been suggested to be responsible for the enhancement in a concentration of ionic carriers [117-120]. It has been reported that Li₂CO₃ is a good electronic insulator with relatively high ionic conductivity $\sigma_{\text{ionic}} \approx 10^{-8}$ having the Li ion interstitials (Li_{Li}^{\bullet}) as the main charge carrier [121]. On the other hand, LiF is a poor ionic conductor ($\sigma_{\text{ionic}} \approx 10^{-31}$), with Li vacancies (V_{Li}') as main charge carrier [122]. At the LiF/ Li₂CO₃ interface it might be energetically favorable for Li ion to partially redistribute from LiF to Li₂CO₃, resulting in enhancement in $[Li_{Li}^{\bullet}]$ in Li₂CO₃ and $[V_{Li}']$ in LiF similar to the LiF/TiO₂ interface [118]. This enhancement in concentration of the ionic carriers near the interface is accompanied by a suppression of the electronic

carriers. This suggests that the formation of more LiF/ Li₂CO₃ interfaces can simultaneously increase the ionic conductivity and electronic resistivity, both being beneficial for cyclability of the SEI.

5.2.4 SEI Modification for Lithium Metal Battery

In the current study, an attempt to investigate the effect of the presence of other lithium compounds such as Li₃N and LiCl in the SEI is presented. This has been done utilizing an alternative salt, LiTfI and chlorotrimethylsilane as the source of nitrogen and chlorine.

5.2.4.1 Electrode Pre-Passivation

Figure 5-19 exhibits the AC measurements before and after polarization for the Li |AAO: (1M LiTf/triglyme)| Li cell using chlorotrimethylsilane-passivated lithium metal. Although the initial R_{SEI} appears to be lower in comparison to the non-passivated lithium electrode, it increases after 1Cy polarization.

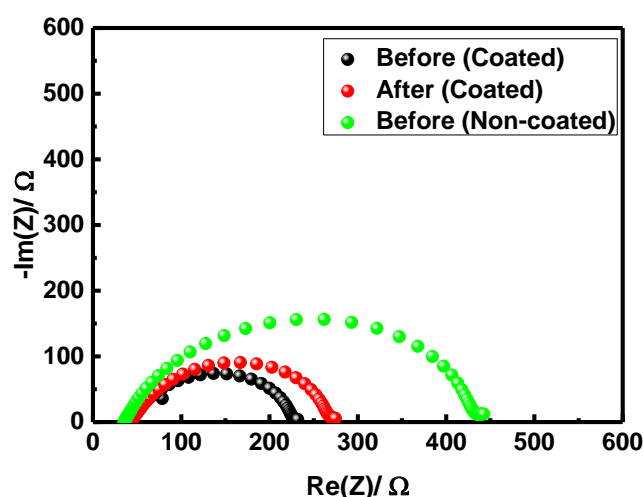


Figure 5-19 EIS of Li | AAO: 1M LiTf / triglyme| Li at RT for chlorotrimethylsilane -passivated electrode before polarization (black), chlorotrimethylsilane-passivated electrode after polarization (red) and non-passivated electrode before polarization (green).

The XPS results of the passivated electrode after 1Cy polarization are depicted in Figure 5-20 a-f. In addition to common XPS spectra of non-passivated sample, Cl 1s and Si 2p are recorded. The C 1s signal at 201.7 eV is corresponding to LiCl and the Si 2p signal at 113 eV is assigned to the siloxane group.

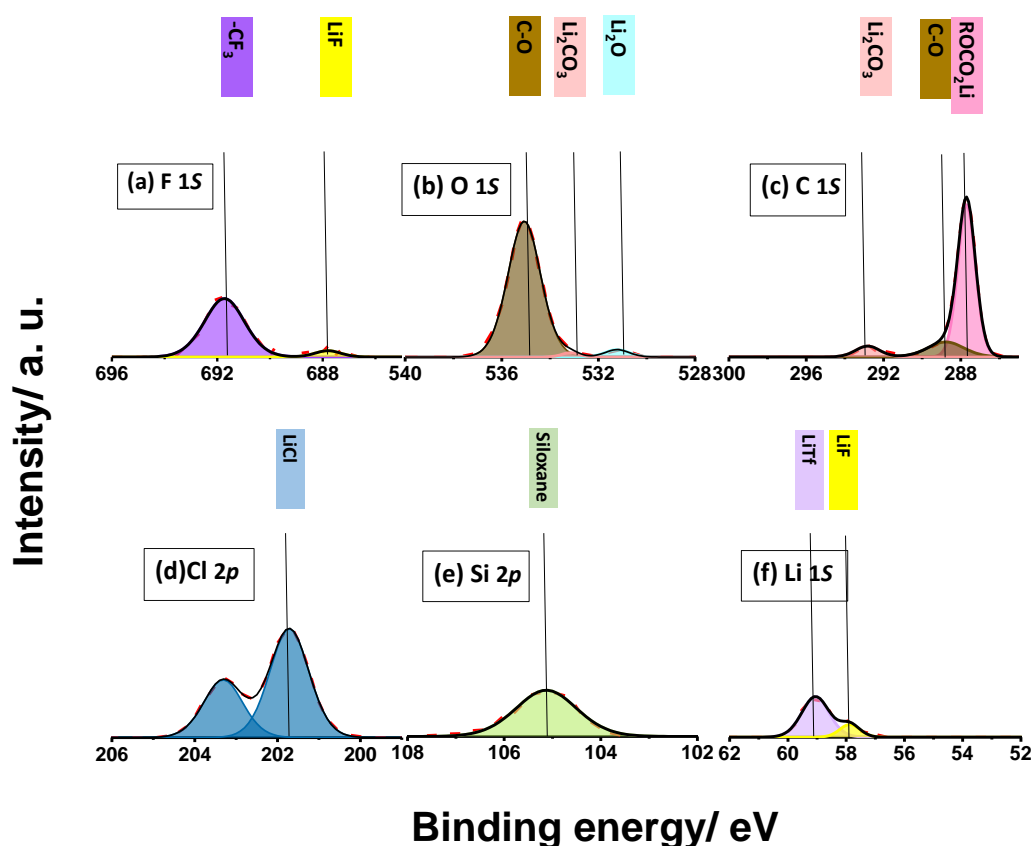


Figure 5-20 Detailed XPS spectra for chlorotrimethylsilane-passivated electrode after 1Cy polarization.

In addition to the F 1s, O 1s, C 1s and S 2p signal Cl 2p and Si 2p are observed.

However, the amount of LiF remains negligible even after sputtering shown in (appendix A Figure 12). The Li 1s signal after 16 minutes Ar⁺ ion sputtering for the non-passivated (black) and passivated (red) samples, Figure 5-21, implies that the SEI is relatively thinner in the passivated lithium case.

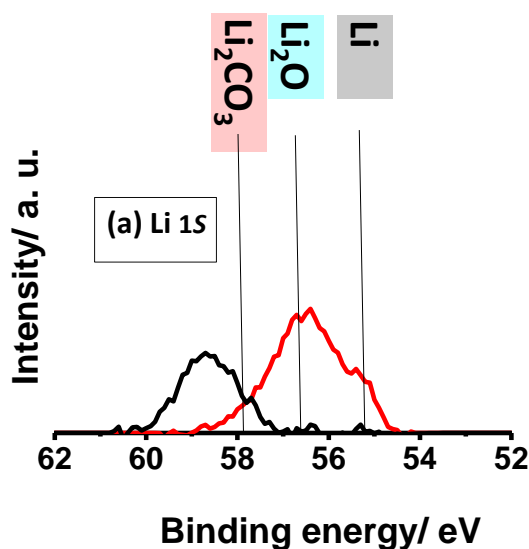


Figure 5-21 The Li 1s XPS spectra after 16 minutes of Ar⁺ sputtering for non-passivated (black) and passivated (red) lithium electrode after one-time galvanostatic polarization. The contribution of pure Li can be seen for the passivated sample, indicating that the SEI thickness is smaller.

The absence of LiF formation in the case of the pre-passivated sample could be the reason for the growth of the SEI after polarization, as LiF has been reported to improve the cyclability of Li metal by suppressing the electrode/electrolyte reaction due to the low solubility in organic solvents [73, 123, 124]. A further electrochemical investigation (stripping-plating) is not attempted due to the observed instability of the SEI.

5.2.4.2 Chemical Composition of SEI

As already shown, the reduction of the Li₂S upon cycling to Li₂S_x compounds causes the instability of the SEI in the LiTf/triglyme system. In order to manipulate the composition of the SEI and to avoid the formation of Li₂S_x, LiTf is substituted with LiTfDI. The conductivity of the electrolyte is higher for Li| 1M LiTfDI/triglyme: AAO| Li while the R_{SEI} shows comparable values of 315 Ω , Figure 5-22.

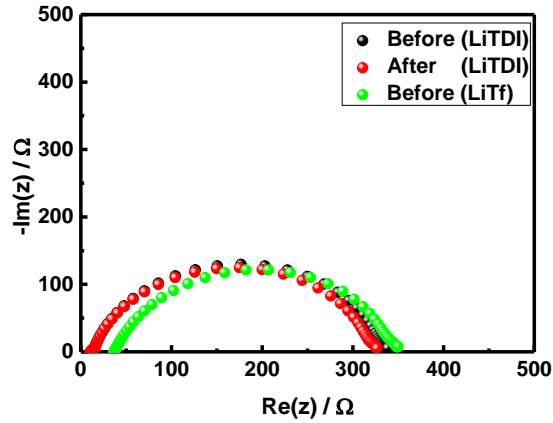


Figure 5-22 The EIS of Li|AAO: (1M LiTf/triglyme | before (black) and after (red) galvanostatic polarization. The R_{SEI} value seems to be analogous to LiTf sample (green).

The XPS spectra on the lithium surface and after 16 minutes of sputtering is shown in Figure 5-23. The signal at 402.8 eV in N 1s on the surface corresponds to the N-C band in the LiTf residual.

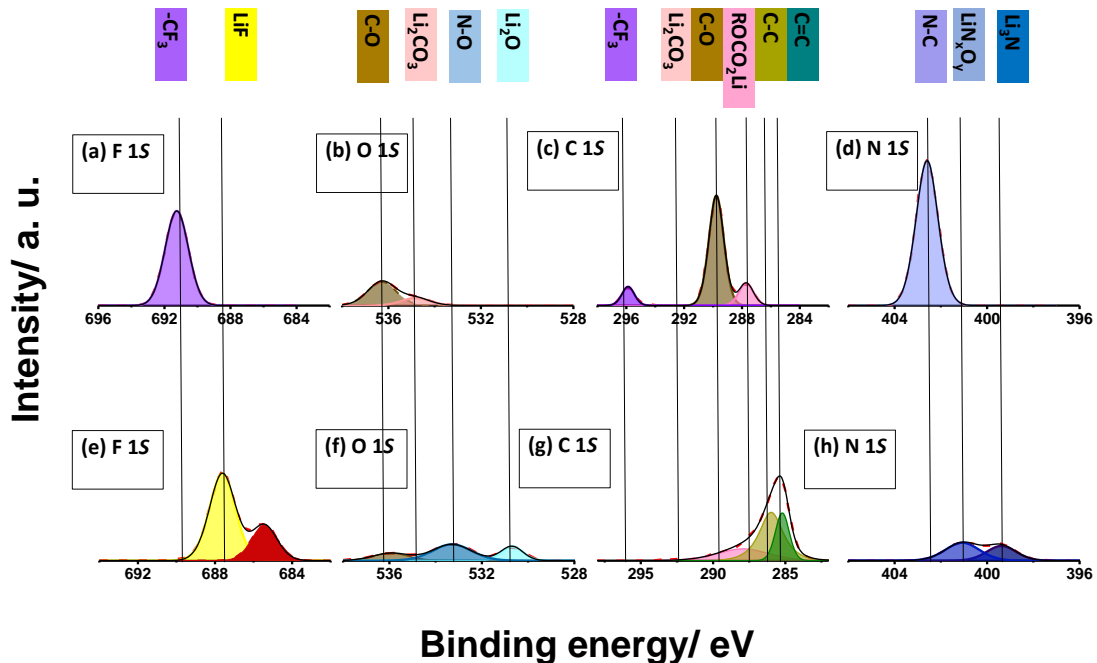


Figure 5-23 Detailed XPS detail spectra for lithium electrode in contact with LiTf after 1Cy polarization in addition to the F 1s, O 1s, C 1s signal, the N 1s is observed. Notable amount Li_3N could be observed while almost no Li_2CO_3 and smaller amount of organic phases are detected.

The N 1s signal upon Ar⁺ sputtering is attributed to Li₂N_xO_y and Li₃N at 401 and 399 eV, respectively. However, no significant amount of Li₂O and Li₂CO₃ is noticed, even after Ar⁺ sputtering. The Li 1s signal comparison for LiTf and LiTf, after 60 minutes of Ar⁺ ion sputtering, Figure 5-24(a) proposes the formation of the thicker SEI in agreement with the obtained FIB-SEM image Figure 5-24 (b and c). The comparable value for R_{SEI} despite the formation of thicker SEI on lithium metal in contact with the LiTf based electrolyte could be explained through the high ionic conductivity ($\sigma_{ionic} \approx 10^{-4}$) of Li₃N [125, 126].

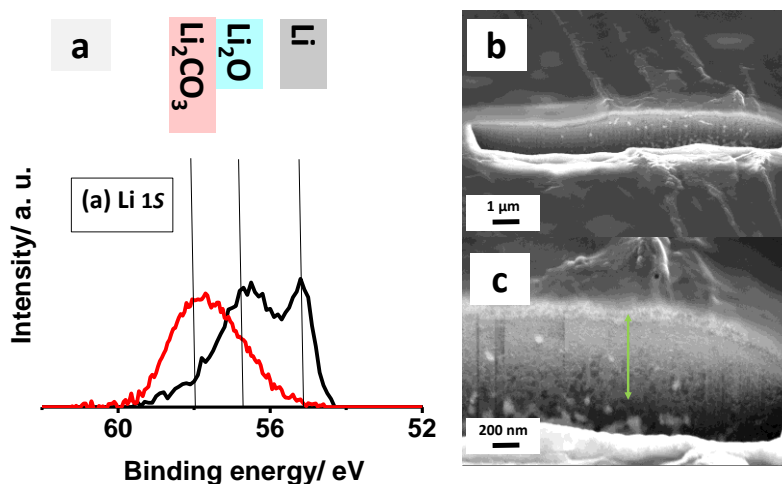


Figure 5-24 The SEI thickness investigation with LiTf electrolytes: a) Li 1s signal after 60 minutes of Ar⁺ ion sputtering in the LiTf sample (red) and LiTf sample (black). No pure lithium contribution is seen for LiTf sample; b and c) FIB-SEM cross section image of SEI formed on lithium metal in contact with LiTf seems to be very thick.

To further investigate cyclability of these two salts in contact with lithium metal electrodes, a cyclic lithium stripping-plating procedure consisting of 1-hour charging followed by 1-hour of discharge was employed in the identical symmetric cell. Figure 5-25 illustrates the time-dependent voltage profile under applying a constant current density of 0.1 mA cm⁻² in AAO: 1M LiTf/triglyme and AAO: 1M LiTf/triglyme. Indeed, the LiTf system appears to be more stable while LiTf indicates a constant increase in impedance even after 25 cycles and eventually early cell failure due to the formation of mossy lithium deposits. In addition to the high σ_{ionic} and low σ_e of Li₃N,

the elasticity of the passivation layer formed on lithium metal in contact with LiTDI consisting solvent could play an important role in cyclability of this cell [127]. It is theoretically shown that the passivation layer formed on the lithium metal in contact with N_2 has the highest elasticity, preventing the formation of cracks and growth of dendrite [128].

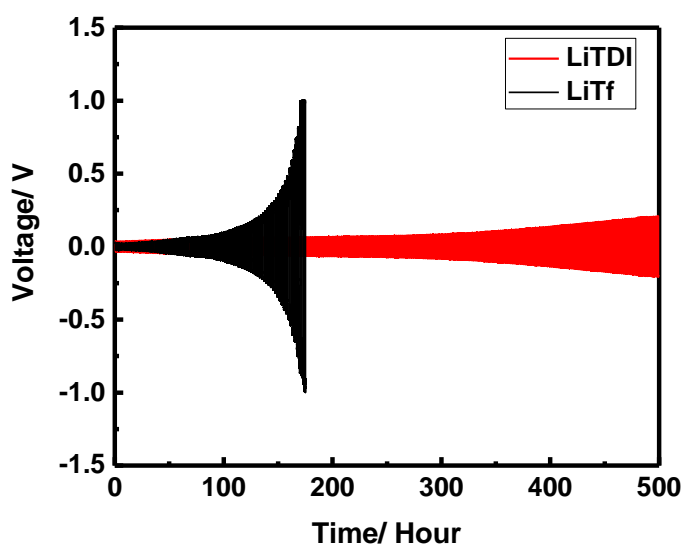


Figure 5-25 The stripping-plating experiment with the current density of 0.1 mA cm^{-2} for Li| 1M LiTf/triglyme: AAO| Li (black) and Li| 1M LiTfDI/triglyme: AAO| Li (red). The LiTf cell fails before 200 hours.

5.3 Conclusions

Hereby, the electrochemical behaviour, composition and morphology of the SEI layers formed on the lithium metal electrode in contact with glyme-based electrolytes is investigated. According to FIB-SEM, the thickness of the SEI appears to be hundreds (100-300) of nanometers.

The SEI thickness increases upon galvanostatic cycling while its resistivity decreases, indicating an increase in ionic conductivity of the SEI. Furthermore, the effect of salt concentration is studied. At lower salt concentration, a thin and highly resistive SEI layer composed of mostly organic phases is observed. The increase in temperature does not change the composition of the SEI despite the significant depletion in R_{SEI} values indicating possible porosity evolution.

To avoid the reactive Li_2S components in the SEI, LiTf salt is replaced with nitrogen-rich LiTDI. The SEI formed in contact with glyme-containing LiTDI is composed of mostly inorganic phases including LiF and Li_3N without Li_2CO_3 and organic phases. High conductivity of Li_3N and absence of phases such as Li_2S_x improve the cyclability of the LiTDI-containing solid/liquid composite electrolyte. The passivation layer elasticity might also partially play the role in the improved cyclability of the cell in the latter case.

Chapter 6 General Conclusions

The present work deals with interfacial effects of LiTf/triglyme electrolytes in lithium cells. A major part is devoted to the electrochemical behaviour of solid-liquid composite electrolyte consisting of nano-porous anodic alumina oxide (AAO) infiltrated by lithium triflate/triglyme.

The ideal solid-liquid interface exhibits charging and hence space charge zones, whose thicknesses are determined by the screening length. The ionic speciation, interfacial structuring and screening length of LiTf/triglyme in contact with muscovite mica have been investigated implementing multiple techniques such as surface force apparatus (SFA), infrared spectroscopy (IR) and impedance spectroscopy (IS). The interfacial layer consisting of two regions (0-4nm) and (4-15nm) is recorded by the SFA experiment for this electrolyte. The negative value of zeta potential for this system implies anion adsorption on the surface of the mica. The effective screening lengths measured by surface force apparatus are about 8nm for the concentrated systems (0.2-1M), considerably larger than expected from pairing and electrostatic correlation, indicating complex long-range interactions. The same effects are expected in the solid-liquid composite electrolyte as well as for the lithium electrode-glyme electrolyte contact.

The solid-liquid composite electrolyte composed of nano-porous anodic alumina infiltrated with LiTf/triglyme has been investigated in a symmetrical lithium cell. The enhanced lithium transference number (0.45) associated with high conductivity of (0.3 mS cm⁻¹) for 1M are measured, indicating a medium level of adsorption. The transference number appears to increase ($t_{Li} \approx 0.8$) at lower concentrations (0.02 M) and elevated temperature 80°C, explainable in terms of charge carrier concentrations and mobilities in the composite electrolyte. As far as application is concerned, this class of electrolytes shows much lower over-potential for hundreds of cycles in stripping-plating experiments.

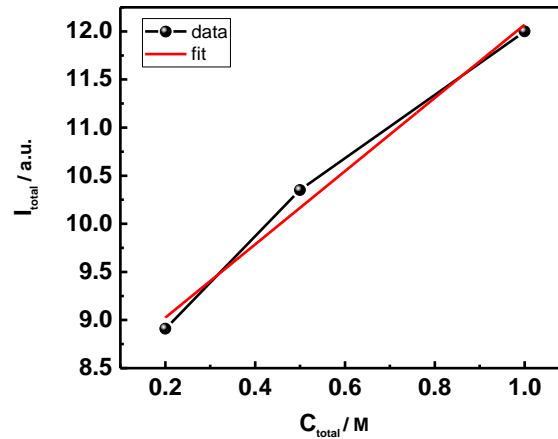
The electrode/electrolyte interface is additionally complicated by the formation of

passivation layer. Formation, composition and morphology of the solid electrolyte interphase (SEI) on lithium metal in contact with AAO: (LiTf/triglyme) are probed by means of impedance spectroscopy, X-ray photoelectron spectroscopy and Focused-Ion-Beam (FIB) scanning electron microscopy.

The SEI on the lithium electrode in contact with the LiTf-containing glyme-based electrolyte is composed of inorganic LiOH, Li₂CO₃, LiF and organic species such as RCH₂OLi and C-S containing molecules. Upon argon sputtering, additional Li₂O, Li₂S emerge. The thickness of the SEI is on the order of 100 nm after one galvanostatic concentration polarization and increases to 300 nm after five galvanostatic concentration. The effects of temperature, salt concentration and anion of the salt are explored regarding morphology and composition evolution. Despite the decrease in the resistance of the SEI upon elevating temperature, no obvious changes in the chemical composition have been detected. This suggests morphological restructuring of the passivation layer. The formed SEI at lower concentration of salt appears thinner and mainly consists of organic matter explaining the higher resistance of the passivation layer. These investigations lead to the interesting finding that the resistance of SEI is more dependent on the composition rather than the thickness. For the application, the formation of Li₃N is shown to be favourable over the formation of Li₂S. Therefore, LiTfDI salt is recommended as salt rather than LiTf.

Appendix

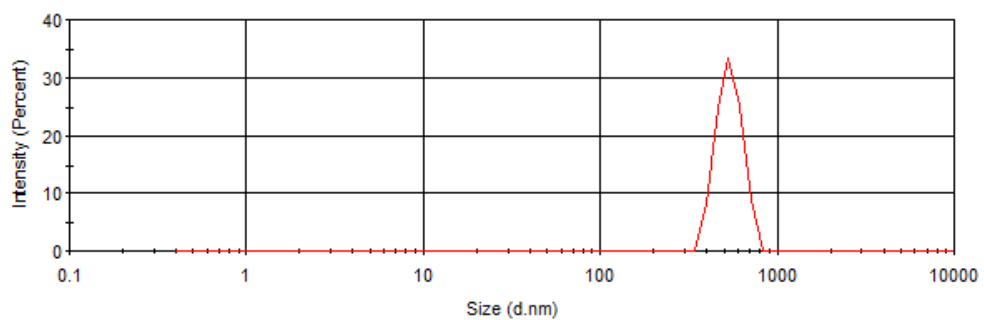
Beer law for IR



A Figure 1 Total intensity is proportional to the total concentration, indicating the similar sensitivities for different species.

DLS

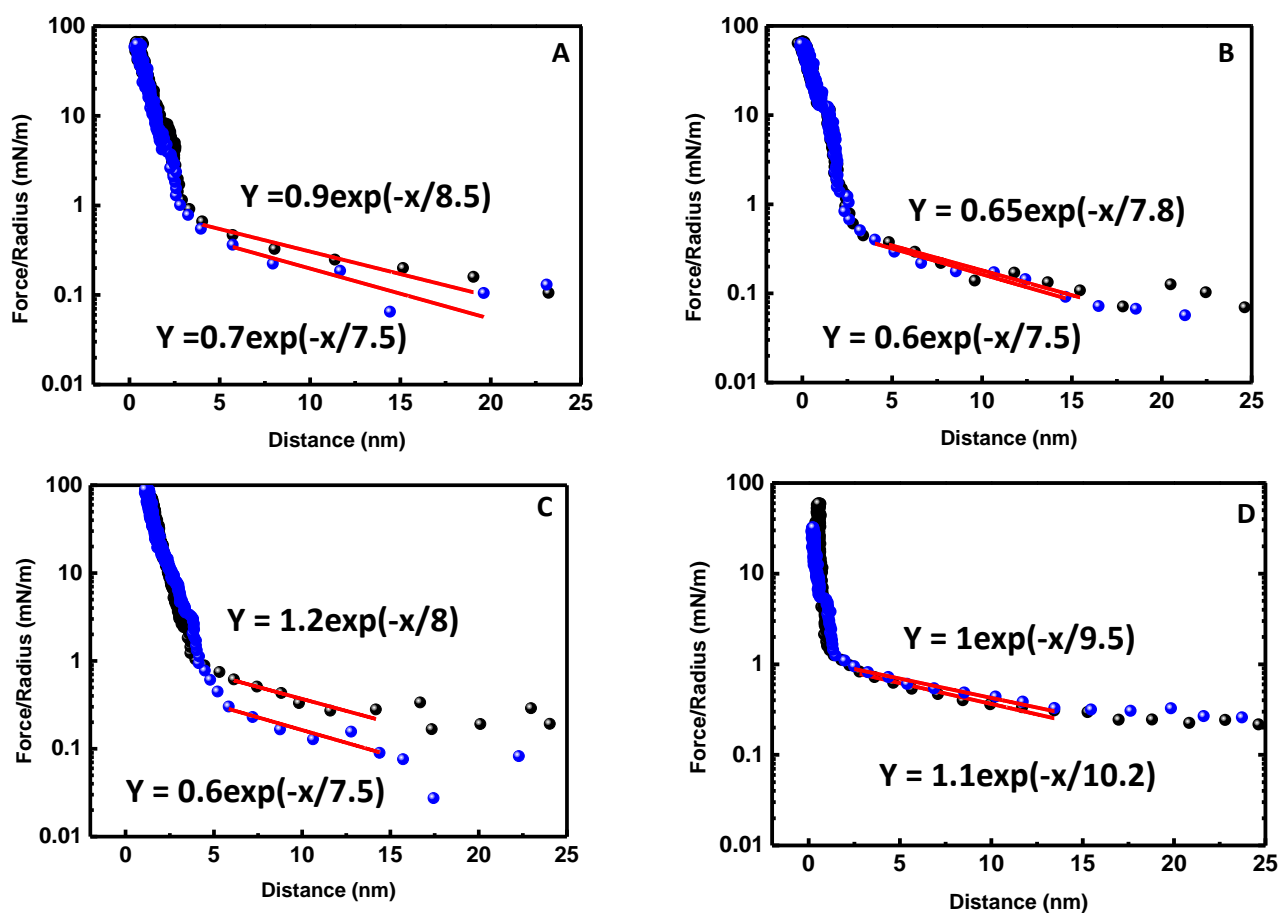
The room temperature particle size measurement based on a Dynamic Light Scattering principle (Zetasizer Nano S, Malvern) shows narrow distribution around 500 nm confirming particle aggregation.



A Figure 2 Particle size distribution of 1 vol% Mica in 1 M LiTf/triglyme

Force-distance Profile for Different Concentration

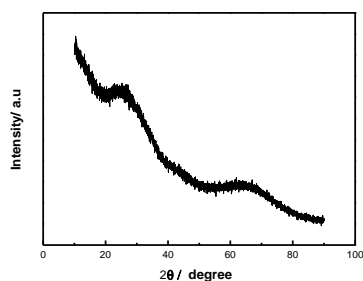
The force-distance profiles and corresponding exponential decay fits for concentrated LiTf/triglyme electrolytes ($C > 0.2M$) are indicated in A3. The black and blue data points correspond to two subsequent SFA runs.



A Figure 3 SFA force-distance profiles between symmetric Mica in triglyme (black and blue) and the corresponding fitted exponential decay (red) for LiTf concentrations: a) 0.2M, b) 0.3M, c) 0.5M, d)

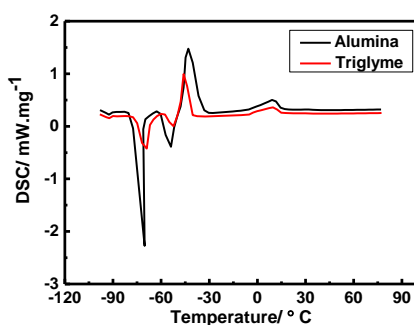
0.7M

XRD of the AAO



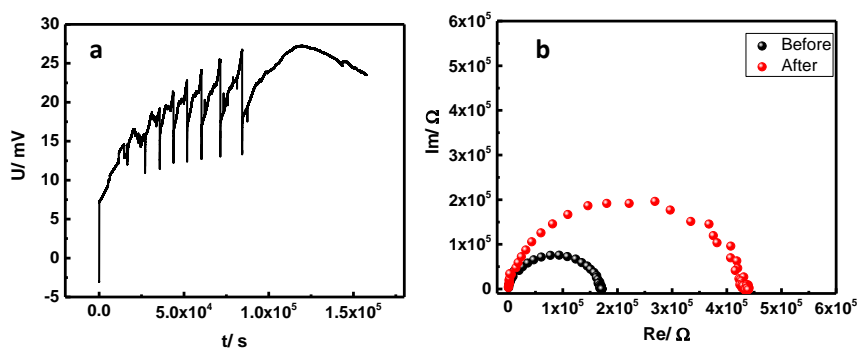
A Figure 4 X-ray diffraction pattern of one membrane revealing the amorphous structure of the material

DSC Measurement of Triglyme and 1M LiTf/ triglyme



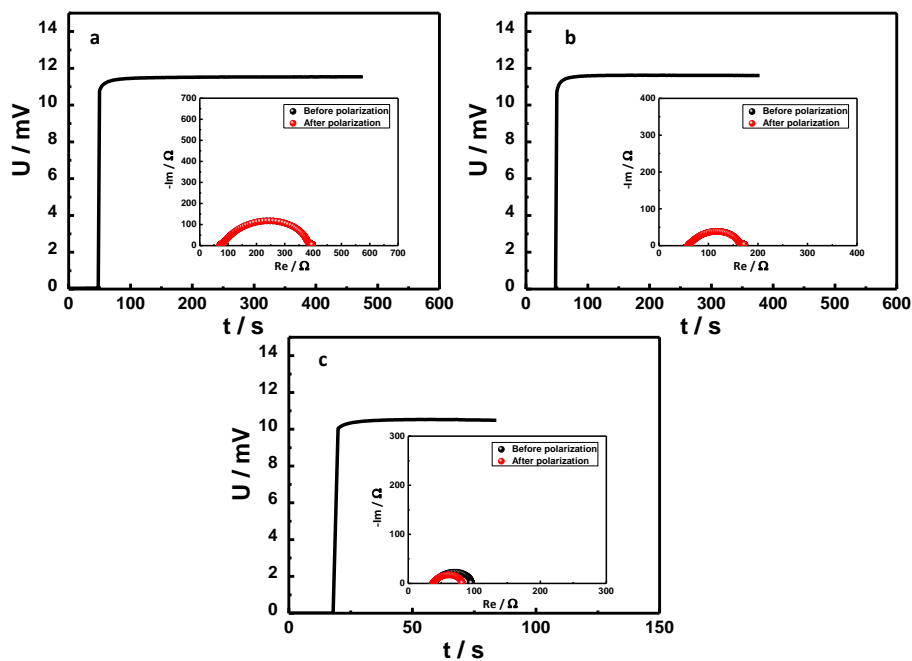
A Figure 5 DSC measurement of pure triglyme and 1M LiTf/triglyme.

Transference Number for liquid 1M/ triglyme



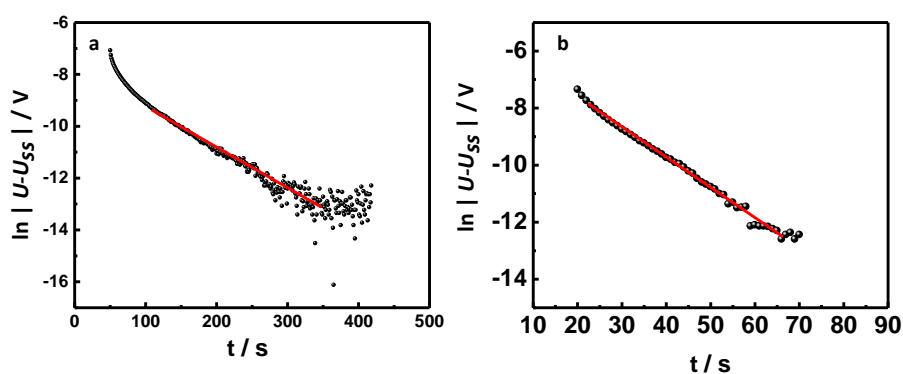
A Figure 6 a) Galvanostatic polarization curve for 1 M LiTf/triglyme. b) Impedance spectra before (black) and after (red) the galvanostatic polarization. Observed semicircle corresponds to the SEI resistance, changing during the polarization. The measured transference number is 0.15

Galvanostatic Polarization at Different Temperature



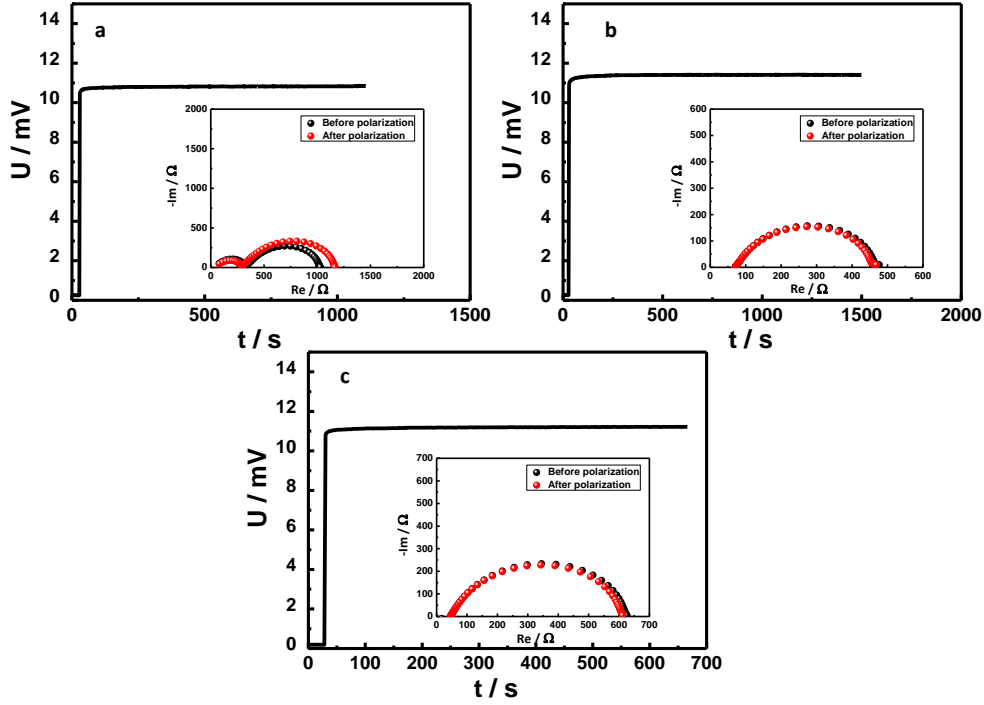
A Figure 7 Temperature dependent galvanostatic polarization of AAO: (1 M LiTf/triglyme) and AC measurement before and after polarization. A) 35 °C b) 45 °C c) 60 °C

Diffusion Coefficient at Different Temperature



A Figure 8 The extracted salt diffusion coefficient from the long polarization times for left) 10 °C, Right) 80 °C

Galvanostatic Polarization for Different Salt Concentration



A Figure 9 Concentration dependent galvanostatic polarization of AAO: (LiTf/triglyme) and AC measurement before and after polarization. A) 0.1 M LiTf b) 0.4 M LiTf C) 0.6 M LiTf

Surface Area, Number of OH Groups and Saturation Concentration:

$$A_{pore} = \pi(R + r)\sqrt{(R - r)^2 + h^2} \quad \text{A Equation 1}$$

$$N_{pores} = 1.25 * 10^{10}$$

$$Surface\ area = \frac{A_{pore} \times N_{pore}}{m_{pallet}} \approx 35 \quad \text{A Equation 2}$$

$$m_{electrolyte} \ , \ m_{pellet}$$

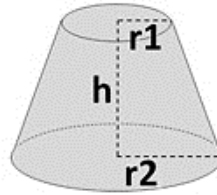
$$A_{total} = surface\ area \times m_{pellet} \quad \text{A Equation 3}$$

$$N_{OH} = 6 * A_{total} \quad \text{A Equation 4}$$

$$N_{Li+} = N_A C_{salt} \frac{m_{liquid}}{d_{liquid}} \quad \text{A Equation 5}$$

$$C_{salt} = \frac{N_{OH}}{N_{Li^+}}$$

A Equation 6



A Figure 10 The pores structure in frustum form.

Depression in conductivity:

For concentrated system (1M) obtained from IR experiment (see part 3.2.1):

$$c_{Li^+} = c_{X^-} = \frac{1}{4} c_{pair} = \frac{1}{5} c_{salt}$$

A Equation 7

If we take into account the u_{Li^+} and u_{X^-} , derived from the deconvoluted contributions of specific ions to the overall conductivity (σ_+ , σ_-) for the similar system in the previous work [77]:

$$\frac{u_-}{u_+} \approx 18$$

A Equation 8

For dilute system (0.2M) obtained from IR experiment (see part 3.2.1):

$$(c_{Li^+} = \frac{1}{2} c_{pair} = \frac{1}{3} c_{salt})$$

A Equation 9

And mobilities [77]:

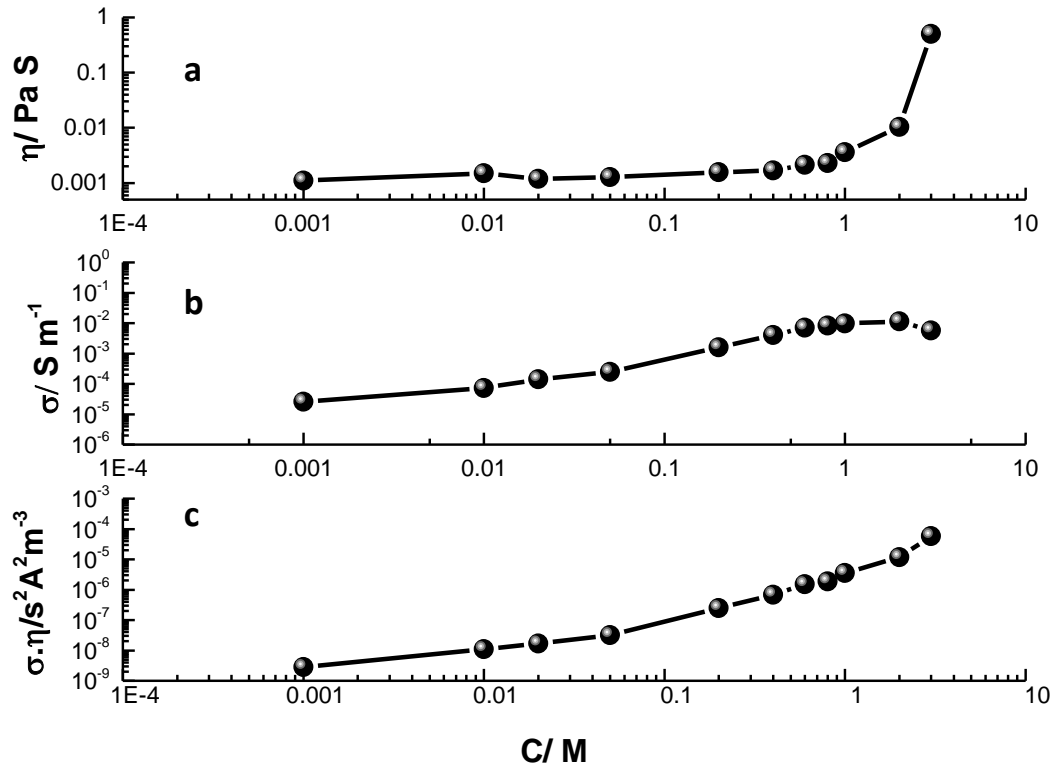
$$\left(\frac{u_-}{u_+} \approx 4\right)$$

A Equation 10

Consequently:

$$\frac{\sigma_m}{\sigma_\infty} = \frac{(1-\varphi)c_{salt} u_+}{(c_{salt}/3)(u_+ + u_-)} \approx 0.5$$

A Equation 11

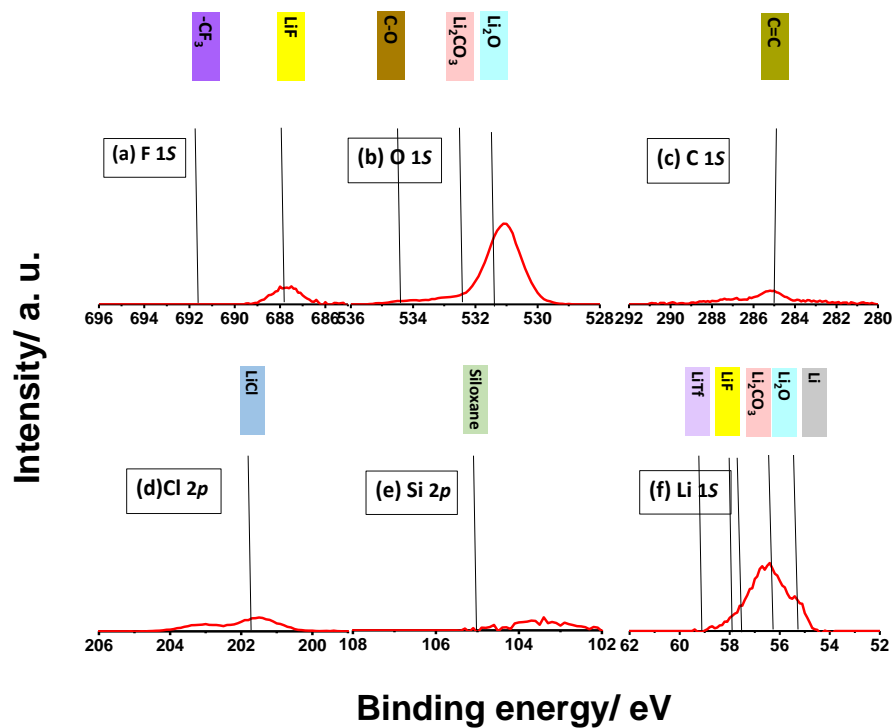
Viscosity-Concentration:

A Figure 11 The effect of salt concentration on a) viscosity b) conductivity.

A Table 1 BE assigned to different SEI typical compositions [40, 114, 129, 130]

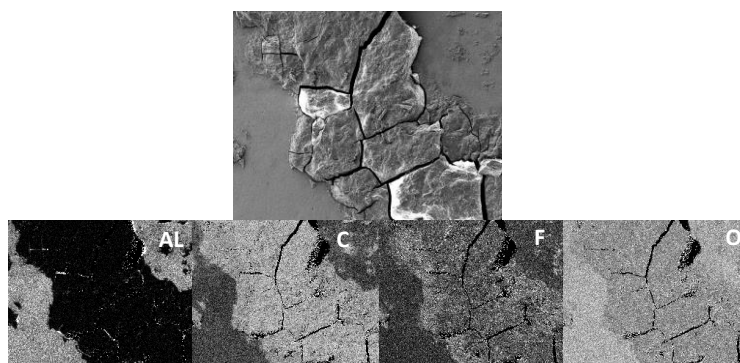
Chemical bond assignment		BE(eV)
C1s	C=C , C-C	286.5
	ROCO ₂ Li	288
	C-O	288.5
	Li ₂ CO ₃	290
	CF ₃	293
O1s	C-O	532.8
	Li ₂ CO ₃	531.2
	Li ₂ O	529.5
F 1s	LiF	684.6
	C-F	688
Li 1s	Li	54.7
	LiF	57
	Li ₂ CO ₃	55.2
	Li ₂ O	55.6

Sputtered XPS spectra for Silane coated sample



A Figure 12 Detailed XPS spectra for chlorotrimethylsilane-passivated electrode (1Cy) after 16 minutes of sputtering.

Characterization of the Deposited Lithium



A Figure 13 EDS elemental mapping images showing distribution of C, F, Al and O on the deposited lithium on the Alumina.

List of Figures

Figure 2-1 Gouy-Chapman-Stern model for EDL at solid-liquid interface. This model consists of 2 layers: Stern and diffuse layer.	6
Figure 2-2 Formation of the space charge and profile of concentration and conductivity as function of distance from the surface of oxide particle [11].	10
Figure 2-3 Normalized ionic conductivity of the “soggy sand” electrolyte as a function of the volume fraction of added particle [14].	11
Figure 2-4 Lithium transference number dependence on the volume fraction of the added particles.	12
Figure 2-5 Electrolyte confined in the surface active nano-channels removing the bulk effect.	13
Figure 2-6 Schematic mosaic structure of SEI including organic and inorganic phases. The mosaic structure can have a bilayer form with an inner inorganic and outer organic layer [16].	15
Figure 2-7 Highly simplified charge transfer mechanism at electrolyte/ SEI, SEI, SEI/ electrode interfaces. Each step could be the rate determining step [40].	16
Figure 2-8 Removal and re-deposition of the Li ion underneath the SEI layer causes a crack and forms the passage for the reactive lithium metal to grow through.	17
Figure 3-1. Molecular structure of glymes.	21
Figure 3-2 Molecular structure of the lithium triflate salt.	23
Figure 3-3 Crystal structure of muscovite mica. The oxygen atoms are depicted red, the potassium ions are depicted in blue, and the aluminium/silicon atoms are depicted green.	23
Figure 3-4 Simplified SFA setup showing the major parts of the instrument [83].	24
Figure 3-5 Fringes of equal chromatic order (FECO) reveal the information about the distance between the two mica surfaces in SFA. Top: Surfaces separated from each other. Bottom: Surfaces in contact with each other. The wavelength shift between the contact and the separated surfaces is shown between the two red lines [84].	25
Figure 3-6 Infrared spectra of the triflate stretching band for 1M LiTf/triglyme electrolyte. The concentration of the free ions (green), ion pairs (purple) and dimers (orange) has been determined from the Gaussian-Lorentzian fit (dashed red line) of the total measured spectra (continuous blue line).	29
Figure 3-7 Infrared spectra of the triflate stretching band for left) 0.2 M LiTf/triglyme Right) 0.5 M LiTf/triglyme.	30
Figure 3-8 SEM image of dry ball-milled mica particles [92].	32
Figure 3-9 Shear viscosity of 1 M LiTf/triglyme compared to 1 vol% Mica: (1 M LiTf/triglyme) [92].	33

Figure 3-10 The effective Zeta potential of 1M LiTf/triglyme as a function of mica particle volume fraction [92].	34
Figure 3-11 Temperature dependent ac-conductivity 1M LiTf/triglyme and 1 vol% Mica: (LiTf/triglyme).	34
Figure 3-12 Force distance plot of specific interactions between two mica surfaces in contact with the pure triglyme and corresponding interfacial structuring through time. Black lines are the fitting curves according to de Gennes theory describing the force-distance characteristics across two approaching cylindrical surfaces covered with interfacially bound polymer layers [92].	35
Figure 3-13 Brush-like polymer layer growing due to K^+ complexation centers [92].	36
Figure 3-14 Force distance plot of specific interactions between two mica surfaces in contact with pure triglyme (blue), 0.2M LiTf/triglyme (green), and 1M LiTf/triglyme (red).	37
Figure 3-15 Schematic of interfacial structuring on mica surface exposed to LiTf/triglyme electrolyte [92].	38
Figure 3-16 Two subsequent recorded SFA force-distance of Mica sheets in contact with triglyme (black and green) and the corresponding fitted exponential decay (red) for LiTf concentrations: a) 1mM, b) 1 M[92]. The $FR = Y$ and the distance= X .	39
Figure 3-17 Debye length for solutions of LiTf/triglyme plotted as a function of $c^{1/2}$: measured by surface force measurements (black) , using measured concentration of free ions by infrared spectroscopy (red) and calculated from DH theory (blue). The straight green line is the value of the Bjerrum length for the mentioned system [92].	40
Figure 4-1 Typical impedance spectra recorded in the Li AAO: (LiTf/triglyme) Li cell and the corresponding fitted equivalent circuit.	46
Figure 4-2a) Schematic galvanostatic polarization profile b) Schematic impedance spectroscopy before and after galvanostatic polarization. The colours represent different time regimes.	48
Figure 4-3 Characterization of the AAO membranes: a,b) scanning electron micrographs(top view) of 2 sides of the membrane. c) cross-section of the pores d,e) the cross section of the AAO sides corresponding to a and b.	51
Figure 4-4 1H MAS-NMR spectra of a crushed AAO membrane (black line) was fitted with three Gaussian component (blue, purple and orange line) to estimate the total number of available surface $-OH$ groups.	52
Figure 4-5 a) Time dependent galvanostatic polarization of AAO: (1 M LiTf/triglyme) in an anion blocking Li electrolyte Li cell with current of $0.176 \mu A$, b) impedance spectra recorded before (black) and after (red) the galvanostatic polarization. Different colours correspond to different time regimes.	53
Figure 4-6 Exponential behaviour of voltage as a function of time. Extraction of the salt diffusion coefficient from the long polarization times.	54
Figure 4-7 a) Galvanostatic polarization for 0.02 and 2 M LiTf/triglyme: AAO in symmetric Li/electrolyte/Li cell b) AC measurement before and after polarization for	

2 M LiTf c) AC measurement before and after polarization for 0.02 M.....	56
Figure 4-8 Effects of lithium salt concentration variation in AAO: (LiTf/triglyme) electrolyte on: ionic conductivity (black) and lithium transference number (red) measured by galvanostatic polarization.....	57
Figure 4-9 Schematic of purely bulk conduction (left) and conduction in strong adsorption case (right).....	58
Figure 4-10 a) concentration dependent conductivity for LiTf/triglyme (black) and AAO: (LiTf/triglyme) (blue) and b) depression in σm for different salt concentration.....	59
Figure 4-11. Temperature controlled galvanostatic polarization of a Li/AAO: (1 M LiTf/triglyme)/Li cell: a) voltage-time curve for 10 and 80 °C, b) AC impedance before and after polarization at 10 °C, c) AC impedance before and after polarization at 80 °C.....	61
Figure 4-12 Temperature dependent ionic conductivity (black) and lithium transference number (red) in AAO: (LiTf/triglyme).....	62
Figure 4-13 Infrared spectra of the triflate stretching band for 1 M LiTf/triglyme at a) 20 °C, b) 80 °C. Concentration of the free ions (green), ion pairs (pink) and dimers (yellow) has been determined from the Gaussian-Lorentzian fit (dashed red line) of the total measured spectra (continuous blue line).....	63
Figure 4-14 Viscosity changes upon increasing temperature in the range of 20 to 80 °C.....	64
Figure 4-15 Temperature dependent diffusion coefficient determined at long galvanostatic polarization times.....	64
Figure 4-16. Lithium stripping-plating at 0.3 mA cm ⁻² in a symmetrical Li/electrolyte/Li cell for: a) AAO: (1 M LiTf/triglyme) b) Whatman: (1 M LiTf/triglyme).....	65
Figure 4-17 SEM images of mossy lithium formed during the stripping-plating experiment in Li AAO: (1 M LiTf/triglyme) Li cell: (a and b) mossy lithium on the surface of porous AAO (c and d) mossy lithium on the surface of lithium electrode.....	66
Figure 4-18 Lithium stripping-plating at 0.3 mA cm ⁻² in a symmetrical Li/electrolyte/Li cell for AAO: (0.02 M LiTf/triglyme).....	67
Figure 5-1 Molecular structure of LiTDI.....	69
Figure 5-2 Molecular structure of chlorotrimethylsilane.....	70
Figure 5-3 The photoemission process involved in the XPS surface analysis. The dots represent electrons and the bars represent energy levels within the atom [109]......	71
Figure 5-4 Detailed XPS spectra of pristine lithium: O 1s, C 1s and Li 1s. a-c) on the surface, d-f) after 5 minutes of Ar ⁺ sputtering, g-i) after 60 minutes of Ar ⁺ sputtering...	73
Figure 5-5 FIB-SEM images of lithium: a and b) cross section morphology of the lithium metal depicting the native passivation film. b) SEM image of the lithium showing the precipitated impurities on the grain boundaries. d) structural sketch of	

native passivating layer on lithium.	74
Figure 5-6 Detailed XPS spectra for lithium immersed in 1M LiTf/triglyme: F 1s, O 1s, C 1s and s 2p. a-d) on the surface, e-h) after 1 minute of sputtering, i-l) after 60 minutes of sputtering.	75
Figure 5-7 Detailed XPS spectra of Li 1s signal for the lithium electrode immersed in 1 M LiTf/triglyme electrolyte: a) on the surface b) after 1 minute of Ar ⁺ sputtering c) after 16 minutes of sputtering d) after 60 minutes of Ar ⁺ sputtering.	76
Figure 5-8 The increase in resistance of SEI upon time under OCV condition. Red line is the corresponding fit by assuming that a single process occurs. The dashed lined are obtained by extrapolation assuming two independent process.	78
Figure 5-9 Detailed XPS spectra for immersed sample (black) and 1Cy polarized (red): F 1s, O 1s, C 1s and S 2p. a-d) on the surface, e-h) after 16 minutes of Ar ⁺ sputtering, i-l) after 60 minutes of Ar ⁺ sputtering.	79
Figure 5-10 Detailed XPS spectra of Li 1s signal for immersed sample (black) and 1Cy polarized (red): a) on the surface b) after 16 minutes of sputtering c) after 60 minutes of sputtering.	80
Figure 5-11 Temperature dependent impedance spectroscopy of Li AAO: (1M LiTf / triglyme) Li a) in the temperature range of 20C° to 80C°. b) reversibility of R_{SEI} amid changing the temperature.	81
Figure 5-12 Detailed XPS spectra for sample at 20 °C (black) and sample at 60 °C: a-d) F 1s, O 1s, C 1s and s 2p.	81
Figure 5-13 Salt concentration dependence of R_{SEI} a) in Li AAO: (0.02-1 M LiTf)/triglyme Li at RT. b) the R_{SEI} vs. salt concentrations plot.	82
Figure 5-14 Detailed XPS spectra for one-time galvanostatically polarized for AAO: (1 M (black) and 0.02 M (red) LiTf/triglyme) : a-d) on the surface, e-h) after 60 minutes of Ar ⁺ sputtering.	83
Figure 5-15 XPS spectra of Li 1s signal for one-time galvanostatically polarized AAO: 1 M (black) and 0.02 M (red) LiTf/triglyme).	83
Figure 5-16 Impedance spectroscopy of Li AAO: (1 M LiTf / triglyme) Li cell: a) changes upon galvanostatic polarization. b) changes upon time aging at OCV conditions.	84
Figure 5-17 Detailed XPS detail spectra of) F 1s, O 1s, C 1s and s 2p for 1Cy (black) and 5Cy(red): a-d) on the surface, e-h) after 16 minutes of Ar ⁺ sputtering, i-l) after 60 minutes of Ar ⁺ sputtering.	85
Figure 5-18 a) Li 1s signal after 60 minutes of Ar ⁺ sputtering 1Cy (black) Vs 5Cy (red); b and c) SEM-FIB images of the 1Cy; c and d) SEM-FIB images of 5Cy.	86
Figure 5-19 EIS of Li AAO: 1M LiTf / triglyme Li at RT for chlorotrimethylsilane - passivated electrode before polarization (black), chlorotrimethylsilane-passivated electrode after polarization (red)and non-passivated electrode before polarization(green).	87

- Figure 5-20 Detailed XPS spectra for chlorotrimethylsilane-passivated electrode after 1Cy polarization. In addition to the F 1s , O 1s, C 1s and S 2p signal Cl 2p and Si 2p are observed. 88
- Figure 5-21 The Li 1s XPS spectra after 16 minutes of Ar⁺ sputtering for non-passivated (black) and passivated (red) lithium electrode after one-time galvanostatic polarization. The contribution of pure Li can be seen for the passivated sample, indicating that the SEI thickness is smaller. 89
- Figure 5-22 The EIS of Li| AAO: (1M LiTDI/triglyme | before (black) and after (red) galvanostatic polarization. The R_{SEI} value seems to be analogous to LiTf sample (green). 90
- Figure 5-23 Detailed XPS detail spectra for lithium electrode in contact with LiTDI after 1Cy polarization in addition to the F 1s , O 1s, C 1s signal, the N 1s is observed. Notable amount Li₃N could be observed while almost no Li₂CO₃ and smaller amount of organic phases are detected. 90
- Figure 5-24 The SEI thickness investigation with LiTDI electrolytes: a) Li 1s signal after 60 minutes of Ar⁺ ion sputtering in the LiTDI sample (red) and LiTf sample (black). No pure lithium contribution is seen for LiTDI sample; b and c) FIB-SEM cross section image of SEI formed on lithium metal in contact with LiTDI seems to be very thick. 91

References

- [1] M. Armand and J. M. Tarascon, "Building better batteries," *Nature*, vol. 451, pp. 652-657, 2008.
- [2] J. W. Choi and D. Aurbach, "Promise and reality of post-lithium-ion batteries with high energy densities," *Nature Reviews Materials*, vol. 1, p. 16013, 2016.
- [3] J. B. Goodenough and K. S. Park, "The Li-ion rechargeable battery: A perspective," *Journal of the American Chemical Society*, vol. 135, pp. 1167-1176, 2013.
- [4] J. M. Tarascon and M. Armand, "Issues and challenges facing rechargeable lithium batteries," *Nature*, vol. 414, pp. 359-367, 2001.
- [5] X.-B. Cheng, R. Zhang, C.-Z. Zhao, and Q. Zhang, "Toward Safe Lithium Metal Anode in Rechargeable Batteries: A Review," *Chemical Reviews*, vol. 117, pp. 10403-10473, 2017.
- [6] D. Lin, Y. Liu, and Y. Cui, "Reviving the lithium metal anode for high-energy batteries," *Nature Nanotechnology*, vol. 12, p. 194, 2017.
- [7] B. Liu, J.-G. Zhang, and W. Xu, "Advancing Lithium Metal Batteries," *Joule*, vol. 2, pp. 833-845, 2018.
- [8] H. Kim, G. Jeong, Y.-U. Kim, J.-H. Kim, C.-M. Park, and H.-J. Sohn, "Metallic anodes for next generation secondary batteries," *Chemical Society Reviews*, vol. 42, pp. 9011-9034, 2013.
- [9] L. F. Nazar, M. Cuisinier, and Q. Pang, "Lithium-sulfur batteries," *MRS Bulletin*, vol. 39, pp. 436-442, 2014.
- [10] M. Doyle, T. F. Fuller, and J. Newman, "The importance of the lithium ion transference number in lithium/polymer cells," *Electrochimica Acta*, vol. 39, pp. 2073-2081, 1994.
- [11] C. Pfaffhuber, M. Göbel, J. Popovic, and J. Maier, "Soggy-sand electrolytes: status and perspectives," *Physical Chemistry Chemical Physics*, vol. 15, pp. 18318-18335, 2013.
- [12] J. Popovic, G. Hasegawa, I. Moudrakovski, and J. Maier, "Infiltrated porous oxide monoliths as high lithium transference number electrolytes," *Journal of Materials Chemistry A*, vol. 4, pp. 7135-7140, 2016.
- [13] Y. Lu, Z. Tu, and L. A. Archer, "Stable lithium electrodeposition in liquid and nanoporous solid electrolytes," *Nature Materials*, vol. 13, p. 961, 2014.
- [14] A. J. Bhattacharyya and J. Maier, "Conductivity of Non-Aqueous Salt Solutions: "Soggy Sand Electrolytes"," *Advanced Materials*, vol. 16, pp. 811-814, 2004.
- [15] M. Gauthier, T. J. Carney, A. Grimaud, L. Giordano, N. Pour, H.-H. Chang, *et al.*,

- "Electrode–Electrolyte Interface in Li-Ion Batteries: Current Understanding and New Insights," *The Journal of Physical Chemistry Letters*, vol. 6, pp. 4653-4672, 2015.
- [16] E. Peled and S. Menkin, "Review-SEI: Past, Present and Future," *Journal of the Electrochemical Society*, vol. 164, pp. A1703-A1719, 2017.
- [17] E. J. W. Verwey, "Theory of the Stability of Lyophobic Colloids," *The Journal of Physical and Colloid Chemistry*, vol. 51, pp. 631-636, 1947.
- [18] D. L. Chapman, "LI. A contribution to the theory of electrocapillarity," *The London, Edinburgh, and Dublin Philosophical Magazine and Journal of Science*, vol. 25, pp. 475-481, 1913.
- [19] M. Gouy, "Sur la constitution de la charge électrique à la surface d'un électrolyte," *Journal de Physique Théorique et Appliquée*, vol. 9, pp. 457-468, 1910.
- [20] O. Stern, "Zur theorie der elektrolytischen doppelschicht," *Z. Elektrochem. Angew. Phys. Chem.*, vol. 30, pp. 508-516, 1924.
- [21] H. Lyklema, "Volume II: Solid-Liquid Interfaces," in *Fundamentals of Interface and Colloid Science*. vol. 2, J. Lyklema, Ed., ed: Academic Press, 1995, pp. vii-ix.
- [22] P. H. Debye, E., , "The theory of electrolytes I. The lowering of the freezing point and related occurrences. ," *Phys Z*, pp. 185-206, 1923.
- [23] J. Maier, "Ionic conduction in space charge regions," *Progress in Solid State Chemistry*, vol. 23, pp. 171-263, 1995.
- [24] K. Shahi and J. B. Wagner, "Fast ion transport in silver halide solid solutions and multiphase systems," *Applied Physics Letters*, vol. 37, pp. 757-759, 1980.
- [25] J. Maier, "On the heterogeneous doping of ionic conductors," *Solid State Ionics*, vol. 18-19, pp. 1141-1145, 1986.
- [26] C. C. Liang, "Conduction Characteristics of the Lithium Iodide-Aluminum Oxide Solid Electrolytes " *J. Electrochem. Soc.*, vol. 120, p. 1298, 1973.
- [27] J. Saito. Y and Maier, "Ionic Conductivity Enhancement of the Fluoride Conductor CaF₂ by Grain Boundary Activation Using Lewis Acids," *J. Electrochem. Soc.*, vol. 142, pp. 3078–3083, 1995.
- [28] A. J. Bhattacharyya, J. Maier, R. Bock, and F. F. Lange, "New class of soft matter electrolytes obtained via heterogeneous doping: Percolation effects in “soggy sand” electrolytes," *Solid State Ionics*, vol. 177, pp. 2565-2568, 2006.
- [29] J. Maier, "Acid–Base Centers and Acid–Base Scales in Ionic Solids," *Chemistry – A European Journal*, vol. 7, pp. 4762-4770, 2001.
- [30] J. Maier, "On the Conductivity of Polycrystalline Materials," *Berichte der Bunsengesellschaft für physikalische Chemie*, vol. 90, pp. 26-33, 1986.
- [31] A. Jarosik, C. Pfaffhuber, A. Bunde, and J. Maier, "Electrochemical Investigations of Polyethylene Glycol-Based “Soggy Sand” Electrolytes – From the Local Mechanism to the Overall Conduction," *Advanced Functional Materials*, vol. 21,

- pp. 3961-3966, 2011.
- [32] C. Pfaffhuber, F. Hoffmann, M. Fröba, J. Popovic, and J. Maier, "Soggy-sand effects in liquid composite electrolytes with mesoporous materials as fillers," *Journal of Materials Chemistry A*, vol. 1, pp. 12560-12567, 2013.
- [33] C. Pfaffhuber, S. Sörgel, K. Weichert, M. Bele, T. Mundinger, M. Göbel, *et al.*, "In Situ Recording of Particle Network Formation in Liquids by Ion Conductivity Measurements," *Journal of the American Chemical Society*, vol. 133, pp. 14514-14517, 2011.
- [34] E. Peled, "The Electrochemical-Behavior of Alkali and Alkaline-Earth Metals in Non-Aqueous Battery Systems - the Solid Electrolyte Interphase Model," *Journal of the Electrochemical Society*, vol. 126, pp. 2047-2051, 1979.
- [35] H. Wu, G. Chan, J. W. Choi, I. Ryu, Y. Yao, M. T. McDowell, *et al.*, "Stable cycling of double-walled silicon nanotube battery anodes through solid-electrolyte interphase control," *Nature Nanotechnology*, vol. 7, p. 310, 2012.
- [36] S. Yamaguchi, H. Asahina, K. A. Hirasawa, T. Sato, and S. Mori, "SEI Film Formation On Graphite Anode Surfaces In Lithium Ion Battery," *Molecular Crystals and Liquid Crystals Science and Technology. Section A. Molecular Crystals and Liquid Crystals*, vol. 322, pp. 239-244, 1998.
- [37] A. Manthiram, Y. Fu, S.-H. Chung, C. Zu, and Y.-S. Su, "Rechargeable Lithium-Sulfur Batteries," *Chemical Reviews*, vol. 114, pp. 11751-11787, 2014.
- [38] E. Peled, D. Golodnitsky, and J. Penciner, "The Anode/Electrolyte Interface," in *Handbook of Battery Materials*, D. Claus and J. O. Besenhard (Ed.), 2011, pp. 479-518.
- [39] D. Aurbach, I. Weissman, A. Zaban, and O. Chusid, "Correlation between surface chemistry, morphology, cycling efficiency and interfacial properties of Li electrodes in solutions containing different Li salts," *Electrochimica Acta*, vol. 39, pp. 51-71, 1994.
- [40] X.-B. Cheng, R. Zhang, C.-Z. Zhao, F. Wei, J.-G. Zhang, and Q. Zhang, "A Review of Solid Electrolyte Interphases on Lithium Metal Anode," *Advanced Science*, vol. 3, p. 1500213, 2015.
- [41] Y. E. Ely and D. Aurbach, "Identification of surface films formed on active metals and nonactive metal electrodes at low potentials in methyl formate solutions," *Langmuir*, vol. 8, pp. 1845-1850, 1992.
- [42] Y. Matsuda, "Behavior of lithium/electrolyte interface in organic solutions," *Journal of Power Sources*, vol. 43, pp. 1-7, 1993.
- [43] T. Matsui and K. Takeyama, "Lithium deposit morphology from polymer electrolytes," *Electrochimica Acta*, vol. 40, pp. 2165-2169, 1995.
- [44] J. G. Thevenin and R. H. Muller, *J. Electrochem. Soc.* , vol. 134, p. 273.
- [45] D. Aurbach, *Nonaqueous Electrochemistry*: Boca Raton: CRC Press, 1999.
- [46] H. Schmalzried, "Solid-State Reactions," in *Treatise on Solid State Chemistry*:

- Volume 4 Reactivity of Solids*, N. B. Hannay, Ed., ed Boston, MA: Springer US, 1976, pp. 233-279.
- [47] W. Xu, J. Wang, F. Ding, X. Chen, E. Nasybulin, Y. Zhang, *et al.*, "Lithium metal anodes for rechargeable batteries," *Energy & Environmental Science*, vol. 7, pp. 513-537, 2014.
- [48] C. Brissot, M. Rosso, J. N. Chazalviel, and S. Lascaud, "Dendritic growth mechanisms in lithium/polymer cells," *Journal of Power Sources*, vol. 81-82, pp. 925-929, 1999.
- [49] M. Rosso, C. Brissot, A. Teyssot, M. Dollé, L. Sannier, J.-M. Tarascon, *et al.*, "Dendrite short-circuit and fuse effect on Li/polymer/Li cells," *Electrochimica Acta*, vol. 51, pp. 5334-5340, 2006.
- [50] M. Rosso, T. Gobron, C. Brissot, J. N. Chazalviel, and S. Lascaud, "Onset of dendritic growth in lithium/polymer cells," *Journal of Power Sources*, vol. 97-98, pp. 804-806, 2001.
- [51] G. Liu and W. Lu, "A Model of Concurrent Lithium Dendrite Growth, SEI Growth, SEI Penetration and Regrowth," *Journal of The Electrochemical Society*, vol. 164, pp. A1826-A1833, 2017.
- [52] P. Bai, J. Li, F. R. Brushett, and M. Z. Bazant, "Transition of lithium growth mechanisms in liquid electrolytes," *Energy & Environmental Science*, vol. 9, pp. 3221-3229, 2016.
- [53] J. Steiger, D. Kramer, and R. Mönig, "Mechanisms of dendritic growth investigated by in situ light microscopy during electrodeposition and dissolution of lithium," *Journal of Power Sources*, vol. 261, pp. 112-119, 2014.
- [54] J. Steiger, D. Kramer, and R. Mönig, "Microscopic observations of the formation, growth and shrinkage of lithium moss during electrodeposition and dissolution," *Electrochimica Acta*, vol. 136, pp. 529-536, 2014.
- [55] B. Wu, J. Lochala, T. Taverne, and J. Xiao, "The interplay between solid electrolyte interface (SEI) and dendritic lithium growth," *Nano Energy*, vol. 40, pp. 34-41, 2017.
- [56] J.-H. Cheng, A. A. Assegie, C.-J. Huang, M.-H. Lin, A. M. Tripathi, C.-C. Wang, *et al.*, "Visualization of Lithium Plating and Stripping via in Operando Transmission X-ray Microscopy," *The Journal of Physical Chemistry C*, vol. 121, pp. 7761-7766, 2017.
- [57] X. Wang, W. Zeng, L. Hong, W. Xu, H. Yang, F. Wang, *et al.*, "Stress-driven lithium dendrite growth mechanism and dendrite mitigation by electroplating on soft substrates," *Nature Energy*, vol. 3, pp. 227-235, 2018.
- [58] A. Jana, D. R. Ely, and R. E. García, "Dendrite-separator interactions in lithium-based batteries," *Journal of Power Sources*, vol. 275, pp. 912-921, 2015.
- [59] J.-G. Zhang, W. Xu, and W. A. Henderson, "Characterization and Modeling of Lithium Dendrite Growth," in *Lithium Metal Anodes and Rechargeable Lithium Metal Batteries*, J.-G. Zhang, W. Xu, and W. A. Henderson, Eds., ed Cham: Springer

- International Publishing, 2017, pp. 5-43.
- [60] D. Aurbach, Y. Talyosef, B. Markovsky, E. Markevich, E. Zinigrad, L. Asraf, *et al.*, "Design of electrolyte solutions for Li and Li-ion batteries: A review," *Electrochimica Acta*, vol. 50, pp. 247-254, 2004.
- [61] Y. Gofer, M. Ben-Zion, and D. Aurbach, "Solutions of LiAsF₆ in 1,3-dioxolane for secondary lithium batteries," *Journal of Power Sources*, vol. 39, pp. 163-178, 1992.
- [62] K. Xu, "Nonaqueous Liquid Electrolytes for Lithium-Based Rechargeable Batteries," *Chemical Reviews*, vol. 104, pp. 4303-4418, 2004.
- [63] R. Younesi, G. M. Veith, P. Johansson, K. Edström, and T. Vegge, "Lithium salts for advanced lithium batteries: Li-metal, Li-O₂, and Li-S," *Energy & Environmental Science*, vol. 8, pp. 1905-1922, 2015.
- [64] J. Heine, P. Hilbig, X. Qi, P. Niehoff, M. Winter, and P. Bieker, "Fluoroethylene Carbonate as Electrolyte Additive in Tetraethylene Glycol Dimethyl Ether Based Electrolytes for Application in Lithium Ion and Lithium Metal Batteries," *Journal of the Electrochemical Society*, vol. 162, pp. A1094-A1101, 2015.
- [65] D. Aurbach, E. Pollak, R. Elazari, G. Salitra, C. S. Kelley, and J. Affinito, "On the surface chemical aspects of very high energy density, rechargeable Li-sulfur batteries," *Journal of the Electrochemical Society*, vol. 156, pp. A694-A702, 2009.
- [66] N.-W. Li, Y.-X. Yin, J.-Y. Li, C.-H. Zhang, and Y.-G. Guo, "Passivation of Lithium Metal Anode via Hybrid Ionic Liquid Electrolyte toward Stable Li Plating/Stripping," *Advanced Science*, vol. 4, p. 1600400, 2016.
- [67] F. Marchioni, K. Star, E. Menke, T. Buffeteau, L. Servant, B. Dunn, *et al.*, "Protection of Lithium Metal Surfaces Using Chlorosilanes," *Langmuir*, vol. 23, pp. 11597-11602, 2007.
- [68] A. Basile, A. I. Bhatt, and A. P. O'Mullane, "Stabilizing lithium metal using ionic liquids for long-lived batteries," *Nature Communications*, vol. 7, p. ncomms11794, 2016.
- [69] Y. Cao, X. Meng, and J. W. Elam, "Atomic Layer Deposition of Li_xAl_yS Solid-State Electrolytes for Stabilizing Lithium-Metal Anodes," *ChemElectroChem*, vol. 3, pp. 858-863, 2016.
- [70] A. C. Kozen, C.-F. Lin, A. J. Pearse, M. A. Schroeder, X. Han, L. Hu, *et al.*, "Next-Generation Lithium Metal Anode Engineering via Atomic Layer Deposition," *ACS Nano*, vol. 9, pp. 5884-5892, 2015.
- [71] M. Wu, Z. Wen, Y. Liu, X. Wang, and L. Huang, "Electrochemical behaviors of a Li₃N modified Li metal electrode in secondary lithium batteries," *Journal of Power Sources*, vol. 196, pp. 8091-8097, 2011.
- [72] Y. J. Zhang, W. Wang, H. Tang, W. Q. Bai, X. Ge, X. L. Wang, *et al.*, "An ex-situ nitridation route to synthesize Li₃N-modified Li anodes for lithium secondary batteries," *Journal of Power Sources*, vol. 277, pp. 304-311, 2015.
- [73] J. Zhao, L. Liao, F. Shi, T. Lei, G. Chen, A. Pei, *et al.*, "Surface Fluorination of Reactive Battery Anode Materials for Enhanced Stability," *Journal of the American*

- Chemical Society*, vol. 139, pp. 11550-11558, 2017.
- [74] Z. H. Tang, S., "Glymes as Versatile Solvents for Chemical Reactions and Processes: from the Laboratory to Industry," *RSC Adv.*, vol. 4, pp. 11251–11287, 2014.
- [75] P. Johansson, S. P. Gejji, J. Tegenfeldt, and J. Lindgren, "Local Coordination and Conformation in Polyether Electrolytes - Geometries of M-Triglyme Complexes (M=Li, Na, K, Mg and Ca) from Ab-Initio Molecular-Orbital Calculations," *Solid State Ionics*, vol. 86-88, pp. 297-302, 1996.
- [76] T. Matsui and K. Takeyama, "Li⁺ adsorption on a metal electrode from glymes," *Electrochimica Acta*, vol. 43, pp. 1355-1360, 1998.
- [77] J. Popovic, C. Pfaffenhuber, J. P. Melchior, and J. Maier, "Determination of individual contributions to the ionic conduction in liquid electrolytes: Case study of LiTf/PEGDME-150," *Electrochemistry Communications*, vol. 60, pp. 195-198, 2015.
- [78] M. Petrowsky, R. Frech, S. N. Suarez, J. R. P. Jayakody, and S. Greenbaum, "Investigation of Fundamental Transport Properties and Thermodynamics in Diglyme–Salt Solutions," *The Journal of Physical Chemistry B*, vol. 110, pp. 23012-23021, 2006.
- [79] M. V. Maslova, L. G. Gerasimova, V. N. Makarov, V. Naidenov, and W. Forsling, "A Study of Structure and Surface Properties of Cleaved Mica Particles," *Russian Journal of Applied Chemistry*, vol. 76, pp. 867-870, 2003.
- [80] K. T. Christenson, N. H., "The Nature of the Air-Cleaved Mica Surface," *Surf. Sci. Rep.*, vol. 71, p. 367–390, 2016.
- [81] J. Israelachvili, "Direct measurements of forces between surfaces in liquids at the molecular level," *Proceedings of the National Academy of Sciences*, vol. 84, p. 4722, 1987.
- [82] J. Israelachvili, Y. Min, M. Akbulut, A. Alig, G. Carver, W. Greene, *et al.*, "Recent advances in the surface forces apparatus (SFA) technique," *Reports on Progress in Physics*, vol. 73, p. 036601, 2010.
- [83] M. A. Gebbie, H. A. Dobbs, M. Valtiner, and J. N. Israelachvili, "Long-range electrostatic screening in ionic liquids," *Proceedings of the National Academy of Sciences*, vol. 112, p. 7432, 2015.
- [84] T. Utzig, "A contribution to understanding interfacial adhesion based on molecular level knowledge," PhD, 2017.
- [85] J. N. Israelachvili, "Chapter 12 - Force-Measuring Techniques," in *Intermolecular and Surface Forces (Third Edition)*, J. N. Israelachvili, Ed., ed San Diego: Academic Press, 2011, pp. 223-252.
- [86] B. Derjaguin, "Untersuchungen über die Reibung und Adhäsion, IV," *Kolloid-Zeitschrift*, vol. 69, pp. 155-164, 1934.
- [87] R. J. Hunter, "Chapter 2 - Charge and Potential Distribution at Interfaces," in *Zeta Potential in Colloid Science*, R. J. Hunter, Ed., ed: Academic Press, 1981, pp. 11-

- 58.
- [88] F. Booth, "The electroviscous effect for suspensions of solid spherical particles," *Proceedings of the Royal Society of London. Series A. Mathematical and Physical Sciences*, vol. 203, p. 533, 1950.
- [89] R. W. O'Brien, "Electro-acoustic effects in a dilute suspension of spherical particles," *Journal of Fluid Mechanics*, vol. 190, pp. 71-86, 2006.
- [90] C. Pfaffenhuber, "Short and long range transport effects in salt containing solid-liquid composites," PhD, Stuttgart, 2014.
- [91] I. N. Levine, *Physical chemistry*. New York: McGraw-Hill, 1988.
- [92] M. Nojabae, H.-W. Cheng, M. Valtiner, J. Popovic, and J. Maier, "Interfacial Layering and Screening Behavior of Glyme-Based Lithium Electrolytes," *The Journal of Physical Chemistry Letters*, vol. 9, pp. 577-582, 2018.
- [93] H. J. Taunton, C. Toprakcioglu, L. J. Fetters, and J. Klein, "Forces between surfaces bearing terminally anchored polymer chains in good solvents," *Nature*, vol. 332, p. 712, 1988.
- [94] P.-G. de Gennes, *Scaling concepts in polymer physics*. Cornell: University Press: Ithaca, NY, 1979.
- [95] V. A. Parsegian and D. Gingell, "On the Electrostatic Interaction across a Salt Solution between Two Bodies Bearing Unequal Charges," *Biophysical Journal*, vol. 12, pp. 1192-1204, 1972.
- [96] A. A. Lee, C. S. Perez-Martinez, A. M. Smith, and S. Perkin, "Underscreening in concentrated electrolytes," *Faraday Discussions*, vol. 199, pp. 239-259, 2017.
- [97] R. Kjellander, "Decay behavior of screened electrostatic surface forces in ionic liquids: the vital role of non-local electrostatics," *Physical Chemistry Chemical Physics*, vol. 18, pp. 18985-19000, 2016.
- [98] R. Kjellander and D. J. Mitchell, "Dressed-ion theory for electrolyte solutions: A Debye-Hückel-like reformulation of the exact theory for the primitive model," *The Journal of Chemical Physics*, vol. 101, pp. 603-626, 1994.
- [99] F. Keller, Hunter, M. S. & Robinson, D. L. , " Structural features of oxide coatings on aluminium.," *J. Electrochem. Soc.*, vol. 100, pp. 411-419 1953.
- [100] W. Lee, R. Ji, U. Gösele, and K. Nielsch, "Fast fabrication of long-range ordered porous alumina membranes by hard anodization," *Nature Materials*, vol. 5, p. 741, 2006.
- [101] J. Maier, *Physical Chemistry of Ionic Materials: Ions and Electrons in Solids*: John Wiley & Sons, 2004.
- [102] Z. Tu, M. J. Zachman, S. Choudhury, S. Wei, L. Ma, Y. Yang, *et al.*, "Nanoporous Hybrid Electrolytes for High-Energy Batteries Based on Reactive Metal Anodes," *Advanced Energy Materials*, vol. 7, 2017.
- [103] R. Dupree, I. Farnan, A. J. Forty, S. El-Mashri, and L. Bottyan, "A MAS NMR STUDY OF THE STRUCTURE OF AMORPHOUS ALUMINA FILMS," *J. Phys.*

- Colloques*, vol. 46, pp. C8-113-C8-117, 1985.
- [104] J. Maier, "Mass Transport in the Presence of Internal Defect Reactions—Concept of Conservative Ensembles: I, Chemical Diffusion in Pure Compounds," *Journal of the American Ceramic Society*, vol. 76, pp. 1212-1217, 1993.
- [105] M. Bukowska, J. Prejzner, and P. Szczeciński, "Synthesis of 4,5-dicyanoimidazoles," *Polish Journal of Chemistry*, vol. 78, pp. 417-422, 2004.
- [106] L. Niedzicki, G. Z. Żukowska, M. Bukowska, P. Szczeciński, S. Grugeon, S. Laruelle, *et al.*, "New type of imidazole based salts designed specifically for lithium ion batteries," *Electrochimica Acta*, vol. 55, pp. 1450-1454, 2010.
- [107] C. L. Berhaut, P. Porion, L. Timperman, G. Schmidt, D. Lemordant, and M. Anouti, "LiTDI as electrolyte salt for Li-ion batteries: transport properties in EC/DMC," *Electrochimica Acta*, vol. 180, pp. 778-787, 2015.
- [108] L. Niedzicki, E. Karpierz, A. Bitner, M. Kasprzyk, G. Z. Zukowska, M. Marcinek, *et al.*, "Optimization of the lithium-ion cell electrolyte composition through the use of the LiTDI salt," *Electrochimica Acta*, vol. 117, pp. 224-229, 2014.
- [109] R. S. Thompson, D. J. Schroeder, C. M. López, S. Neuhold, and J. T. Vaughey, "Stabilization of lithium metal anodes using silane-based coatings," *Electrochemistry Communications*, vol. 13, pp. 1369-1372, 2011.
- [110] E. Paterson and R. Swaffield, "X-ray photoelectron spectroscopy," in *Clay Mineralogy: Spectroscopic and Chemical Determinative Methods*, M. J. Wilson, Ed., ed Dordrecht: Springer Netherlands, 1994, pp. 226-259.
- [111] C. Fiedler, B. Luerssen, M. Rohnke, J. Sann, and J. Janek, "XPS and SIMS Analysis of Solid Electrolyte Interphases on Lithium Formed by Ether-Based Electrolytes," *Journal of The Electrochemical Society*, vol. 164, pp. A3742-A3749, 2017.
- [112] Q. Pang, X. Liang, A. Shyamsunder, and L. F. Nazar, "An in Vivo Formed Solid Electrolyte Surface Layer Enables Stable Plating of Li Metal," *Joule*, vol. 1, pp. 871-886, 2017.
- [113] C. S. Rustomji, Y. Yang, T. K. Kim, J. Mac, Y. J. Kim, E. Caldwell, *et al.*, "Liquefied gas electrolytes for electrochemical energy storage devices," *Science*, vol. 356, pp. 4263, 2017.
- [114] A. Schechter, D. Aurbach, and H. Cohen, "X-ray Photoelectron Spectroscopy Study of Surface Films Formed on Li Electrodes Freshly Prepared in Alkyl Carbonate Solutions," *Langmuir*, vol. 15, pp. 3334-3342, 1999.
- [115] N. Schulz, R. Hausbrand, C. Wittich, L. Dimesso, and W. Jaegermann, "XPS-Surface Analysis of SEI Layers on Li-Ion Cathodes: Part II. SEI-Composition and Formation inside Composite Electrodes," *Journal of The Electrochemical Society*, vol. 165, pp. A833-A846, 2018.
- [116] K. Weichert, W. Sigle, P. A. van Aken, J. Jamnik, C. Zhu, R. Amin, *et al.*, "Phase Boundary Propagation in Large LiFePO₄ Single Crystals on Delithiation," *Journal of the American Chemical Society*, vol. 134, pp. 2988-2992, 2012.
- [117] J. Jamnik, J. Maier, and S. Pejovnik, "Interfaces in solid ionic conductors:

- Equilibrium and small signal picture," *Solid State Ionics*, vol. 75, pp. 51-58, 1995.
- [118] C. Li, L. Gu, X. Guo, D. Samuelis, K. Tang, and J. Maier, "Charge Carrier Accumulation in Lithium Fluoride Thin Films due to Li-Ion Absorption by Titania (100) Subsurface," *Nano Letters*, vol. 12, pp. 1241-1246, 2012.
- [119] J. Maier, "Defect chemistry in heterogeneous systems," *Solid State Ionics*, vol. 75, pp. 139-145, 1995.
- [120] Q. Zhang, J. Pan, P. Lu, Z. Liu, M. W. Verbrugge, B. W. Sheldon, *et al.*, "Synergetic Effects of Inorganic Components in Solid Electrolyte Interphase on High Cycle Efficiency of Lithium Ion Batteries," *Nano Letters*, vol. 16, pp. 2011-2016, 2016.
- [121] S. Shi, Y. Qi, H. Li, and L. G. Hector, "Defect Thermodynamics and Diffusion Mechanisms in Li₂CO₃ and Implications for the Solid Electrolyte Interphase in Li-Ion Batteries," *The Journal of Physical Chemistry C*, vol. 117, pp. 8579-8593, 2013.
- [122] J. Pan, Y.-T. Cheng, and Y. Qi, "General method to predict voltage-dependent ionic conduction in a solid electrolyte coating on electrodes," *Physical Review B*, vol. 91, 2015.
- [123] A. W. Jones, F. C. Kugelberg, A. Holmgren, and J. Ahlner, "Five-year update on the occurrence of alcohol and other drugs in blood samples from drivers killed in road-traffic crashes in Sweden," *Forensic Science International*, vol. 186, pp. 56-62, 2009.
- [124] J. Jones, M. Anouti, M. Caillon-Caravanier, P. Willmann, P.-Y. Sizaret, and D. Lemordant, "Solubilization of SEI lithium salts in alkylcarbonate solvents," *Fluid Phase Equilibria*, vol. 305, pp. 121-126, 2011.
- [125] U. v. Alpen, A. Rabenau, and G. H. Talat, "Ionic conductivity in Li₃N single crystals," *Applied Physics Letters*, vol. 30, pp. 621-623, 1977.
- [126] B. A. Boukamp and R. A. Huggins, "Fast ionic conductivity in lithium nitride," *Materials Research Bulletin*, vol. 13, pp. 23-32, 1978.
- [127] H. Shin, J. Park, S. Han, A. M. Sastry, and W. Lu, "Component-/structure-dependent elasticity of solid electrolyte interphase layer in Li-ion batteries: Experimental and computational studies," *Journal of Power Sources*, vol. 277, pp. 169-179, 2015.
- [128] S. L. Koch, B. J. Morgan, S. Passerini, and G. Teobaldi, "Density functional theory screening of gas-treatment strategies for stabilization of high energy-density lithium metal anodes," *Journal of Power Sources*, vol. 296, pp. 150-161, 2015.
- [129] J. Guo, Z. Wen, M. Wu, J. Jin, and Y. Liu, "Vinylene carbonate–LiNO₃: A hybrid additive in carbonic ester electrolytes for SEI modification on Li metal anode," *Electrochemistry Communications*, vol. 51, pp. 59-63, 2015.
- [130] S. S. K. Kanamura, Z. i. Takehara, "XPS Analysis of Lithium Surfaces Following Immersion in Various Solvents Containing LiBF₄," *J. Electrochem. Soc.*, vol. 143, p. 2187 1996.

Acknowledgments

Hereby, I would like to express my appreciation to many people who made this thesis possible.

First of all, I would like to thank Prof. Joachim Maier for giving me the chance to do my PhD in his research group. It was a pleasure to have the opportunity to work with him and learn from him in this period.

I am most grateful to Dr. Jelena Popovic, my daily supervisor, for her scientific advices and experimental ideas as well as her tremendous patience and availability during my PhD.

I would like to acknowledge Prof. Dr. Sabine Ludwigs and Prof. Dr. Peer Fischer for honouring me as co-examiner and exam chairman for my PhD exam, respectively.

Many thanks go to Prof. Dr. Markus Valtiner that gave me the opportunity to use the Surface force apparatus setup developed in his research group at *Max Planck Institute for Iron Research* in Düsseldorf and also Dr. Hsiu-Wei Cheng who introduced me to this setup and helped to run the experiments. I had lots of fruitful scientific discussion with both of them about our recorded data.

I thank Dr. Kathrin Müller for running all the XPS experiments patiently and teaching me how to analyse the XPS data.

I thank Dr. Rotraut Merkle and Dr. Robert Usiskin for their help in many scientific and experimental matters in the last years.

Special thanks go to Florian Kaiser for maintaining the glove box and designing cells for my project. Many thanks to the other technical support from our department, I am grateful to Udo Klock, Annette Fuchs, Uwe Traub, Dr. Helga Hoier, Armin Sorg.

I also thank Bernhard Fenk for doing the FIB experiment specifically for challenging and time-consuming lithium electrodes.

I would like to thank dear Sofia Weiglein for all her administrative helps.

Many thanks to my colleagues (Torben Saatkamp, Simon Lorger, Pinar kaya, Alessandro Senocrate, Gee young Kim, Gints Kucinskis, Andreas Münchinger, Reihaneh Zohourian, Kyungmi Lim) for many nice moments that we spent together during lunch time and gatherings. These social communications were indeed a huge support for the hard days.

Regarding the same matter, I thank once more Dr. Jelena Popovic for the very nice personal relationship that we developed. We shared lots of happy, exciting and challenging moments together in our great office (7M14).

I thank all the friends and family in Stuttgart for making me feel at home, specifically Doris and Wolfgang.

I owe my deepest gratitude to my family for being very supportive and encouraging all the time, in particular, my amazing mom (Nasrin) for her endless kindness and sacrifices.

Finally, I would like to thank my boyfriend (Daniel) for his tremendous love and support. He has been very understanding and helpful during the encountered challenging times in my PhD. We shared lots of great moments during this time in Stuttgart in addition to our great travelling experiences from far- to middle-east to the west.

Maryam Nojabae

Curriculum Vitae

Full Name: Seyedeh Maryam Nojabaee

Date of Birth: 10.07.1989

Email: M.Nojabaee@fkf.mpg.de

Education:

- **PhD in Chemistry (2015-2018)**

Max Planck Institute for Solid State Research (MPI), Stuttgart

Title: "Interfacial Effects in Solid-Liquid Glyme-based Electrolytes for Lithium Batteries"

Supervisor: Prof. Dr. Joachim Maier

- **MSc in Material Science (2012- 2014)**

University of Kiel (CAU)

Title: "FFT- Impedance Analysis of Anodes for Lithium-Ion-Batteries Containing Silicon Microwires with Different Thicknesses"

Supervisor: Prof. Dr. Rainer Adelung

- **BSc in Material Engineering-Ceramic Engineering (2008-2012)**

Iran University of Science and Technology

Title: "Solid-Solution Investigation of Ultra-High-Temperature-Ceramics using X-ray diffraction "

Supervisor: Prof. Dr. Farhad Golestanifard

- **High School and College Diploma in Mathematics and Physics (2004-2008)**

Foroughe Danesh, Tonekabon, Mazandaran, Iran